

Master's Thesis

**Exploring the Pseudogap-to-Fermi
Liquid Phase Transition
in Dynamical Cluster Approximation
using Numerical Renormalization
Group**

Chair of Theoretical Solid State Physics
Faculty of Physics
Ludwig-Maximilians-Universität München

Boheng Niu

Munich, December 12, 2024



Supervisor:
Prof. Jan von Delft

Masterarbeit

**Untersuchung des Phasenübergangs
vom Pseudospalt- zum
Fermiflüssigkeitszustand
in der Dynamischen Cluster-Näherung
mittels Numerischer
Renormierungsgruppe**

Lehrstuhl für Theoretische Festkörperphysik
Fakultät für Physik
Ludwig-Maximilians-Universität München

Boheng Niu

München, den 12. Dezember 2024



Betreuer:
Prof. Jan von Delft

Declaration of authorship

I hereby declare that this thesis is my own work, and that I have not used any sources and aids other than those stated in the thesis.

München, December 12, 2024

Boheng Niu

Abstract

The pseudogap phenomenon and its transition to the Fermi liquid state is of interest in the physics of hole-doped cuprates. The pseudogap, characterized by a suppression of electronic states near the Fermi level along antinodal directions, remains enigmatic and is closely tied to unconventional superconductivity. Understanding this transition requires capturing the interplay between local strong correlations and momentum-dependency. In this work, we investigate whether the 2-site Dynamical Cluster Approximation (DCA) framework, that dichotomizes the Brillouin zone into two coarse-grained momenta, can capture the critical behavior of the pseudogap-to-Fermi liquid transition, focusing on both single-band Hubbard and three-band Emery models.

Our approach combines DCA with the Numerical Renormalization Group (NRG), enabling high-precision analysis of low-energy properties. By tuning the chemical potential, we systematically study the doping evolution from the underdoped to overdoped regimes. The Emery model, incorporating additional p_x - and p_y -orbitals, provides a more realistic description of the CuO_2 plane and allows us to test whether a multi-orbital setup compensates for the limitations of small clusters in DCA.

Through calculations of the spectral function, self-energy, current and magnetic susceptibilities, we identify a continuous insulator-to-metal transition at a critical doping level x_c in the border momentum patch, corresponding to antinodal direction. However, the 2-site DCA framework fails to capture a genuine quantum critical point (QCP), with energy flow analysis confirming the persistent Fermi liquid characteristics across all doping levels. While the Emery model refines momentum-dependent features, the absence of a true QCP underscores the need for larger cluster studies to fully resolve the pseudogap-to-Fermi liquid phase transition.

Acknowledgments

First and foremost, I would like to thank Prof. Jan von Delft for giving me this excellent opportunity to join his group and investigate this interesting topic.

Many thanks to Mathias Pelz, who provided significant guidance and support on both conceptual and technical problems. This work could not have been completed without his patient and helpful assistance.

I would also like to thank Dr. Andreas Gleis for his insightful discussions and suggestions, as well as Dr. Jeongmin Shim and Ming Huang for their assistance in setting up the task submission code.

Equally important, this work is based on the powerful tensor network library QSpace-v4.0, developed by Dr. Andreas Weichselbaum, along with the NRG solver developed by Prof. Seung-Sup B. Lee. I would like to express my gratitude to them and greatly appreciate their brilliant contributions.

I am also grateful to my colleagues in the Chair of Theoretical Solid State Physics for their fruitful discussions and constant inspiration. The stimulating research environment and access to advanced computational resources made this project possible.

Finally, a special thanks to my family and friends for their unconditional support and understanding during the demanding times of this journey. Their belief in me kept me motivated and focused.

Contents

1	Introduction	1
2	Dynamical Mean Field Theory (DMFT)	3
2.1	Introduction to mean-field theory	3
2.2	Hubbard model in infinite dimensions	6
2.3	Green's function and self-energy	9
2.4	Effective impurity problem	10
2.5	The self-consistency procedure	15
2.6	Cluster extensions	17
3	Numerical Renormalization Group (NRG)	22
3.1	Introduction to NRG	22
3.2	The Single impurity Anderson model (SIAM)	23
3.3	Logarithmic discretization	26
3.4	Mapping onto a Wilson chain	28
3.5	Iterative diagonalization	29
3.6	Renormalization group flow	33
4	Model Study	35
4.1	Fermi liquid theory	35
4.2	Pseudogap	37
4.3	Realization of 2-site DCA	39
4.4	Three-band Hubbard model (Emery model)	40
5	Numerical Results I (Hubbard Model)	46
5.1	Spectral functions	46
5.2	Self-energy and quasiparticle weight	49
5.3	Susceptibility and phase diagram	52
5.4	Energy flow	55
6	Numerical Results II (Emery Model)	57
6.1	Spectral functions	57
6.2	Self-energy and quasiparticle weight	60
6.3	Susceptibility and phase diagram	61
6.4	Energy flow	62
7	Conclusion and Outlook	64
A	Fluctuations in the overdoped regime	I
B	Electronic structure	III

1 Introduction

Background and methods

Strongly correlated electron systems, such as high-temperature superconductors, exhibit complex phenomena that challenge conventional theories. Among these phenomena, the pseudogap observed in hole-doped cuprates has garnered significant attention due to its connection with unconventional superconductivity and its enigmatic nature [1, 2]. Understanding the pseudogap state requires advanced theoretical frameworks capable of resolving both momentum-dependent and low-energy properties.

Dynamical Mean-Field Theory (DMFT) has emerged as a powerful method for investigating strongly correlated systems [3, 4]. By mapping the lattice problem onto an effective impurity model, DMFT provides a non-perturbative approach to capture local quantum fluctuations. However, DMFT inherently lacks momentum resolution, limiting its ability to describe phenomena like the pseudogap [5], which exhibit strong momentum dependence. To address this limitation, cluster extensions such as Dynamical Cluster Approximation (DCA) have been developed [6].

Furthermore, the numerical renormalization group offers a highly accurate real-frequency method to solve impurity models [7, 8], with exceptional resolution at low energies, which enables us to study zero-temperature properties. Combining NRG with DCA allows us to investigate the momentum-selective pseudogap phenomena.

Motivation and goal

In this thesis, we utilize the DCA+NRG framework to explore the pseudogap-Fermi liquid transition in two representative models: the single-band Hubbard model and the three-band Emery model [9]. Our investigation reveals that under the 2-site DCA scheme, the single-band model fails to capture the genuine quantum criticality associated with the pseudogap state. This limitation motivates us to investigate the three-band Emery model, which incorporates additional p_x - and p_y -orbitals to describe the CuO_2 plane in cuprates. The Emery model is, as a three-band model, closer to real materials. Therefore, we ask the question if this model, treated in DCA as a 2-site cluster, is enough to capture the underlying physics of the pseudogap phase.

Structure

In Chapter 2, we introduce the theoretical foundation of DMFT, emphasizing its role in describing correlated systems and its limitations in capturing momentum-dependent properties. Chapter 3 provides an overview of the Numerical Renormalization Group, focusing on its application to impurity models within the DMFT framework. Chapter 4 describes the models studied in this thesis, including the single-band Hubbard model and the three-band Emery model, along with their respective parameterizations. In Chapters 5 and 6, we present the numerical results for the Hubbard and Emery models, respectively, discussing the spectral functions, critical doping levels, and dynamical properties such as

current and spin susceptibilities.

Conclusion

Through this work, we aim to provide insights into the pseudogap state and its evolution with doping, while highlighting the similarities between the single-band and three-band Hubbard models. Our findings reveal that the 2-site DCA scheme fails to capture the genuine quantum criticality associated with the pseudogap state, underscoring the limitations of small cluster approximations. This highlights the need for larger cluster studies to sufficiently resolve the spatial correlations and the possible quantum criticality in these strongly correlated systems.

2 Dynamical Mean Field Theory (DMFT)

2.1 Introduction to mean-field theory

The study of correlated electron systems is currently one of the most actively investigated fields in modern physics. In this chapter, we first provide a heuristic discussion of what correlation means [10] and then introduce one of the most important and successful solutions to this problem: dynamical mean-field theory.

In single-particle quantum physics, our ultimate goal is to find the average or expectation values of observables, which are represented by linear operators. Similarly, in many-body physics, we are interested in the expectation value of a product of quantities, which typically satisfies the following inequality:

$$\langle AB \rangle \neq \langle A \rangle \langle B \rangle. \quad (2.1)$$

Such property is attributed to correlations between A and B . A more concrete example is the density-density correlation function

$$\langle n(\mathbf{r})n(\mathbf{r}') \rangle \neq \langle n(\mathbf{r}) \rangle \langle n(\mathbf{r}') \rangle = n^2. \quad (2.2)$$

The function does not factorize due to what is known as correlation. In the case of a non-interacting classical system, the formula above is supposed to be an equality, meaning the particle density at position \mathbf{r} is independent of the particle density at position \mathbf{r}' , i.e., the system is uncorrelated. However, in quantum systems, the inequality always holds, even for the non-interacting case, due to quantum statistics. Fermions with the same spin direction do not occupy the same position, whereas bosons tend to cluster together. Thus, the spatial dependence is inherently present in quantum systems, leading to non-vanishing correlations. Correlation, therefore, is defined as the property whereby expectation values cannot be factorized using methods such as Hartree-Fock theory.

A natural question arises: in which types of systems are correlations strong enough to be significant? Assuming the band electrons have a certain dispersion $\varepsilon_{\mathbf{k}}$, their velocity can be evaluated as $v_{\mathbf{k}} = \frac{1}{\hbar} |\nabla_{\mathbf{k}} \varepsilon_{\mathbf{k}}|$. On the one hand, the typical value of velocity is given by $v_{\mathbf{k}} \propto a/\tau$, where a is the lattice constant and τ is the time an electron spends within an atom. On the other hand, $|\nabla_{\mathbf{k}}| \propto 1/k \propto a$, and $|\varepsilon_{\mathbf{k}}|$ is proportional to the bandwidth W . Combining these equations and approximations, we arrive at:

$$\tau \propto \frac{\hbar}{W}. \quad (2.3)$$

The above relation implies that a narrower band leads to a longer time that an electron resides on an atom, thereby feeling the presence of another electron with a different spin direction. The spatial confinement enhances the effect due to the Coulomb interaction between electrons. Consequently, materials with narrower bands and partially filled shells (typically d and f shells) are referred to as strongly correlated systems.

Due to the non-factorization in Eq. (2.1), finding an exact solution to many-body models, such as the Hubbard model, is challenging. Dynamical mean-field theory (DMFT) is an appealing candidate for an approximate solution. To better understand the underlying principles, we will first revisit a much simpler model, the classical Ising model, using mean-field theory, and then turn to the discussion of the Hubbard model solved by its dynamical version.

The classical Ising model describes a system of spins, where each spin σ_i can take values $+1$ or -1 , representing up- or down- orientations. The spins are arranged on a lattice, and each spin interacts with its nearest neighbors. The Hamiltonian is:

$$H = -J \sum_{\langle i,j \rangle} S_i S_j - h \sum_i S_i, \quad (2.4)$$

where J is the interaction strength between neighboring spins, which is taken to be positive for ferromagnetism in our case, S_i and S_j are the spins at lattice sites i and j , and h is an external magnetic field. This model remains difficult to solve, despite being classical, due to the correlated (interaction) term $S_i S_j$, which results in $\langle S_i S_j \rangle \neq \langle S_i \rangle \langle S_j \rangle$.

The most important approximation applied in mean-field theory is to treat the interaction as an overall mean-field. We assume each spin only feels an average effect from its neighbors, rather than considering each interaction individually. This leads to the following steps.

- (a) Approximate the local field. Each spin S_i experience an effective mean-field h_{eff} , which is proportional to the average spin $\langle S_j \rangle = \langle S \rangle$ with a factor $-Jz$, i.e the product of interaction strength and number of nearest neighbors. Thus the interaction term of the Hamiltonian becomes:

$$H_i = -h_{\text{eff}} S_i = -(Jz \langle S \rangle + h) S_i. \quad (2.5)$$

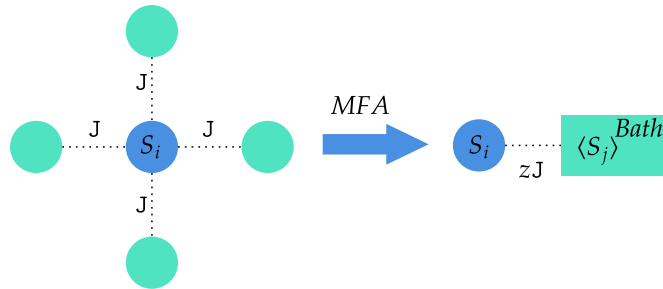


Figure 1: A schematic illustrating the mean-field approximation (MFA) applied in Ising model. The neighboring sites are treated as an averaged bath, hence the $S_i S_j$ interaction term is decoupled into an effective single-particle term described by H_{eff} .

This corresponds to the factorization

$$\begin{aligned} \langle [S_i - \langle S \rangle][S_j - \langle S \rangle] \rangle &= \langle S_i S_j - \langle S \rangle S_i - \langle S \rangle S_j + \langle S \rangle^2 \rangle \\ &= \langle S_i S_j \rangle - \langle S \rangle (S_i + S_j) + \langle S \rangle^2 \\ &\equiv 0 \end{aligned} \quad (2.6)$$

which gives $\langle S_i S_j \rangle = \langle S \rangle (S_i + S_j)$ (constant $\langle S \rangle^2$ has been dropped). Consequently, there are no more cross terms $S_i S_j$ in Eq. (2.5), as we decoupled the interaction term by h_{eff} , which is an approximation and the specific value must be determined self-consistently. By now, the original Hamiltonian is cast in the form

$$H = \sum_i H_i, \quad (2.7)$$

and can be solved exactly.

- (b) Find the self-consistency condition. As the Hamiltonian is decoupled in the form of Eq. (2.7), we transformed a complex lattice to a summation of a series single sites. As a consequence, one only needs to focus on one of the sites, e.g. $\langle S_i \rangle = \langle S \rangle$. In statistical mechanics, the probability that spin S_i takes a particular value is given by the Boltzmann distribution

$$P(S_i) = \frac{e^{-\beta H_i}}{Z} = \frac{e^{\beta h_{\text{eff}} S_i}}{Z}. \quad (2.8)$$

Since S_i can only take values ± 1 , the partition function can be easily evaluated

$$Z = \sum_{S_i=\pm 1} P(S_i) = e^{\beta h_{\text{eff}}} + e^{-\beta h_{\text{eff}}} = 2 \cosh(\beta h_{\text{eff}}). \quad (2.9)$$

With the partition function at hand, one can express the expectation value of spin

$$\langle S_i \rangle = \sum_{S_i=\pm 1} S_i P(S_i) = \frac{1}{Z} (e^{\beta h_{\text{eff}}} - e^{-\beta h_{\text{eff}}}) = \frac{\sinh(\beta h_{\text{eff}})}{\cosh(\beta h_{\text{eff}})} = \tanh(\beta h_{\text{eff}}). \quad (2.10)$$

From now on we denote the average spin $\langle S_i \rangle = \langle S \rangle$ as magnetization m , and regard it as the so-called Weiss mean-field. The above equation becomes

$$m = \tanh(\beta h_{\text{eff}}). \quad (2.11)$$

Finally, substituting the expression for the effective field $h_{\text{eff}} = (Jz\langle S \rangle + h)$, we arrive at the self-consistent equation for the mean-field m , which can be solved iteratively

$$m = \tanh(\beta(Jzm + h)). \quad (2.12)$$

- (c) Solve the self-consistent equation. It is worth pointing out the reason why Eq. (2.12) is referred to as a self-consistent equation. This originates from the mean-field nature of the method. The right-hand side of the equation is based on an important assumption: each spin only feels an averaged mean-field represented by $Jz\langle S \rangle$. Only with this assumption one can evaluate the expectation value of the local spin via Eq. (2.10). On the left-hand side, m stands for the real magnetization, by equating m and $\langle S_i \rangle$, we are essentially applying the mean-field approximation: expectation value of local spin evaluated via a mean-field (input), is required to be equal to

the real magnetization (output). We hope to solve m via an expression including m itself, therefore it is called self-consistent.

Iterative method is a commonly used approach to solve the above equation:

- (i) Start with an initial guess for m , e.g $m = m_0$.
- (ii) Plug the guess solution into the RHS of Eq. (2.12) and obtain the value m_1 .
- (iii) Plug m_1 into Eq. (2.12) again for the next iteration and so on.
- (iv) Continue this process until the value of m converges, i.e. until $|m_{n+1} - m_n|$ is sufficiently small.

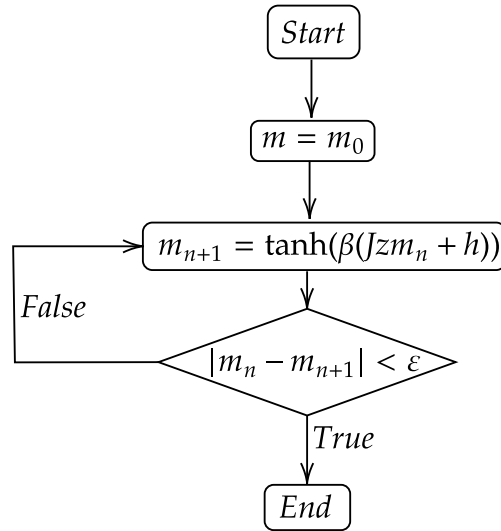


Figure 2: A flowchart of the iterative solution of the Ising self-consistent equation.

where J is the interaction strength between neighboring spins, which is taken to be positive for ferromagnetism in our case, S_i and S_j are the spins at lattice sites i and j , and h is an external magnetic field. This model remains difficult to solve, despite being classical, due to the correlated (interaction) term $S_i S_j$, which results in $\langle S_i S_j \rangle \neq \langle S_i \rangle \langle S_j \rangle$.

The key approximation used in mean-field theory is to treat the interaction as an overall mean-field. We assume that each spin only feels the average effect from its neighbors, rather than considering each individual interaction. This approximation leads to the following steps.

2.2 Hubbard model in infinite dimensions

In the following sections, the dynamical version of mean-field theory will be elaborated by solving the typical and fundamental many-body model, i.e., the Hubbard model. We will first discuss the scaling behavior, followed by the self-consistent equation.

We consider the simplest model describing electron interactions in a solid, namely, the single-band, spin- $\frac{1}{2}$ Hubbard model. The Hamiltonian is defined on a cubic lattice in d dimensions, and we assume natural units with $\hbar = k_B = 1$.

$$\begin{aligned} H &= H_{\text{kin}} + H_{\text{int}} - \mu N \\ &= - \sum_{\langle i,j \rangle, \sigma} t_{ij} c_{i\sigma}^\dagger c_{j\sigma} + U \sum_i n_{i\uparrow} n_{i\downarrow} - \mu \sum_{i\sigma} n_{i\sigma}, \end{aligned} \quad (2.13)$$

where $\langle i, j \rangle$ denotes a sum over nearest neighbors, $c_{i\sigma}^{(\dagger)}$ the annihilation (creation) operators of a conduction electron occupying site i and carrying spin σ , and $n_{i\sigma}$ the number operator. As for the parameters of the model, U is the Coulomb interaction strength. In the Hubbard model, the basic assumption is that the Coulomb interaction is strong enough (at least comparable to the kinetic energy, or hopping amplitude t_{ij}) to be screened by the lattice, making it a purely local term in the Hamiltonian. μ is the chemical potential, and t_{ij} are the hopping amplitudes. In this chapter, we consider an isotropic hopping, i.e., $t_{ij} = t$. Since the kinetic term is a quadratic form of creation/annihilation operators and is defined on a periodic lattice, H_{kin} can be diagonalized by Fourier transformation.

$$c_{i\sigma}^{(\dagger)} = \frac{1}{\sqrt{N}} \sum_{\mathbf{k}} e^{(\pm)i\mathbf{k}\mathbf{R}_i} c_{i\sigma}^{(\dagger)}, \quad (2.14)$$

which gives the kinetic term in momentum representation

$$H_{\text{kin}} = \sum_{\mathbf{k}\sigma} \varepsilon_{\mathbf{k}} n_{\mathbf{k}\sigma}, \quad (2.15)$$

where $\varepsilon_{\mathbf{k}}$ is the tight-binding dispersion relation, for a cubic lattice in d dimension, it reads

$$\varepsilon_{\mathbf{k}} = -2t \sum_{\alpha=1}^d \cos k_\alpha. \quad (2.16)$$

The number of nearest neighbors is defined as the coordination number $z = 2d$ (for a hypercubic lattice). It is clear that the kinetic energy depends on d , and consequently on z . Thus, when we take the infinite z limit, as we did for the Ising model, the kinetic energy $\varepsilon_{\mathbf{k}}$ diverges as well. The Hubbard model considers the competition between mobility (t) and localization (U) of electrons. To maintain this competition and avoid divergence, a rescaling of t is necessary. On the other hand, the chemical potential and Coulomb interaction terms are independent of dimension, so no rescaling is needed for μ and U .

To find an appropriate scaling, we require the width of the non-interacting density of states to be independent of dimension d .

$$\rho_0(\varepsilon) = \frac{1}{N} \sum_{\mathbf{k}} \delta(\varepsilon - \varepsilon_{\mathbf{k}}) = \int_{-\pi}^{\pi} \frac{d^d \mathbf{k}}{(2\pi)^d} \delta(\varepsilon - \varepsilon_{\mathbf{k}}). \quad (2.17)$$

The width is defined as the variance of the distribution

$$\sigma^2 = \int_{-\infty}^{\infty} d\varepsilon \rho_0(\varepsilon) \varepsilon^2 = 2t^2 d. \quad (2.18)$$

Let the width be a constant and relabel it

$$2t^2d = \text{const} \equiv (t^*)^2. \quad (2.19)$$

One obtains the scaling for t

$$t = \frac{t^*}{\sqrt{2d}} = \frac{t^*}{\sqrt{z}}. \quad (2.20)$$

As a result, the rescaled Hubbard model is

$$H = -\frac{t^*}{\sqrt{z}} c_{i\sigma}^\dagger c_{j\sigma} + U \sum_i n_{i\uparrow} n_{i\downarrow} - \mu \sum_{i\sigma} n_{i\sigma}, \quad (2.21)$$

possessing a well-defined $z \rightarrow \infty$ limit and maintaining the competition between H_{kin} and H_{int} .

Another way to derive this scaling is through a diagrammatic approach. One expresses the kinetic energy as the summation of propagators G_{ij} .

$$E_{\text{kin}} \equiv -\sum_{\langle ij \rangle} \frac{t^*}{\sqrt{z}} \langle c_i^\dagger c_j \rangle = -\lim_{t \rightarrow 0^+} \sum_{\langle ij \rangle} \frac{t^*}{\sqrt{z}} \int_{-\infty}^{\infty} \frac{d\omega}{2\pi i} G_{ij}(\omega) e^{i\omega t}. \quad (2.22)$$

As the sum over nearest neighbors gives an order z , and we expect the kinetic energy per site to be order 1 for infinite dimension, G_{ij} has to scale like

$$\begin{aligned} G_{ij} &\propto O\left(\frac{1}{\sqrt{z}}\right), \text{ for } |i-j|=1, \\ G_{ii} &\propto O(1). \end{aligned} \quad (2.23)$$

The above scaling leads to a crucial property of dynamical mean-field theory, namely the local nature of self-energy. This can be well illustrated by the perturbative expansion in real space [10, 11].

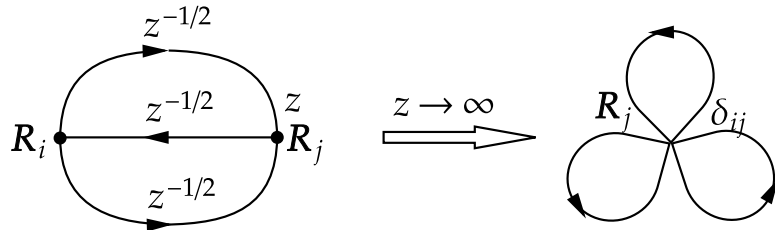


Figure 3: Example of second order diagram, each propagator contributes $z^{-1/2}$, three give $z^{-3/2}$. While the summation over the nearest neighbors gives z , finally leads to a factor of $z^{-1/2}$. When $z \rightarrow \infty$, all the diagrams higher than second order collapse.

In Fig. 3, two different internal vertices are connected by at least three independent propagators, which gives a factor of $(1/\sqrt{z})^3 = z^{-3/2}$. Since the summation over nearest neighbors introduces a factor of z , the resulting non-local contribution from the skeleton expansion decays as $z \times z^{-3/2} = z^{-1/2}$, and all diagrams with

higher-order interactions eventually collapse to a single-site propagator in the infinite z limit. As a consequence, the self-energy becomes a purely local quantity in real space.

$$\Sigma_{ij}(\omega) \rightarrow \Sigma_{ij}(\omega)\delta_{ij}, \quad (2.24)$$

as it is fully diagonal in real space representation, the Fourier transform is momentum independent

$$\Sigma_{\mathbf{k}}(\omega) \rightarrow \Sigma(\omega). \quad (2.25)$$

The locality of $\Sigma(\omega)$ is reminiscent of the Ising mean-field $m = \langle S \rangle$, which is also a local quantity and encodes interactions between a site and its neighbors. It turns out that the so-called hybridization function $\Gamma(\omega)$, defined from an effective impurity model, plays the same role as the Weiss mean-field. $\Gamma(\omega)$ consists of $\Sigma(\omega)$, and both are solved self-consistently in the DMFT procedure.

2.3 Green's function and self-energy

Before we elaborate on the practical procedure of DMFT, it is necessary to formally define the Green's function, self-energy, and spectral function.

The Green's function is a central concept in many-body physics, describing the propagation of an electron or excitation in a system. The retarded Green's function captures the probability amplitude of an electron's motion in space and time.

$$G_{ij}^R(t) = -i\Theta(t) \left\langle \{c_i(t), c_j^\dagger(0)\} \right\rangle, \quad (2.26)$$

where $\Theta(t)$ is the Heaviside function, and $c_i^{(\dagger)}(t)$ annihilates (creates) an electron occupying site i at time t . Here, the Green's function is defined in the real-space representation. Orbital and spin quantum numbers can be included within the subscript but are omitted in our definition for simplicity.

The Green's function in the frequency domain and momentum representation is more commonly used in DMFT.

$$G^R(\mathbf{k}, \omega) = \sum_{ij} \int_{-\infty}^{\infty} \frac{dt}{2\pi} e^{i\omega t} e^{i\mathbf{k}(\mathbf{R}_i - \mathbf{R}_j)} G_{ij}^R(t). \quad (2.27)$$

The local Green's function $G(\omega)$ plays a crucial role in DMFT and describes the electronic correlations by mapping a lattice problem to an impurity problem.

$$\begin{aligned} G(\omega) &= \frac{1}{N} \sum_{\mathbf{k}} G(\mathbf{k}, \omega) \\ &= \int_{BZ} \frac{d^d \mathbf{k}}{(2\pi)^d} G(\mathbf{k}, \omega), \end{aligned} \quad (2.28)$$

which is an average over the first Brillouin zone and we have omitted the superscript R .

The self-energy represents the effects of interactions between electrons. It modifies the bare Green's function into the interacting Green's function. The relationship between Green's function and self-energy is given by Dyson's equation

$$G(\mathbf{k}, \omega) = \frac{1}{\omega + \mu - \varepsilon_{\mathbf{k}} - \Sigma(\omega)}. \quad (2.29)$$

Here $\omega \equiv \omega + i\delta$ is implied to ensure causality and guarantees the convergence of the Fourier transformation in Eq. (2.27). μ is chemical potential, $\varepsilon_{\mathbf{k}}$ is the non-interacting dispersion and $\Sigma(\omega)$ the self-energy. One can easily tell the reminiscent of free Green's function via the Dyson's equation

$$G^{(0)}(\mathbf{k}, \omega) = \frac{1}{\omega + \mu - \varepsilon_{\mathbf{k}}}. \quad (2.30)$$

$\Sigma(\omega)$ modifies the non-interacting Green's function by adding itself to the dispersion. Since $\Sigma(\omega)$ is purely frequency-dependent, this simplification, as discussed in the previous section, is a key aspect of DMFT, where a local quantum impurity model is solved self-consistently.

The spectral function provides direct insight into the density of states and the excitations of the system. It is related to the imaginary part of the Green's function by:

$$A(\mathbf{k}, \omega) = -\frac{1}{\pi} \text{Im}G(\mathbf{k}, \omega). \quad (2.31)$$

$A(\mathbf{k}, \omega)$ gives the probability of adding or removing an electron with a specific energy and momentum. It reveals the structure of quasiparticle peaks, which describe coherent excitations, as well as incoherent features such as Hubbard bands.

In this thesis, $A(\mathbf{k}, \omega)$ provides key information about correlated systems, such as the formation of a Mott gap, the presence of quasiparticle states near the Fermi level, and other features arising from strong correlations.

As it serves the role of the density of states (DOS), which is a distribution function describing the probability of finding an electron at a given frequency (and thus energy in natural units) ω , $A(\omega)$ is normalized to 1.

$$\int_{-\infty}^{\infty} d\omega A(\omega) = 1. \quad (2.32)$$

Here $A(\omega)$ is from local Green's function $G(\omega)$, which is summed over \mathbf{k} and is only frequency relevant.

2.4 Effective impurity problem

Given the definitions of self-energy and Green's function, we now discuss how to compute these central quantities. A significant simplification was proposed in 1992 by A. Georges and G. Kotliar [3]: a lattice model, such as the Hubbard model, can be mapped onto an effective quantum impurity model and solved in a self-consistent manner.

This idea naturally arises from the locality of $\Sigma(\omega)$ in infinite dimensions [11]. As discussed in Section 2.2, the self-energy freezes out the momentum dependency when $d \rightarrow \infty$ and becomes completely local: $\Sigma_{\mathbf{k}}(\omega) = \Sigma(\omega)$. This provides a picture where a single site, with on-site Coulomb interaction $Un_{\uparrow}n_{\downarrow}$, is surrounded by an infinite number of neighbors as the dimension becomes infinite. The number of neighbors is so large that the local environment becomes very similar for all sites. Consequently, the relative position of a site becomes less important, as the hopping to each individual neighbor becomes weaker ($t \sim 1/\sqrt{d}$). The contribution from each neighboring site tends to average out, resulting in a local environment that is spatially homogeneous.

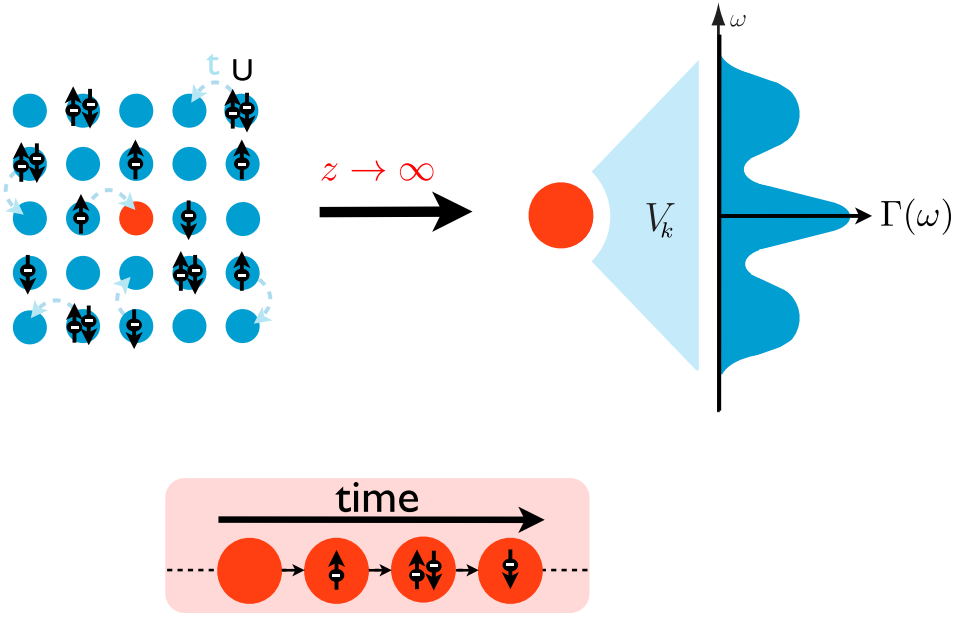


Figure 4: **Upper panel:** Mapping a lattice problem onto an effective impurity model, where the impurity site (red circle) interacts with a bath through the hybridization function, $\Gamma(\omega)$. **Lower panel:** In single-site DMFT, only temporal correlations of the system are captured. The figure is taken from Ref. Stadler2013.

The goal of DMFT is to find out an approach to calculate $\Sigma(\omega)$, to be more specific the lattice self-energy $\Sigma_{\text{latt}}(\omega)$. It is defined from the full interacting Green's function via Dyson's equation

$$G_{\text{latt}}(\mathbf{k}, \omega) = \frac{1}{\omega + \mu - \varepsilon_{\mathbf{k}} - \Sigma_{\text{latt}}(\omega)}. \quad (2.33)$$

The local (also known as site-diagonal) Green's function can be obtained by either summing over \mathbf{k} , or integrating over ε via a weight $\rho_{\text{latt}}(\omega)$, i.e. density of states

$$\begin{aligned} G_{\text{latt}}(\omega) &= \int_{\text{BZ}} \frac{d^d \mathbf{k}}{(2\pi)^d} G_{\text{latt}}(\mathbf{k}, \omega) \\ &= \int_{-\infty}^{+\infty} d\varepsilon \frac{\rho_{\text{latt}}(\omega)}{\omega + \mu - \varepsilon - \Sigma_{\text{latt}}(\omega)}. \end{aligned} \quad (2.34)$$

To compute $\Sigma_{\text{latt}}(\omega)$ an auxiliary impurity problem is considered via the action [3]

$$S_{\text{imp}} = U \int_0^\beta d\tau n_\uparrow(\tau)n_\downarrow(\tau) - \int_0^\beta d\tau \int_0^\beta d\tau' \sum_\sigma c_\sigma^\dagger(\tau) G_{0,\text{imp}}^{-1}(\tau - \tau') c_\sigma(\tau'). \quad (2.35)$$

Here $G_{0,\text{imp}}$ is the bare Green's function excluding Coulomb interaction on the impurity site. But it has to be pointed out that $G_{0,\text{imp}}$ includes hybridization caused by hopping to the environment, i.e. $\Delta(\omega)$

$$G_{0,\text{imp}}^{-1}(\omega) = \omega + \mu - \Delta(\omega). \quad (2.36)$$

The impurity has its corresponding self-energy $\Sigma_{\text{imp}}(\omega)$ from U term as well. Consequently, the full interacting Green's function of this impurity problem is given by

$$G_{\text{imp}}(\omega) = \frac{1}{G_{0,\text{imp}}(\omega)^{-1} - \Sigma_{\text{imp}}(\omega)} = \frac{1}{\omega + \mu - \Delta(\omega) - \Sigma_{\text{imp}}(\omega)}. \quad (2.37)$$

DMFT requires that the full interacting Green's function of the original lattice model Eq. (2.34) coincides with that of impurity problem Eq. (2.37). This reads:

$$G_{\text{imp}}(\omega) \stackrel{!}{=} G_{\text{latt}}(\omega). \quad (2.38)$$

In this sense, self-energies coincide as well

$$\Sigma_{\text{imp}}(\omega) = \Sigma_{\text{latt}}(\omega). \quad (2.39)$$

as local interactions are the same $Un_\uparrow n_\downarrow$ and only local effects enter the self-energy. As a result, the lattice Green's function Eq. (2.40) combined with Eq. (2.37) and Eq. (2.38) can be cast into

$$\begin{aligned} G_{\text{latt}}(\omega) &\stackrel{!}{=} \int_{-\infty}^{+\infty} d\varepsilon \frac{\rho_{\text{latt}}(\omega)}{\omega + \mu - \varepsilon - \Sigma_{\text{imp}}(\omega)} \\ &= \frac{1}{\omega + \mu - \Delta(\omega) - \Sigma_{\text{imp}}(\omega)}. \end{aligned} \quad (2.40)$$

One should note that the nature of the lattice enters the above equation only through the density of states $\rho_{\text{latt}}(\omega)$, and on the right-hand side, the lattice self-energy is replaced by the impurity self-energy. The equation above is referred to as a mean-field equation, which resembles Eq. (2.12) in the Ising mean-field solution, $m = \tanh(\beta h_{\text{eff}})$. The right-hand side (RHS) represents the input of a trial solution, i.e., h_{eff} or $\Delta(\omega)$, while the left-hand side (LHS) represents the quantity one wants to calculate, i.e., m or $G_{\text{latt}}(\omega)$. The equation is considered converged only when the LHS coincides with the RHS. With an initial guess for $\Delta(\omega)$, the solution for $\Sigma_{\text{imp}}(\omega)$ can be initiated via an impurity model, thus continuing the self-consistent process.

Eq. (2.38) is also known as the DMFT self-consistent condition and has a natural physical interpretation. As a mean-field approach that freezes out spatial fluctuations $\Sigma_{\mathbf{k}}(\omega) = \Sigma(\omega)$, one-particle properties can be obtained by focusing on a single fixed site of the lattice $G_{\text{latt}}(\omega) = G_{\text{imp}}(\omega)$ [3], and this site is regarded as the impurity embedded in a non-interacting bath. Given that the original model is itinerant, one must take temporal fluctuations into account (hence the term, dynamic). The fixed site undergoes fluctuations between empty, singly occupied, and doubly occupied states. Such quantum dynamical processes are effectively described by $\Delta(\omega)$, which encapsulates the hybridization between the impurity and the bath. Therefore, $\Delta(\omega)$ can be regarded as the effective mean-field h_{eff} that interacts with the local spin S in the Ising model.

Single impurity Anderson model (SIAM)

The effective impurity problem corresponding to the single-band Hubbard model is the single impurity Anderson model (SIAM) [12]

$$\begin{aligned}
 H_{SIAM} &= H_{\text{bath}} + H_{\text{imp}} + H_{\text{imp-bath}} \\
 &= \sum_{\sigma\mathbf{k}} \varepsilon_{\mathbf{k}} b_{\mathbf{k}\sigma}^{\dagger} b_{\mathbf{k}\sigma} \\
 &\quad + \sum_{\sigma} \varepsilon_f f_{\sigma}^{\dagger} f_{\sigma} + U f_{\uparrow}^{\dagger} f_{\uparrow} f_{\downarrow}^{\dagger} f_{\downarrow} \\
 &\quad + \sum_{\mathbf{k}\sigma} V_{\mathbf{k}} (f_{\sigma}^{\dagger} b_{\mathbf{k}\sigma} + b_{\mathbf{k}\sigma}^{\dagger} f_{\sigma}),
 \end{aligned} \tag{2.41}$$

where $f_{\sigma}^{(\dagger)}$ annihilates (creates) an electron with spin σ at the impurity site, $b_{\mathbf{k}\sigma}^{(\dagger)}$ corresponds to annihilation (creation) operator of the non-interacting bath electrons. Hybridization between the impurity and the bath is described by $V_{\mathbf{k}}$. As the bath terms are quadratic, they can be integrated out from H_{SIAM} , yielding an effective Hamiltonian that contains impurity operators $f_{\sigma}^{(\dagger)}$ only, hopping in and out the impurity is described by a hybridization function $\Delta(\omega)$, the expression can be derived via functional integral as follows.

We now ignore the Coulomb interaction term and focus on the non-interacting parts only, the action is

$$S_0 = \int_0^{\beta} d\tau \sum_{\mathbf{k}} \{ b_{\mathbf{k}}^{\dagger}(\tau) (\partial_{\tau} + \varepsilon_{\mathbf{k}}) b_{\mathbf{k}}(\tau) + \varepsilon_f f^{\dagger}(\tau) f(\tau) + V_{\mathbf{k}} [f^{\dagger}(\tau) b_{\mathbf{k}}(\tau) + b_{\mathbf{k}}^{\dagger}(\tau) f(\tau)] \}. \tag{2.42}$$

For simplification, subscripts of spin are omitted. We first go to Matsubara frequency space via Fourier transformation

$$b_{\mathbf{k}}(\tau) = \frac{1}{\sqrt{\beta}} \sum_{i\omega_n} b_{\mathbf{k}}(i\omega_n) e^{-i\omega_n \tau}, \tag{2.43a}$$

$$f(\tau) = \frac{1}{\sqrt{\beta}} \sum_{i\omega_n} f(i\omega_n) e^{-i\omega_n \tau}. \tag{2.43b}$$

The action becomes

$$S_0 = \sum_{\mathbf{k}, i\omega_n} b_{\mathbf{k}}^\dagger(i\omega_n)(i\omega_n - \varepsilon_{\mathbf{k}})b_{\mathbf{k}}(i\omega_n) + \varepsilon_d f^\dagger(i\omega_n)f(i\omega_n) + V_{\mathbf{k}}[b_{\mathbf{k}}^\dagger(i\omega_n)f(i\omega_n) + f^\dagger(i\omega_n)b_{\mathbf{k}}(i\omega_n)].$$

We want to integrate out $b_{\mathbf{k}}$ field and make it decouple from f field, hence we define

$$B_{\mathbf{k}} = b_{\mathbf{k}} + \frac{fV_{\mathbf{k}}}{i\omega_n - \varepsilon_{\mathbf{k}}}, \quad (2.45a)$$

$$B_{\mathbf{k}}^\dagger = b_{\mathbf{k}}^\dagger + \frac{V_{\mathbf{k}}^* f^\dagger}{-i\omega_n - \varepsilon_{\mathbf{k}}}. \quad (2.45b)$$

Substituting $B_{\mathbf{k}}^{(\dagger)}$ field to the action yields

$$S_{\text{imp-bath}} = \sum_{\mathbf{k}, i\omega_n} B_{\mathbf{k}}^\dagger(i\omega_n - \varepsilon_{\mathbf{k}})B_{\mathbf{k}} + f^\dagger(i\omega_n - \varepsilon_f - \frac{V_{\mathbf{k}}^2}{i\omega_n - \varepsilon_{\mathbf{k}}})f. \quad (2.46)$$

Note in the first term, the auxiliary field $B_{\mathbf{k}}$ is completely decoupled from f , in the second term, f field acquires additional momentum-dependency, encoding the hybridization between f and $b_{\mathbf{k}}$.

Given the decoupled action $S_{\text{imp-bath}}$, $B_{\mathbf{k}}$ term can be integrated out, yielding an effective action merely about f

$$\begin{aligned} Z_0 &= \int D[B_{\mathbf{k}}^\dagger, B_{\mathbf{k}}] \int D[f^\dagger, f] e^{-S_{\text{imp-bath}}} \\ &= \int D[B_{\mathbf{k}}^\dagger, B_{\mathbf{k}}] \exp\left\{-\sum_{\mathbf{k}, i\omega_n} B_{\mathbf{k}}^\dagger(i\omega_n - \varepsilon_{\mathbf{k}})B_{\mathbf{k}}\right\} \\ &\times \int D[f^\dagger, f] \exp\left\{-\sum_{\mathbf{k}, i\omega_n} f^\dagger(i\omega_n - \varepsilon_f - \frac{V_{\mathbf{k}}^2}{i\omega_n - \varepsilon_{\mathbf{k}}})f\right\} \\ &= \det(i\omega_n - \varepsilon_{\mathbf{k}}) \int D[f^\dagger, f] e^{-S_{\text{eff}}}. \end{aligned} \quad (2.47)$$

Finally we arrive at the effective action

$$S_{\text{eff}} = -\sum_{\mathbf{k}, i\omega_n} f^\dagger(i\omega_n - \varepsilon_f - \frac{V_{\mathbf{k}}^2}{i\omega_n - \varepsilon_{\mathbf{k}}})f, \quad (2.48)$$

and define the hybridization function

$$\Delta(\omega) = \sum_{\mathbf{k}} \frac{V_{\mathbf{k}}^2}{\omega - \varepsilon_{\mathbf{k}}}, \quad (2.49)$$

note that we have transferred from Matsubara frequency back to real frequency, where $\omega \equiv \omega + i\delta$ is implied. Since $\Delta(\omega)$ is causal and analytic in the upper

complex half-plane, the real part and imaginary part are related via the Kramers-Kronig relations, thus only the imaginary part is considered conventionally.

$$\Gamma(\omega) = -\text{Im}\Delta(\omega) = \pi \sum_{\mathbf{k}} V_{\mathbf{k}}^2 \delta(\omega - \varepsilon_{\mathbf{k}}). \quad (2.50)$$

From now, $\Gamma(\omega)$ instead of $\Delta(\omega)$ plays the role of hybridization function, and is the analogy of the Weiss field in Ising mean-field solution. As discussed before, $\Gamma(\omega)$, $\Sigma(\omega)$ and hence $G_{\text{latt}}(\omega)$ have to be determined self-consistently.

2.5 The self-consistency procedure

As explained in the last section, now the hybridization function is defined as Eq. (2.50). Combined with Eq. (2.40) we have

$$\begin{aligned} \Gamma(\omega) &= -\text{Im}\Delta(\omega) \\ &= \text{Im}(G_{\text{latt}}^{-1}(\omega) + \Sigma(\omega)), \end{aligned} \quad (2.51)$$

here $\Sigma(\omega) = \Sigma_{\text{imp}}(\omega) = \Sigma_{\text{latt}}(\omega)$. An iterative procedure that resembles Ising mean-field solution in section 2.1 can be devised

- (i) initiate the DMFT procedure with a guess hybridization $\Gamma_{\text{in}}(\omega)$
- (ii) solve the impurity problem with input $\Gamma_{\text{in}}(\omega)$ to determine $\Sigma(\omega)$
- (iii) evaluate the local lattice Green's function $G_{\text{latt}}(\omega) = \int_{BZ} \frac{d^d \mathbf{k}}{(2\pi)^d} \frac{1}{\omega + \mu - \varepsilon_{\mathbf{k}} - \Sigma(\omega)}$
- (iv) update the hybridization function $\Gamma_{\text{out}}(\omega) = \text{Im}(G_{\text{latt}}^{-1}(\omega) + \Sigma(\omega))$
- (v) compare Γ_{out} and Γ_{in} , if it converges, break out the procedure. If not, repeat from (ii) and take Γ_{out} as the input hybridization until convergence

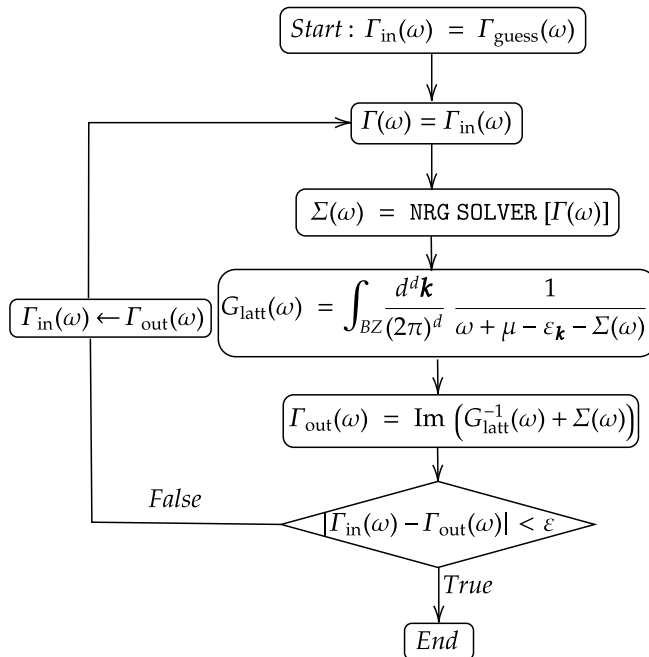


Figure 5: A flowchart illustrating the DMFT procedure: Starting with a trial hybridization function $\Gamma_{\text{guess}}(\omega)$, the impurity model is solved to obtain the self-energy $\Sigma(\omega)$, with which the lattice Green's function and the impurity Green's function are then equated. This process is iteratively repeated until the hybridization function converges.

In recent decades, a variety of techniques have been developed to address quantum impurity problems. Among these, Quantum Monte Carlo (QMC) methods, especially the continuous-time version (CTQMC), have gained widespread use due to their statistical accuracy, scalability to multi-orbital models, and straightforward parallel implementation [13]. While CTQMC is a powerful approach, its reliance on imaginary-time data necessitates analytic continuation, a process known to be numerically unstable, which compromises the precision of spectral functions. Furthermore, QMC methods become computationally demanding at low temperatures and are significantly affected by the sign problem, which poses severe challenges for solving certain multi-orbital problems due to its exponentially increasing sampling complexity. This thesis mainly studies the zero-temperature behavior of the (three-band) Hubbard model, and consequently, a more suitable impurity solver is needed.

The Numerical Renormalization Group (NRG) method, pioneered by Wilson [7], is exploited as a primary tool for solving quantum impurity problems. NRG offers the distinct advantage of delivering results directly on the real-frequency axis while also achieving very low energy or temperature resolutions. The main challenge with NRG lies in its limited scalability for multi-orbital models. Nevertheless, our research group utilizes an advanced NRG code developed by S.-S.B. Lee, which is optimized to handle complex systems through the use of both

Abelian and non-Abelian symmetries, using the tensor network library developed by A. Weichselbaum [14, 15, 16]. By exploiting these symmetries to the fullest extent, the computational efficiency is significantly enhanced, enabling the treatment of intricate multi-orbital scenarios. In the following chapter, we will provide a brief introduction to the fundamental principles of NRG.

2.6 Cluster extensions

Since single-site DMFT ignores all the momentum dependence of the self-energy by averaging over the entire Brillouin zone, spatial correlations are lost. Nevertheless, there are some extension schemes to improve this drawback. Two typical methods are cellular dynamical mean-field theory (CDMFT) [4] and dynamical cluster approximation (DCA) [6]. In order to acquire and retain non-local correlations within the cluster, CDMFT clusterizes the lattice into small clusters in real space whereas DCA perform such clusterization in momentum space.

As shown in Fig. 6, the position of each cluster is labeled by \mathbf{x} , while the position within the cluster by \mathbf{X} . In momentum space, \mathbf{k} and \mathbf{K} label the momentum with respect to \mathbf{x} and \mathbf{X} .

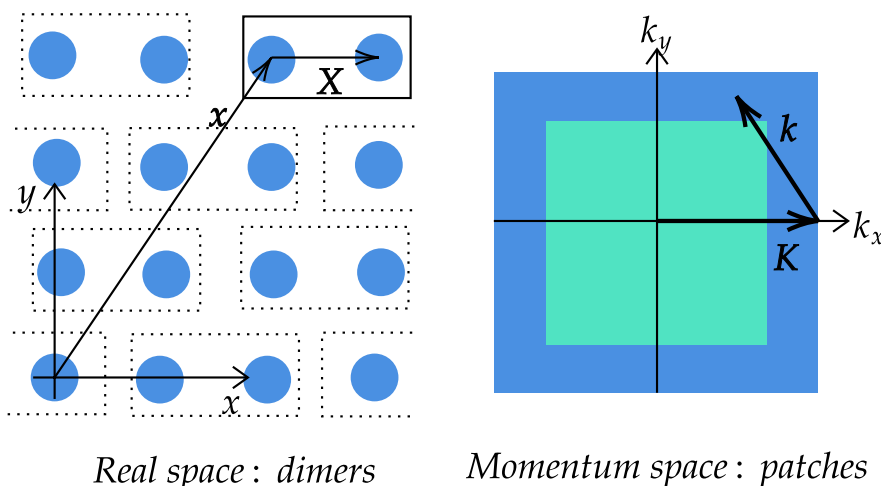


Figure 6: **Left panel:** A square lattice partitioned into dimers, with \mathbf{x} denoting the unit cell positions and \mathbf{X} representing the intracell coordinates. **Right panel:** The corresponding Brillouin zone divided into two patches, where \mathbf{k} specifies the lattice momentum and \mathbf{K} indicates the superlattice momentum.

Cellular dynamical mean-field theory (CDMFT)

In CDMFT [17], the original lattice is firstly tiled into a superlattice containing N_c sites. The translational symmetry is retained in the superlattice but violated because of the clusterization. Consequently, the Green's function and self-energy are formulated as $N_c \times N_c$ matrices, labeled by intra-cluster indices X_i and X_j . The full Green's function has the form:

$$\mathbf{G}(\mathbf{k}, \omega) = \{\mathbf{G}_0^{-1}(\mathbf{k}, \omega) - \boldsymbol{\Sigma}(\mathbf{k}, \omega)\}^{-1}, \quad (2.52)$$

where $\mathbf{G}_0(\mathbf{k}, \omega)$ is non-interacting Green's function

$$\mathbf{G}_0(\mathbf{k}, \omega) = \{(\omega + \mu)\mathbf{1} - \mathbf{t}(\mathbf{k})\}^{-1}. \quad (2.53)$$

Here the intra-cell hopping is captured by matrix element $\mathbf{t}(\mathbf{k})_{X_i X_j}$, which is the Fourier transform of the lattice dispersion $\varepsilon_{\mathbf{k}+\mathbf{K}}$ with respect to the supermomentum \mathbf{K}

$$\mathbf{t}(\mathbf{k})_{X_i X_j} = \frac{1}{N_c} \sum_{\mathbf{K}} \exp(i(\mathbf{k} + \mathbf{K})(\mathbf{X}_i - \mathbf{X}_j)) \varepsilon_{\mathbf{k}+\mathbf{K}}. \quad (2.54)$$

Take $N_c = 2$ as an example, in this case the lattice is clusterized into two-site dimers along \mathbf{e}_x . As a result, $\mathbf{X}_1 = \mathbf{0}, \mathbf{X}_2 = \mathbf{e}_x$ and $\mathbf{K}_1 = \mathbf{0}, \mathbf{K}_2 = \frac{2\pi}{N_c} \mathbf{e}_x$. Inserted into Eq. (2.54) this yields

$$\mathbf{t}(\mathbf{k}) = \begin{pmatrix} 0 & e^{ik_x \varepsilon_{\mathbf{k}}} \\ e^{-ik_x \varepsilon_{\mathbf{k}}} & 0 \end{pmatrix}. \quad (2.55)$$

The exponential factor $e^{\pm ik_x}$ arises from the wave nature of the electron and explicitly breaks the translational invariance within the cluster. When the electron hops from \mathbf{X}_1 to \mathbf{X}_2 , it acquires a phase factor e^{+ik_x} , and when it hops from \mathbf{X}_2 to \mathbf{X}_1 , it acquires the opposite phase e^{-ik_x} . Additionally, the dimers arranged along \mathbf{e}_x also break the inter-cell symmetry.

Moreover, the self-energy $\Sigma(\mathbf{k}, \omega)$ within the DMFT framework is to be solved self-consistently from an effective impurity model. However, the impurity self-energy is purely a function of frequency. Therefore, we continue to apply the dynamical mean-field approximation (DMFA), i.e., $\Sigma(\mathbf{k}, \omega) \approx \Sigma(\omega)$, so that only $\mathbf{t}(\mathbf{k})$ depends on momentum. With the above equations, the local Green's function now reads:

$$\mathbf{G}_{\text{latt}}(\omega) = \int_{BZ} \frac{d^d \mathbf{k}}{(2\pi)^d} \{\mathbf{G}_0^{-1}(\mathbf{k}, \omega) - \Sigma(\omega)\}^{-1}. \quad (2.56)$$

The self-consistent procedure follows in the same way as described in single-site DMFT. The only difference in this case is that the corresponding impurity model is the two-impurity Anderson model (2IAM), rather than SIAM.

$$\begin{aligned} H &= H_{\text{cluster}} + H_{\text{bath}} + H_{\text{hyb}}, \\ H_{\text{cluster}} &= -t \sum_{\sigma} \left(c_{1\sigma}^{\dagger} c_{2\sigma} + \text{h.c.} \right) + U \sum_{\alpha} n_{\alpha\uparrow} n_{\alpha\downarrow} - \mu \sum_{\alpha, \sigma} n_{\alpha\sigma}, \\ H_{\text{bath}} &= \sum_{\alpha, \mathbf{k}, \sigma} \varepsilon_{\mathbf{k}\alpha} a_{\mathbf{k}\alpha\sigma}^{\dagger} a_{\mathbf{k}\alpha\sigma}, \\ H_{\text{hyb}} &= \sum_{\alpha, \beta, \mathbf{k}, \sigma} \left(V_{\mathbf{k}\alpha\beta} c_{\alpha\sigma}^{\dagger} a_{\mathbf{k}\beta\sigma} + \text{h.c.} \right). \end{aligned} \quad (2.57)$$

Here, $\alpha, \beta = 1, 2$ are cluster indices. The hybridization function follows a similar form as Eq. (2.49):

$$\Delta_{\alpha\beta}(\omega) = \sum_{\gamma, \mathbf{k}} \frac{V_{\mathbf{k}\alpha\gamma} V_{\mathbf{k}\beta\gamma}^*}{\omega - \varepsilon_{\mathbf{k}\gamma}}. \quad (2.58)$$

After the solution of the impurity model is initiated by a guess for the hybridization function $\Delta(\omega)$, one obtains $\Sigma(\omega)$ and can evaluate the cluster (impurity) Green's function

$$\mathbf{G}_{\text{cluster}}(\omega) = \{(\omega + \mu)\mathbf{1} - t \cdot \boldsymbol{\sigma}_x - \Delta(\omega) - \Sigma(\omega)\}^{-1}, \quad (2.59)$$

where $t \cdot \boldsymbol{\sigma}_x$ describes the intra-cell hopping. Equating Eq. (2.56) and Eq. (2.59) gives the self-consistence equation

$$\mathbf{G}_{\text{cluster}}(\omega) \stackrel{!}{=} \mathbf{G}_{\text{latt}}(\omega). \quad (2.60)$$

This is reached by iterating the 2IAM with hybridization function $\Gamma(\omega)$, defined by

$$\begin{aligned} \Delta(\omega) &= (\omega + \mu)\mathbf{1} - t \cdot \boldsymbol{\sigma}_x - \mathbf{G}_{\text{cluster}}^{-1}(\omega) - \Sigma(\omega), \\ \Gamma(\omega) &= -\text{Im}\Delta(\omega). \end{aligned} \quad (2.61)$$

The self-energy $\Sigma(\omega)$ is not necessarily diagonal in momentum space, as clusterization breaks the translational invariance. Therefore a reperiodization scheme is needed, see Ref. [18] and Ref. [19].

Dynamical cluster approximation (DCA)

In CDMFT, translational invariance over the entire lattice is broken by clusterization, as only surface sites hybridize with the host [6]. Therefore, the dynamical cluster approximation (DCA) is introduced to address this issue and can restore intra-cell translational invariance. The cause of this violation can be traced back to Eq. (2.54), where the phase factor $e^{\pm ik_x}$ explicitly breaks translational symmetry. To recover translational invariance within the cluster, another Fourier transform is applied

$$\begin{aligned} \mathbf{t}(\mathbf{k})_{X_i X_j}^{\text{DCA}} &= \mathbf{t}(\mathbf{k})_{X_i X_j} e^{-i\mathbf{k}(\mathbf{X}_i - \mathbf{X}_j)} \\ &= \frac{1}{N_c} \sum_{\mathbf{K}} \exp(i\mathbf{K}(\mathbf{X}_i - \mathbf{X}_j)) \varepsilon_{\mathbf{k}+\mathbf{K}} \\ &= \begin{pmatrix} 0 & \varepsilon_{\mathbf{k}} \\ \varepsilon_{\mathbf{k}} & 0 \end{pmatrix}. \end{aligned} \quad (2.62)$$

Such a Fourier transform is equivalent to a periodic boundary condition within each cluster. Now the phase factors $e^{\pm ik_x}$ in Eq. (2.54) are eliminated, and these hopping integrals retain translational invariance within the cluster, hence the lattice Green's function becomes diagonal in cluster Fourier space

$$G_{\text{latt}}(\mathbf{K}, \mathbf{k}, \omega) = \{\omega + \mu - \varepsilon_{\mathbf{K}+\mathbf{k}} - \Sigma(\mathbf{K}, \omega)\}^{-1}. \quad (2.63)$$

Here, the notation for Green's function and self-energy is no longer in bold font, in contrast to Eq. (2.52), because the matrix is diagonal, and the superlattice momentum \mathbf{K} , playing the role of diagonal indices K_i , suffices to indicate the matrix element. Straightforwardly, the local Green's function reads

$$G_{\text{latt}}(\mathbf{K}, \omega) = \int_{P_i} \frac{d^d \mathbf{k}}{\Omega_{P_i}} \{\omega + \mu - \varepsilon_{\mathbf{K}+\mathbf{k}} - \Sigma(\mathbf{K}, \omega)\}^{-1}, \quad (2.64)$$

where P_i denotes the momentum patch in Brillouin zone, corresponding to superlattice momentum \mathbf{K}_i . Ω_{P_i} is the volume of patch P_i . A possible division of Brillouin zone is shown in the right panel of Fig. 6, number of patches equals the number of cluster sites N_c . A larger N_c leads to a larger cluster, hence takes more spacial correlations into account.

To complete the DMFT self-consistence procedure, one still needs the cluster Green's function

$$G_{\text{cluster}}(\mathbf{K}, \omega) = \{\omega + \mu - \bar{\varepsilon}_{\mathbf{K}} - \Delta(\mathbf{K}, \omega) - \Sigma(\mathbf{K}, \omega)\}^{-1}, \quad (2.65)$$

where $\bar{\varepsilon}_{\mathbf{K}}$ is the integrated dispersion over the patch covering \mathbf{K} :

$$\bar{\varepsilon}_{\mathbf{K}} = \int_{P_i} \frac{d^d \mathbf{k}}{\Omega_{P_i}} \varepsilon_{\mathbf{K}+\mathbf{k}}. \quad (2.66)$$

Equating Eq. (2.65) and Eq. (2.66) gives the self-consistency equation

$$G_{\text{cluster}}(\mathbf{K}, \omega) \stackrel{!}{=} G_{\text{latt}}(\mathbf{K}, \omega). \quad (2.67)$$

The hybridization function can be extracted from Eq. (2.66) and fed into the next round of 2IAM solution until it converges.

In DCA, even though the periodicity is restored within each momentum patch P_i , one has to note that the continuity between patches is lost. Thus we need interpolation.

Interpolation schemes

As DCA divides the momentum space into discrete patches, each patch is mapped to a cluster momentum K_i . This allows DCA to approximate the full lattice by solving a finite-sized cluster. In this thesis, a dimer consisting of two impurity sites is implemented, which results in a dichotomy of the Brillouin zone, with relevant quantities labeled by \pm , corresponding to the central and border regions, as shown in the right panel of Fig. 6. However, it is necessary to post-process the resulting self-energies $\Sigma_{\pm}(\omega)$ on these discrete patches P_{\pm} . An interpolation scheme is required to bridge the lattice self-energy $\Sigma_{\text{latt}}(\mathbf{k}, \omega)$, defined in continuous momentum space, and the patch self-energies $\Sigma_{\pm}(\omega)$, which only account for a few momentum points.

A standard method Σ *interpolation* reads [5]

$$\Sigma_{\text{latt}}(\mathbf{k}, \omega) = \alpha_+(\mathbf{k})\Sigma_+(\omega) + \alpha_-(\mathbf{k})\Sigma_-(\omega), \quad (2.68)$$

where $\alpha_{\pm}(\mathbf{k})$ are weights with respect to the patches P_{\pm} , and insert momentum dependency by

$$\alpha_{\pm}(\mathbf{k}) = \frac{1}{2} \{1 \pm \frac{1}{2} [\cos(k_x) + \cos(k_y)]\}. \quad (2.69)$$

The cosine function $[\cos(k_x) + \cos(k_y)]$ originates from the dispersion of a square lattice

$$\varepsilon_{\mathbf{k}} = -2t \sum_{i=1}^d \cos(k_i). \quad (2.70)$$

Such a weight factor reflects the underlying symmetry and periodicity of the 2D square lattice, and ensures that the interpolation respects the lattice geometry.

When \mathbf{k} falls in the inner patch P_+ , which is close to $K_+ = (0, 0)$ point, the weight function $\alpha_+(\mathbf{k})$ gives a maximum, likewise when \mathbf{k} falls in the outer patch that contains $K_- = (\pi, \pi)$, $\alpha_+(\mathbf{k})$ dominates.

$$\begin{aligned}\alpha_+(\mathbf{k} \rightarrow K_+) &= \frac{1}{2} \left\{ 1 + \frac{1}{2} [\cos(0) + \cos(0)] \right\} = 1, \\ \alpha_-(\mathbf{k} \rightarrow K_-) &= \frac{1}{2} \left\{ 1 - \frac{1}{2} [\cos(\pi) + \cos(\pi)] \right\} = 1.\end{aligned}\tag{2.71}$$

In other words, the weight function $\alpha_{\pm}(\mathbf{k})$ maximizes whenever \mathbf{k} encounters representative momenta K_{\pm} in each patch P_{\pm} , reproduces the value of $\Sigma_{\pm}(\omega)$ faithfully and takes the original lattice symmetry into account when \mathbf{k} goes away K_{\pm} .

In this thesis, an alternative interpolation scheme, cumulant *M interpolation* is used. It obeys the similar principle as Σ *interpolation*, but interpolates the other quantity, i.e. cumulant $M_{\text{latt}}(\mathbf{k}, \omega)$ rather than $\Sigma_{\text{latt}}(\mathbf{k}, \omega)$

$$M_{\text{latt}}(\mathbf{k}, \omega) = \alpha_+(\mathbf{k})M_+(\omega) + \alpha_-(\mathbf{k})M_-(\omega),\tag{2.72}$$

here $M_{\pm}(\omega)$ resemble a propagator without dispersion but includes self-energy

$$M_{\pm} = \frac{1}{\omega + \mu - \Sigma_{\pm}(\omega)}.\tag{2.73}$$

From $M_{\text{latt}}(\mathbf{k}, \omega)$, it is then possible to extract a lattice self-energy

$$\Sigma_{\text{latt}}(\mathbf{k}, \omega) = \omega + \mu - M_{\text{latt}}(\mathbf{k}, \omega)^{-1}.\tag{2.74}$$

To summarize, Σ *interpolation* is more suitable for weak coupling, as it corresponds to an expansion around the free electron limit, whereas *M interpolation* works better at strong coupling [5], as the cumulant is more local than the self-energy itself when it is close to a Mott insulating state.

3 Numerical Renormalization Group (NRG)

3.1 Introduction to NRG

The Kondo effect is a fascinating phenomenon in condensed matter physics [20], characterized by the behavior of magnetic impurities in a metal. It emerged from the quantum impurity model, which describes the interaction between a localized magnetic moment (the impurity) and the conduction electrons in a metallic host. The Kondo effect cannot be simply deduced, but requires a deeper understanding of the complex correlations that arise when the impurity's magnetic moment interacts with the surrounding electronic environment. Specifically, the screening of the impurity's magnetic moment occurs below a characteristic temperature known as the Kondo temperature (T_K), necessitating sophisticated numerical techniques to investigate.

One such technique is the Numerical Renormalization Group (NRG), a fully non-perturbative method developed by K.G. Wilson in the 1970s [7]. NRG has significantly advanced our understanding of the Kondo effect and related phenomena. Designed specifically for quantum impurity systems, NRG has evolved into the most reliable numerical algorithm for analyzing these systems, where one or more interacting magnetic impurities, characterized by a limited number of degrees of freedom and arbitrary interaction forms, are coupled to a non-interacting metallic bath. Although each component—the impurity and the metallic bath—can, in principle, be solved exactly, the coupling between them gives rise to intricate correlation effects that cannot be easily resolved.

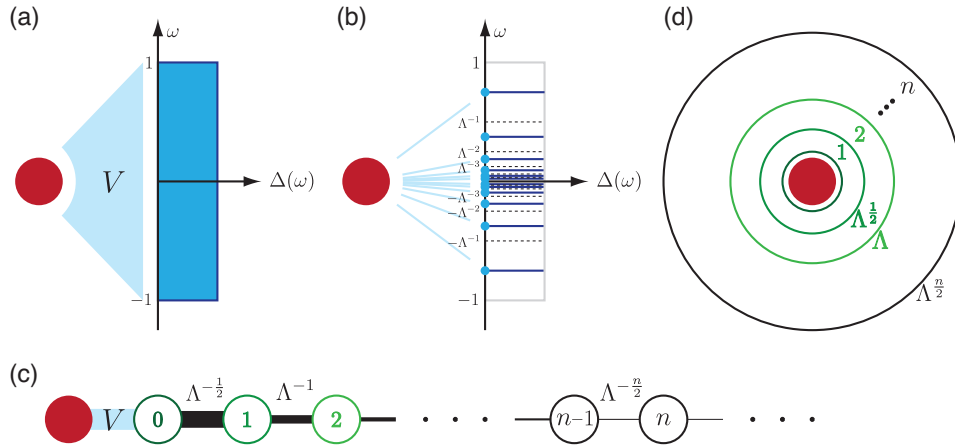


Figure 7: (a) Impurity model: an impurity coupled to a bath with strength V , the hybridization in frequency domain is described by $\Delta(\omega)$. (b) Logarithmic discretization of the frequency axis. (c) Mapping to a Wilson chain, where the impurity is coupled to the first bath site with strength V , hopping amplitudes between the chain sites decrease exponentially. (d) Physical interpretation of Wilson chain: a sequence of shells with exponentially growing radius, centering around the impurity site. The figure is taken from Ref. [21]

The versatility of impurity models allows for the exploration of a vast array of physical phenomena by varying system parameters and energy scales. As a renormalization group method, NRG effectively addresses these varying energy scales through successive diagonalization from high to low energies, making it a suitable candidate for impurity problems. Typically, any introduction to NRG follows a consistent structure, encompassing logarithmic discretization, mapping to a semi-infinite Wilson chain, and iterative diagonalization processes.

To illustrate the NRG methodology, it is logical to start with a prototype model, i.e. the single-impurity Anderson model (SIAM). This model enables a clear explanation of the standard NRG procedure without the complications introduced by multi-orbital systems. Multi-orbital effects are considered further in section 4.4).

An important consideration in impurity systems is the role of the geometry and dimensionality of the bath in which the impurity resides. Dimensionality profoundly influences the physical properties of many correlated systems. However, impurity systems can be treated as essentially one-dimensional problems, as the impurity interacts with a single channel of the bath. This issue will be addressed in detail when we discuss the mapping to a semi-infinite chain. The structure of this chapter aligns closely with Chapter 12 in Ref. [22], authored by Ralf Bulla.

3.2 The Single impurity Anderson model (SIAM)

The Hamiltonian of a most general quantum impurity model [12] consists of three parts, the interacting impurity H_{imp} , the non-interacting bath H_{bath} , and the coupling between them $H_{\text{imp-bath}}$

$$H = H_{\text{imp}} + H_{\text{bath}} + H_{\text{imp-bath}}. \quad (3.1)$$

For single band impurity model, the impurity Hamiltonian H_{imp} contains only a single level with the on-site energy $\varepsilon_f f_{\sigma}^{\dagger} f_{\sigma}$, and a Coulomb interaction term $U f_{\uparrow}^{\dagger} f_{\uparrow} f_{\downarrow}^{\dagger} f_{\downarrow}$. Two electrons occupying the same site must have opposite spin $\sigma = \downarrow$ and $\sigma = \uparrow$ due to Pauli's exclusion principle. Consequently one has

$$H_{\text{imp}} = \sum_{\sigma} \varepsilon_f f_{\sigma}^{\dagger} f_{\sigma} + U f_{\uparrow}^{\dagger} f_{\uparrow} f_{\downarrow}^{\dagger} f_{\downarrow}, \quad (3.2)$$

with f^{\dagger} annihilation (creation) operators for a electronic state with spin σ on the impurity site

The general form of the non-interacting bath H_{bath} is as follows:

$$H_{\text{bath}} = \sum_{\sigma} \sum_l \varepsilon_l c_{l\sigma}^{\dagger} c_{l\sigma} + \sum_{\sigma} \sum_{ij} t_{ij} (c_{i\sigma}^{\dagger} c_{j\sigma} + c_{j\sigma}^{\dagger} c_{i\sigma}), \quad (3.3)$$

where ε_l denotes the on-site energy at site l and t_{ij} the hopping between site i and j .

The impurity only couples to site $i = 0$ by construction, consequently the coupling term is written in the form $H_{\text{imp-bath}}$:

$$H_{\text{imp-bath}} = V \sum_{\sigma} (f_{\sigma}^{\dagger} c_{0\sigma} + c_{0\sigma}^{\dagger} f_{\sigma}). \quad (3.4)$$

With hybridization strength V . General coupling to even more bath sites will be discussed below.

The above Hamiltonian of SIAM is defined at lattice sites in real space, the transformation from real space to momentum space can be done by Fourier transform if the system has translational symmetry in space. For simplicity of notation, we assume that the bath has a finite size, therefore the transform to momentum representation is realized by diagonalizing H_{bath} , firstly we denote it in matrix form:

$$H_{\text{bath}} = \sum_{\sigma} \vec{c}_{\sigma}^{\dagger} T \vec{c}_{\sigma}, \quad (3.5)$$

with \vec{c}^{\dagger} a row vector consisting of creation operators $c_{l\sigma}^{\dagger}$, l runs over all the lattice sites of an arbitrary geometry. T is the matrix built up by on-site energies $\{\varepsilon_l\}$ and hopping amplitudes $\{t_{ij}\}$.

Since the bath is non-interacting, the matrix T can be diagonalized by a unitary matrix A :

$$(A^{\dagger} T A)_{kq} = \varepsilon_k \delta_{kq}, \quad (3.6)$$

whose column vectors form components of bases in k -representation, i.e.

$$c_{i\sigma} = \sum_k a_{ik} b_{k\sigma}, \quad c_{i\sigma}^{\dagger} = \sum_k a_{ik}^* b_{k\sigma}^{\dagger}, \quad (3.7)$$

and now H_{bath} is written as

$$H_{\text{bath}} = \sum_{\sigma k} \varepsilon_k b_{k\sigma}^{\dagger} b_{k\sigma} \quad (3.8)$$

For the site $i = 0$, we insert the transformed $c_{0\sigma}^{(\dagger)}$ to the coupling Hamiltonian Eq. (3.4), it gives the hybridization in k -representation with $V_k = V a_{0k}$.

$$H_{\text{imp-bath}} = \sum_{k\sigma} V_k (f_{\sigma}^{\dagger} b_{k\sigma} + b_{k\sigma}^{\dagger} f_{\sigma}). \quad (3.9)$$

The Green's function of the impurity $G(\omega) = \langle\langle f, f^{\dagger} \rangle\rangle_{\omega}$ can be derived by using equation of motion [8]. Details can be found in Ref. [23] and will not be elaborated here. Nevertheless, the form of the one-particle Green's function has a simple and insightful structure:

$$G_{\sigma}(\omega) = \frac{1}{\omega + i\delta - \varepsilon_f - \bar{\Delta}(\omega) - \Sigma^U(\omega)}, \quad (3.10)$$

where $\Sigma^U(\omega)$ is the correlation part of the one-particle self energy, clearly the correlation effect is caused by Coulomb interaction U on the impurity site. $\bar{\Delta}(\omega)$

is a summation over all the bath non-interacting propagators $\frac{1}{\omega - \varepsilon_k}$ with a weight V_k^2 evaluating the hybridization strength.

Usually the imaginary part is referred to as the hybridization function

$$\Delta(\omega) = -\lim_{\delta \rightarrow 0} \text{Im}[\bar{\Delta}(\omega + i\delta)] = \pi \sum_k V_k^2 \delta(\omega - \varepsilon_k), \quad (3.11)$$

the second equality makes use of the Lorentzian formalism of the delta function:

$$\lim_{\delta \rightarrow 0} \frac{\delta}{\pi(A^2 + \delta^2)} = \delta(A). \quad (3.12)$$

From the above form of hybridization one can see that all the information about bath and its coupling to the impurity are encoded in such single frequency dependent function. In other words, the impurity can only “see” the bath from the hybridization function $\Delta(\omega)$, which averages over the non-interacting Green’s function $\frac{1}{\omega - \varepsilon_k}$, hence is seemingly geometry dependent (because ε_k depends on bath geometry). However, we will elaborate that impurity models are essentially bath geometry independent, and is effectively a one-dimensional problem. This property is crucial to the NRG procedure.

As explained, the impurity site only sees the bath (represented by parameter sets $\{\varepsilon_l\}$ and $\{t_{ij}\}$) from its hybridization function $\Delta(\omega)$, it is natural to ask if such statement is reversible, i.e can one determine the bath geometry merely from $\Delta(\omega)$? The answer is negative.

We can look at the SIAM defined with an infinite chain-like bath

$$H_{\text{bath}} = \sum_{\sigma} \sum_{l=0}^{\infty} t_l (c_{l\sigma}^{\dagger} c_{l+1\sigma} + c_{l+1\sigma}^{\dagger} c_{l\sigma}), \quad (3.13)$$

the matrix representing such Hamiltonian is in a tridiagonal form, where forward-hopping is expressed as $c_l^{\dagger} c_{l+1}$, giving the superdiagonal elements, and backward-hopping $c_{l+1}^{\dagger} c_l$ the subdiagonal ones.

The hybridization function $\Delta(\omega)$ is essentially the first diagonal element of the inverse matrix $\{\omega - (H_{\text{bath}} + H_{\text{imp-bath}})\}^{-1}$, as only the $i = 0$ bath site is coupled to the impurity. The inverse matrix follows the form of a general Green’s function, i.e $G = \{\omega - \varepsilon\}^{-1}$. The inverse of such a tridiagonal matrix can be analytically written down by a continued fraction expansion

$$\Delta(\omega) = \frac{V^2}{\omega - \varepsilon_0 - \frac{t_0^2}{\omega - \varepsilon_1 - \frac{t_1^2}{\omega - \varepsilon_2 - \frac{t_2^2}{\omega - \varepsilon_3 - \dots}}}}. \quad (3.14)$$

Let’s assume that $\Delta(\omega)$ is given via a bath on a square lattice. However, with Eq. (3.14) one can always adjust parameter sets $\{\varepsilon_l\}$ and $\{t_{ij}\}$ and equate the LHS with a given $\Delta(\omega)$. This is saying, even if the hybridization is originally determined from a certain geometry (in our case a square lattice), one can always map it onto a semi-infinite chain. For the impurity, dynamics is only affected by

$\Delta(\omega)$, regardless of bath geometry. In this sense, impurity models are said to be effectively one-dimensional problems. The semi-infinite chain can be viewed as the single conduction band that the impurity is coupled to.

For cluster extensions of DMFT, the single-impurity Anderson model can be generalized to an N -impurity model, where N represents the cluster size and corresponds to the number of impurities. Increasing the number of impurity sites enhances the resolution of spatial correlations. In this thesis, a 2-site scheme is employed, with details provided in Section 2.6.

3.3 Logarithmic discretization

In the previous sections, we discussed the prototype model in Kondo physics, namely the SIAM. The Hamiltonian in both the lattice representation Eq. (3.4) and k -representation Eq. (3.9) is well-defined, describing an interacting impurity coupled to a non-interacting bath. However, for practical calculations, the Hamiltonian requires slight modification.

Our starting point for Wilson's NRG approach is to coarse-grain a continuous non-interacting conduction band, which leads to a discretized set of states that can be mapped onto a semi-infinite chain, known as the Wilson chain (as discussed in the previous section, any bath geometry can be mapped to a one-dimensional tight-binding model). The transformed Wilson chain Hamiltonian can then be numerically solved by iterative diagonalization. The remainder of this chapter follows these steps: (1) Discretization of the conduction band, (2) Mapping onto a Wilson chain, and (3) Iterative diagonalization.

The continuous form of SIAM Hamiltonian follows as:

$$\begin{aligned} H_{\text{bath}} &= \sum_{\sigma} \int_{-D}^D d\varepsilon g(\varepsilon) a_{\varepsilon\sigma}^{\dagger} a_{\varepsilon\sigma}, \\ H_{\text{imp-bath}} &= \sum_{\sigma} \int_{-D}^D d\varepsilon h(\varepsilon) (f_{\sigma}^{\dagger} a_{\varepsilon\sigma} + a_{\varepsilon\sigma}^{\dagger} f_{\sigma}), \end{aligned} \quad (3.15)$$

where D is the band width. From this, we see that the conduction band is now assumed to be continuous and is described by a spectrum $g(\varepsilon)$ and the hybridization function $h(\varepsilon)$. The annihilation (creation) operators $a_{\varepsilon\sigma}^{(\dagger)}$ satisfy the fermionic anticommutation relations: $\{a_{\varepsilon\sigma}^{\dagger}, a'_{\varepsilon'\sigma'}\} = \delta(\varepsilon - \varepsilon')\delta_{\sigma\sigma'}$.

We refer to the above continuous Hamiltonian as the integral representation, to distinguish it from the r - and k - representations mentioned earlier. This integral representation provides a convenient starting point for the so-called logarithmic discretization, which occurs in the frequency (or energy) domain. The parameter $\Lambda > 1$ defines a series of intervals separated by discrete points.

$$x_n = \pm\Lambda^{-n}, n = 0, 1, 2, \dots \quad (3.16)$$

The width of the intervals decreases exponentially with the labeling n

$$d_n = \Lambda^{-n} - \Lambda^{-(n+1)}. \quad (3.17)$$

Within each interval, one can introduce an orthonormal basis set

$$\psi_{np}^{\pm}(\varepsilon) = \frac{1}{\sqrt{d_n}} e^{\pm ip\omega_n \varepsilon}, \quad \text{for } x_{n+1} < \pm\varepsilon < x_n \quad (3.18)$$

The index p labels the complete basis and runs over $[-\infty, \infty]$. Alike a wave-vector in reciprocal space, the frequencies are defined by $\omega_n = 2\pi/d_n$. Given such basis defined within each interval, one can expand the annihilation operator

$$a_{\varepsilon\sigma} = \sum_{np} [a_{np\sigma} \psi_{np}^+(\varepsilon) + b_{np\sigma} \psi_{np}^-(\varepsilon)] \quad (3.19)$$

The above expansion is essentially a Fourier expansion in each interval. The component operators $a_{np\sigma}^{(\dagger)}$, $b_{np\sigma}^{(\dagger)}$ and $a_{np\sigma}^{(\dagger)}$ fulfill the fermionic commutation relation as well.

Given the transformation, the Hamiltonian Eq. (3.15) can be expressed with these discrete operators. We discuss the $H_{\text{imp-bath}}$ and H_{bath} separately.

According to Eq. (3.15), The hybridization part is

$$\int_{-D}^D d\varepsilon h(\varepsilon) f_{\sigma}^{\dagger} a_{\varepsilon\sigma} = f_{\sigma}^{\dagger} \sum_{np} [a_{np\sigma} \int^{+n} d\varepsilon h(\varepsilon) \psi_{np}^+(\varepsilon) + b_{np\sigma} \int^{-n} d\varepsilon h(\varepsilon) \psi_{np}^-(\varepsilon)], \quad (3.20)$$

where a short-cut is defined

$$\int^{+n} d\varepsilon \equiv \int_{x_{n+1}}^{x_n} d\varepsilon, \quad \int^{-n} d\varepsilon \equiv \int_{-x_n}^{-x_{n+1}} d\varepsilon. \quad (3.21)$$

For a constant hybridization $h(\varepsilon) = h$, the above integral filters out the $p = 0$ component only

$$\int^{\pm n} d\varepsilon h \psi_{np}^{\pm}(\varepsilon) = h \sqrt{d_n} \delta_{p0}. \quad (3.22)$$

Equivalently, the impurity only couples to the conduction band through the $p = 0$ mode. This result does not lead to any additional approximations even for non-constant hybridization $h(\varepsilon)$.

Now we let $h(\varepsilon)$ within each interval take the corresponding constant and denote

$$h(\varepsilon) = h_n^{\pm}, \quad x_{n+1} < \pm\varepsilon < x_n, \quad (3.23)$$

the constants are given by the average of the hybridization function $\Delta(\omega)$ with respect to each interval

$$(h_n^{\pm})^2 = \frac{1}{d_n} \int^{\pm n} d\varepsilon \frac{1}{\pi} \Delta(\varepsilon), \quad (3.24)$$

which eventually leads to the following form

$$\int_{-1}^1 d\varepsilon h(\varepsilon) f_{\sigma}^{\dagger} a_{\varepsilon\sigma} = \frac{1}{\sqrt{\pi}} f_{\sigma}^{\dagger} \sum_n [\gamma_n^+ a_{n0\sigma} + \gamma_n^- b_{n0\sigma}], \quad (3.25)$$

with $(\gamma_n^+)^2 = \int^{\pm n} d\varepsilon \Delta(\varepsilon)$. Such form remains the property discussed before: the impurity (f_σ^\dagger) only couples to the $p = 0$ mode ($a_{n0\sigma}, b_{n0\sigma}$) through the averaged hybridization $(\gamma_n^+)^2$.

The derivation of H_{bath} in the discrete basis follows similar process and is discussed in Ref. [22], here we directly give the final result. One can expect a diagonal form in H_{bath}

$$\begin{aligned} H_{\text{discrete}} &= H_{\text{imp}} + H_{\text{bath}} + H_{\text{imp-bath}} \\ &= H_{\text{imp}} + \sum_{n\sigma} [\xi_n^+ a_{n\sigma}^\dagger a_{n\sigma} + \xi_n^- b_{n\sigma}^\dagger b_{n\sigma}] \\ &\quad + \frac{1}{\sqrt{\pi}} \sum_{\sigma} f_{\sigma}^\dagger \left[\sum_n (\gamma_n^+ a_{n\sigma} + \gamma_n^- b_{n\sigma}) \right] + \frac{1}{\sqrt{\pi}} \sum_{\sigma} \left[\sum_n (\gamma_n^+ a_{n\sigma}^\dagger + \gamma_n^- b_{n\sigma}^\dagger) \right] f_{\sigma}, \end{aligned} \quad (3.26)$$

where the energy of conduction band electron is

$$\xi_n^\pm = \frac{\int^{\pm n} d\varepsilon \Delta(\varepsilon) \varepsilon}{\int^{\pm n} d\varepsilon \Delta(\varepsilon)} = \pm \frac{1}{2} \Lambda^{-n} (1 + \Lambda^{-1}). \quad (3.27)$$

In the Hamiltonian Eq. (3.26), we have relabeled the operator $a_{n0\sigma} \equiv a_{n\sigma}$ and dropped the $p \neq 0$ mode in H_{bath} , which is strict for $H_{\text{imp-bath}}$ but considered a reasonable approximation for H_{bath} because of the prefactor $(1 - \Lambda^{-1})$.

3.4 Mapping onto a Wilson chain

At this point, We have obtained the discretized Hamiltonian Eq. (3.26), as said in section 3.3, the next step is to map it onto a semi-infinite chain. According to the discussion in section 3.2, any geometry of the bath can be in principle reduced to a linear chain, and we have already introduced the H_{bath} of the chain geometry in Eq. (3.13). In this section, the goal is to transform Eq. (3.26) to the exactly same structure as Eq. (3.13). Note that the later one is derived from the original model with the same hybridization $\Delta(\omega)$, whereas the transformed form discussed in this section is derived from an approximate H_{discrete} , which dropped off $p \neq 0$ mode, and such approximation is the starting point of NRG. In the semi-infinite chain representation, the impurity is only coupled to the first bath site with fermionic operators $c_{0\sigma}^{(\dagger)}$. If we look at the Eq. (3.26), the $H_{\text{imp-bath}}$ directly corresponds to such coupling, and $c_{0\sigma}$ can be read off. We define

$$c_{0\sigma} = \frac{1}{\sqrt{\xi_0}} \sum_n (\gamma_n^+ a_{n\sigma} + \gamma_n^- b_{n\sigma}), \quad (3.28)$$

with the normalization

$$\xi_0 = \sum_n [(\gamma_n^+)^2 + (\gamma_n^-)^2] = \int_{-1}^1 d\varepsilon \Delta(\varepsilon). \quad (3.29)$$

With such definition, the hybridization (Hermitian conjugate ignored) is rewritten as

$$\frac{1}{\sqrt{\pi}} f_{\sigma}^\dagger \sum_n (\gamma_n^+ a_{n\sigma} + \gamma_n^- b_{n\sigma}) = \sqrt{\frac{\xi_0}{\pi}} f_{\sigma}^\dagger c_{0\sigma} \quad (3.30)$$

Now we have rewritten the coupling term $H_{\text{imp-bath}}$. The H_{bath} shown in Eq. (3.26) expressed in $a_{n\sigma}^{(\dagger)}$ and $b_{n\sigma}^{(\dagger)}$ is supposed to be transformed to a nearest neighbor hopping form as shown in Eq. (3.13). Here below we firstly give the final result

$$\begin{aligned} H_{\text{Wilson}} &= H_{\text{imp}} + H_{\text{imp-bath}} + H_{\text{bath}}, \\ &= H_{\text{imp}} + \sqrt{\frac{\xi_0}{\pi}} \sum_{\sigma} [f_{\sigma}^{\dagger} c_{0\sigma} + c_{0\sigma}^{\dagger} f_{\sigma}] + \sum_{\sigma, n=0}^{\infty} [\varepsilon_n c_{n\sigma}^{\dagger} c_{n\sigma} + t_n (c_{n\sigma}^{\dagger} c_{n+1\sigma} + c_{n+1\sigma}^{\dagger} c_{n\sigma})], \end{aligned} \quad (3.31)$$

where $c_n^{(\dagger)}$ corresponds to the n -th chain site. As $c_{0\sigma}^{(\dagger)}$ is not orthogonal to $a_{n\sigma}^{(\dagger)}$ and $b_{n\sigma}^{(\dagger)}$, to realize the above transformation, a standard Gram-Schmidt procedure is implemented, which is equivalent to an orthogonal transformation

$$c_{n\sigma} = \sum_{m=0}^{\infty} [u_{nm} a_{m\sigma} + v_{nm} b_{m\sigma}], \quad (3.32)$$

the matrix coefficients u_{nm} , v_{nm} are determined by a series of recursion relations, details can be found in Ref. [24].

Not surprisingly, the initial parameters can be numerically evaluated through integrals of hybridization $\Delta(\omega)$ and others can be fixed recursively. For some special form of hybridization, the parameters can be derived analytically. We are especially interested in the $\{\varepsilon_n\}$ and $\{t_n\}$, because they eventually define the chain Hamiltonian. For a constant and even hybridization $\Delta(\omega) = [-1, 1]$, Wilson derived a formula for $\{t_n\}$

$$t_n = \frac{(1 + \Lambda^{-1})(1 - \Lambda^{-n-1})}{2\sqrt{1 - \Lambda^{-2n-1}}\sqrt{1 - \Lambda^{-2n-3}}} \Lambda^{-n/2}, \quad \lim_{n \rightarrow \infty} t_n = \frac{1}{2}(1 + \Lambda^{-1})\Lambda^{-n/2}. \quad (3.33)$$

$\varepsilon_n = 0$ for an even hybridization. The exponentially decaying nature of t_n arises from the logarithmic discretization and is essential for the method to work.

This decaying behavior of t_n also has an intuitive interpretation. While the operator $c_{0\sigma}^{\dagger}$ creates an electron at the impurity site and couples to it with an amplitude of $\sqrt{\frac{\xi_0}{\pi}}$, the wavefunction of such a state is peaked at the impurity. On the other hand, the operators $c_{n\sigma}^{\dagger}$ create electrons at the n -th chain site, and their wavefunctions form a sequence of shells centered around the impurity. The hopping amplitudes decay, and the radius of the wavefunctions grows exponentially, as illustrated in Fig. 7.

In principle, the summation in the Wilson chain Eq. (3.31) runs to infinity, but the Hilbert space size grows explosively with the chain length L (dimension $\propto 2^L$). This many-body problem can be approximately solved by iterative diagonalization, as discussed in the following section.

3.5 Iterative diagonalization

The Wilson chain Hamiltonian derived so far provides the prerequisite of the iterative renormalization group (RG) procedure, as the form of H_{Wilson} can be easily recast into a renormalization transformation as shown below.

Firstly we view H_{Wilson} as a limit of a sequence of Hamiltonian H_N , when the labeling parameter N approaches infinity

$$H_{Wilson} = \lim_{N \rightarrow \infty} \Lambda^{-(N-1)/2} H_N, \quad (3.34)$$

with

$$\begin{aligned} H_N = & \Lambda^{(N-1)/2} \left\{ H_{\text{imp}} + \sqrt{\frac{\xi_0}{\pi}} \sum_{\sigma} (f_{\sigma}^{\dagger} c_{0\sigma} + c_{0\sigma}^{\dagger} f_{\sigma}) \right. \\ & \left. + \sum_{\sigma, n=0}^N \varepsilon_n c_{n\sigma}^{\dagger} c_{n\sigma} + \sum_{\sigma, n=0}^{N-1} t_n (c_{n\sigma}^{\dagger} c_{n+1\sigma} + c_{n+1\sigma}^{\dagger} c_{n\sigma}) \right\}. \end{aligned} \quad (3.35)$$

Note that the prefactors in Eq. (3.34) and Eq. (3.35) cancel each other and are chosen to eliminate the N -dependence of t_{N-1} , namely the hopping amplitude between the last two sites, because when $n = N$ is large, t_n has the form $t_n \propto \Lambda^{-n/2}$ as seen in Eq. (3.33). The choice of such factor is model-dependent, in our case the uniform hybridization is assumed.

H_N owns a successive relation

$$H_{N+1} = \sqrt{\Lambda} H_N + \Lambda^{N/2} \left\{ \sum_{\sigma} \varepsilon_{N+1} c_{N+1\sigma}^{\dagger} c_{N+1\sigma} + \sum_{\sigma} t_N (c_{N\sigma}^{\dagger} c_{N+1\sigma} + c_{N+1\sigma}^{\dagger} c_{N\sigma}) \right\}, \quad (3.36)$$

combined with Eq. (3.34), such recursion relation tells a straightforward but insightful fact: H can be constructed by addition of new sites to a starting configuration H_0 , which is given by

$$H_0 = \Lambda^{-1/2} \left\{ H_{\text{imp}} + \sum_{\sigma} \varepsilon_0 c_{0\sigma}^{\dagger} c_{0\sigma} + \sqrt{\frac{\xi_0}{\pi}} \sum_{\sigma} (f_{\sigma}^{\dagger} c_{0\sigma} + c_{0\sigma}^{\dagger} f_{\sigma}) \right\}. \quad (3.37)$$

The Hamiltonian corresponds to a 2-site cluster containing the impurity ($H_{\text{imp}}, f_{\sigma}^{(\dagger)}$) and the first conduction electron ($c_{0\sigma}^{(\dagger)}$).

Now the recursion Eq. (3.36) can be regarded as a renormalization transformation R

$$H_{N+1} = R(H_N) \quad (3.38)$$

At this point, it is natural to apply iterative diagonalization to H_{Wilson} due to its recursive formalism. Firstly we diagonalize H_0 and obtain a set of eigenstates and eigenenergies $\{E_0(r), |r\rangle_0\}$, with which one can construct a basis for the next Hamiltonian H_1 and diagonalize again ..., eventually the complete Hamiltonian can be diagonalized in such procedure. Assume we have obtained the spectrum $\{E_N(r), |r\rangle_N\}$ of the N -th Hamiltonian H_N ,

$$H_N |r\rangle_N = E_N(r) |r\rangle_N, \quad r = 1, 2, \dots, N_s \text{ (dimension of } H_N), \quad (3.39)$$

the general strategy follows:

- (a) Diagonalize H_N and obtain the eigenstates and eigenenergies, as denoted above

(b) Rescale the eigenenergies $\{E_N(r)\}$ by $\sqrt{\Lambda}$, as defined in Eq. (3.36)

(c) Construct a basis for H_{N+1}

$$|r; s\rangle_{N+1} = |r\rangle_N \otimes |s\rangle_{N+1} \quad (3.40)$$

the state $|r; s\rangle_{N+1}$ are product states made of the eigenstates obtained in (a) and an appropriate basis for the added site $|s\rangle_{N+1}$. From the above new basis, one can construct the matrix representation for the Hamiltonian H_{N+1}

$$H_{N+1}(rs, r's') = {}_{N+1} \langle r; s | H_{N+1} | r' s' \rangle_{N+1} \quad (3.41)$$

diagonalizing H_{N+1} gives the new eigenenergies $\{E_{N+1}(w)\}$ and lifts the degeneracy of $\{E_N(r)\}$, as the dimension of the Hilbert space multiplies by a factor d_{local} , which is the dimension of the added site. The new eigenstates $\{|w\rangle_{N+1}\}$ can be related to the basis $\{|r; s\rangle_{N+1}\}$ via the unitary transformation

$$|w\rangle_{N+1} = \sum_{rs} A_{rw}^s |r; s\rangle_{N+1} \quad (3.42)$$

where w labels the eigenstates in expanded basis, r runs over old basis, and s labels the basis of the added site $|s\rangle_{N+1}$. Apparently, the d_{local} matrices are

$$A_{rw}^s = {}_{N+1} \langle r; s | w \rangle_{N+1} \quad (3.43)$$

Such special formulation of the unitary transformation forms the so-called matrix product states (MPS), which is widely used and investigated in correlated systems.

Additionally, the ground state energy is negative, setting to zero is convenient for the next steps.

(d) Truncate the spectrum $\{E_{N+1}(w)\}$. As explained before, the dimension of the Hilbert space grows exponentially when adding new sites to H_N . A rather straightforward truncation scheme is used in iterative diagonalization: we only remain N_{keep} eigenstates, in other words, the dimension of the Hilbert space is fixed to N_{keep} . Therefore, the computation time only increases linearly with the chain length.

The last step, truncation, plays a crucial role in NRG. It ensures the feasibility of numerical computation and strongly affects the effectiveness of the method. The key question is: to what extent does the loss of high-energy states affect the remaining low-energy states? The answer lies in the very first step of the entire NRG procedure, namely logarithmic discretization.

On one hand, the exponentially decaying nature of $t_n \propto \Lambda^{-n/2}$ arises from logarithmic discretization (note that for any general form of hybridization $\Delta(\omega)$, t_n decays exponentially, not just for uniform hybridization). This form of t_n directly leads to the recursion relation Eq. (3.36), where the added site can be regarded as a perturbation with strength $\Lambda^{-1/2}$. On the other hand, the parameter $\Lambda > 1$ controls the spacing of the grid; a larger Λ leads to a finer grid

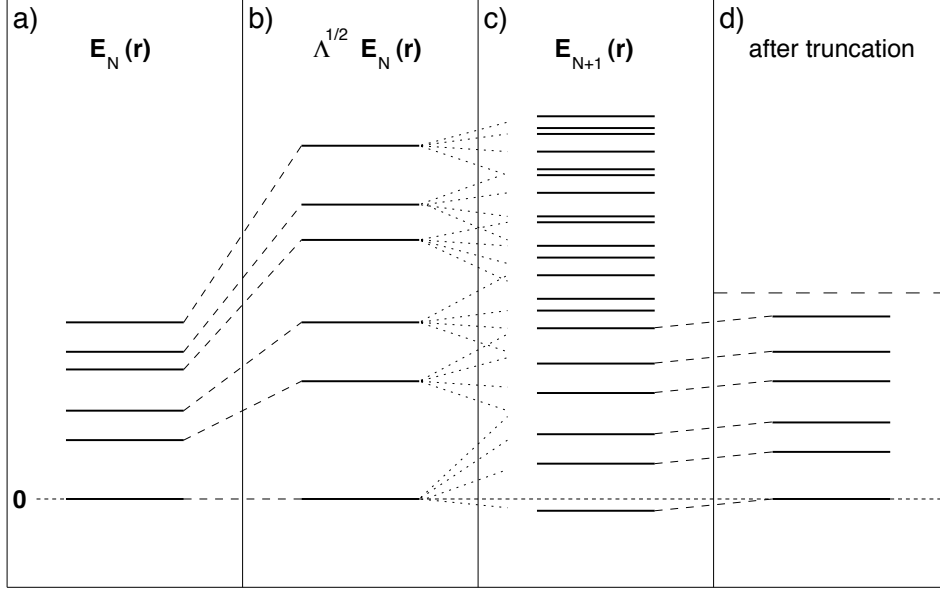


Figure 8: The procedure diagram illustrates the step-by-step process of iterative diagonalization as employed in the Numerical Renormalization Group (NRG) method, the figure is adapted from Ref. [23].

near zero, which in turn gives rise to weaker perturbation from added sites and higher resolution at low frequencies.

The close connection between logarithmic discretization and the success of the truncation scheme (fixed N_{keep}) is one of the most important features of NRG. This explains and justifies the first two steps—discretization and mapping onto a semi-infinite chain.

From NRG spectrum to physical quantities

Given the spectrum $\{E_n, |n\rangle\}$ from an NRG run, important physical quantities such as Green's function, spectral function and self-energy can be evaluated. The Lehmann representation of Green's function reads

$$G_{\text{imp}}^R(\omega) = \frac{1}{Z} \sum_{mn} \frac{e^{-\beta E_m} + e^{-\beta E_n}}{\omega + E_m - E_n + i0^+} \langle m|c|n\rangle \langle n|c^\dagger|m\rangle, \quad (3.44)$$

from which spectral function can be calculated by taking the imaginary part

$$A_{\text{imp}}(\omega) = -\frac{1}{\pi} \text{Im} G_{\text{imp}}^R(\omega) = \sum_{mn} \delta(\omega + E_m - E_n) \frac{e^{-\beta E_m} + e^{-\beta E_n}}{Z} |\langle m|c|n\rangle|^2. \quad (3.45)$$

The second equal sign made use of the Dirac relation $\frac{1}{\omega+i0^+} = \frac{\mathcal{P}}{\omega} - i\pi\delta(\omega)$.

The self-energy is given by the Dyson's equation

$$\Sigma(\omega) = G_0^{-1}(\omega) - G_{\text{imp}}^{-1}(\omega), \quad (3.46)$$

where $G_0^{-1}(\omega)$ is the non-interacting Green's function that only incorporates hybridization.

In practical numerical calculations, several useful techniques have been developed, such as the full density matrix (fdmNRG), which constructs a complete set of approximate eigenstates of the full Hamiltonian from the discarded states [25].

The resolution of dynamical correlation functions, such as $A(\omega)$, at finite frequencies can be improved using an adaptive broadening scheme [26] applied to the discrete data obtained from NRG calculations. By examining the sensitivity of the discrete data to z -shifts, we can assess whether certain features are physical or merely numerical artifacts.

3.6 Renormalization group flow

The Wilson chain Hamiltonian, as described in Eq. (3.38), can be expressed recursively, with each pair of neighboring terms H_N and H_{N+1} connected through an RG transformation. Consequently, the iterative diagonalization process can be interpreted as a sequence of RG transformations.

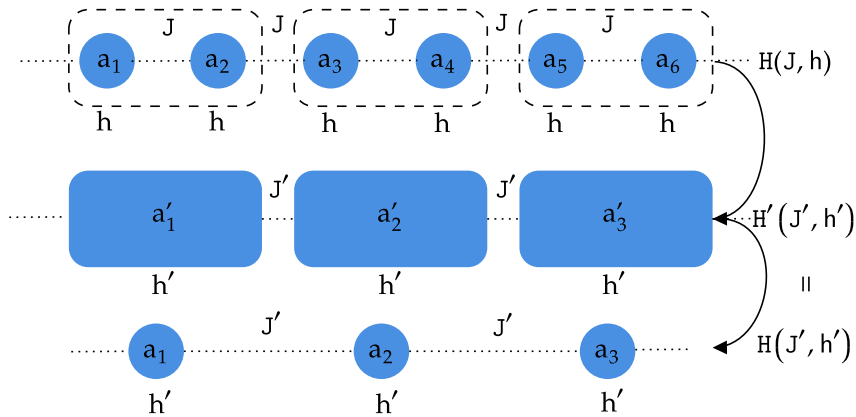


Figure 9: A heuristic introduction to the concept of renormalization. A chain model described by $H(J, h)$ is coarse-grained into an effective model described by $H'(J', h')$. If the rescaled effective model is equivalent to the original one, the implemented operation is regarded as a renormalization group transformation.

The basic RG concepts can be understood in a heuristic way [27]. We consider a one-dimensional lattice defined with annihilation (creation) operators $a_i^{(\dagger)}$ and parameters $\{J, h\}$, as shown in Fig. 9. The Hamiltonian is formally $H(J, h)$. Combining every neighboring two sites and defining a series of new operators $a_i^{(\dagger) \prime}$ in each dimer block give a Hamiltonian describing the effective model $H' = H(J', h')$. We have assumed that such operation does not change the form of Hamiltonian H , but only leads to renormalized parameters $\{J', h'\}$. Finally we rescale it back to the original lattice spacing. The mapping from H to H' is

known as a renormalization group (RG) transformation.

$$H(J', h') = R\{H(J, h)\}. \quad (3.47)$$

If the parameters are denoted as a vector in parameter space $\mathbf{K} = (J, h)$, then the RG transformation reads

$$\mathbf{K}' = R(\mathbf{K}), \quad (3.48)$$

it is essentially an operation that moves the vector from \mathbf{K} to \mathbf{K}' . A sequence of RG transformation naturally leads to a trajectory in parameter space. If we trace and plot (in principle) all the trajectory residing in parameter space, such diagram is called flow diagram. The special points that satisfy the condition

$$\mathbf{K}^* = R(\mathbf{K}^*) \quad (3.49)$$

are referred to as fixed points.

However, the RG transformation in NRG Eq. (3.38) does not remain the original form before transformation, as the Wilson chain is extended by an additional site, even if it is rescaled as well. Nevertheless analysis of the energy flow $E_N(r)$ as a function of Wilson chain length N can give important physical properties of the system.

Take the SIAM as an example, two fixed points of the rescaled energy flow can be observed, see Fig. 10. They divide the energy scale $\Lambda^{-N/2}$ into three regime. Each of them corresponds to a different physical phase or behavior of the impurity as a function of the energy scale.

1. Free orbital regime: in this regime, the impurity behaves as if it were free, meaning it is weakly coupled to the conduction band and behaves almost like a non-interacting system. The impurity electron moves as a free particle, and its interaction with the bath (conduction electrons) is not yet significant.
2. Local moment regime: it arises at intermediate energy scales when the impurity begins to behave like a localized magnetic moment. In this regime, the interaction between the impurity and the conduction electrons has become important enough to freeze out charge fluctuations, but spin fluctuations are still prominent. The impurity develops a well-defined local spin or magnetic moment.
3. Strong coupling regime: it emerges at low energies when the impurity has become strongly coupled to the conduction electrons. This regime is characterized by the formation of a Kondo singlet or a similar strongly correlated state, where the conduction electrons effectively "screen" the impurity's magnetic moment.

For the single-band $t - t'$ Hubbard model and three-band Emery model, a strong coupling (Fermi liquid) fixed point is reached in the low energy regime, as shown in our results in chapter 5 and 6.

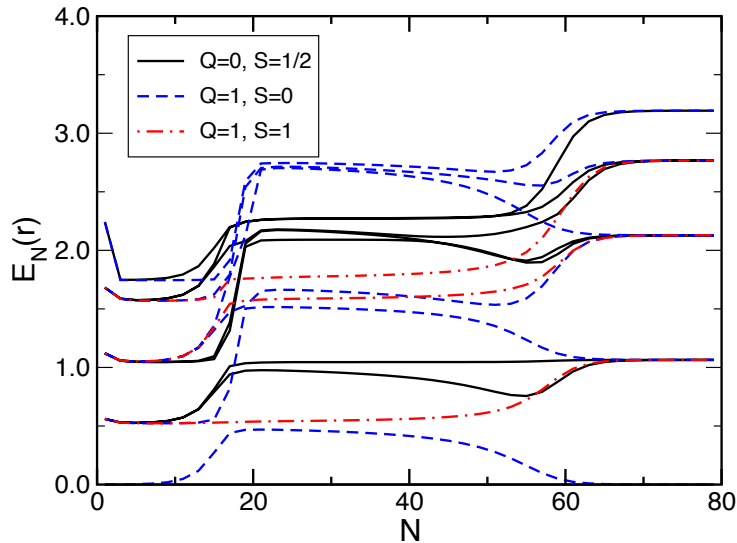


Figure 10: Energy flow of SIAM. $\varepsilon_f = -0.5 \times 10^{-3}$, $U = 10^{-3}$, $V = 0.004$, $\Lambda = 2.5$. Two fix points at $N = 20$ and $N = 60$ partition the flows into three screening regimes, i.e. free orbital, local moment, and strong coupling regime. The figure is adapted from Ref. [23]

4 Model Study

4.1 Fermi liquid theory

This thesis aims to determine the quantum phase transition between the pseudogap and Fermi liquid phases. This section follows the textbook written by Wolfgang Nolting [28] and introduce the basic concepts of Fermi liquid.

The familiar concept of the Fermi sphere, and thus the Fermi surface in momentum space, is successfully developed to describe metals, based on a strong yet effective approximation, e.g. the non-interacting Fermi gas model. The spectral function is simply a Dirac delta function

$$A_{\mathbf{k}}^{(0)}(\omega) = \delta(\omega + \mu_0 - \varepsilon_{\mathbf{k}}). \quad (4.1)$$

The occupation number can be evaluated with spectral theorem

$$\langle n_{\mathbf{k}} \rangle^{(0)} = \frac{1}{\exp(\beta(\varepsilon_{\mathbf{k}} - \mu_0)) + 1} \stackrel{T \rightarrow 0}{=} \Theta(\varepsilon_F - \varepsilon_{\mathbf{k}}), \quad (4.2)$$

which at $T = 0$ becomes a step function owning a discontinuity in both momentum and energy space. The corresponding momentum and energy are defined as Fermi wavevector \mathbf{k}_F and energy $\varepsilon_F = \mu_0(T = 0)$. The so-called Fermi surface can be defined without any ambiguity

$$\text{Fermi surface} \equiv \{\mathbf{k} : \varepsilon_{\mathbf{k}} \stackrel{!}{=} \mu_0(T = 0) = \varepsilon_F\}, \quad (4.3)$$

namely the equal-energy surface with respect to Fermi energy. A natural question is: what if the interaction between electrons is switched on?

For weak interaction, it is tempting to expect:

- A one-to-one relation between interacting system and non-interacting Fermi gas: $E_{\mathbf{k}} \leftrightarrow \varepsilon_{\mathbf{k}}$. $E_{\mathbf{k}}$ is the energy spectrum of interacting system.
- The delta peaks in spectral function $A_{\mathbf{k}}^{(0)}(\omega)$ are broadened out with a finite width.
- The occupation number $\langle n_{\mathbf{k}} \rangle^{(0)}$ will be softened or deformed, just as at finite temperature.

For strongly interacting systems, as described in the third assumption, a well-defined Fermi surface, e.g. the discontinuity between occupied and unoccupied states are expected to be lost, because scattering induced by interaction moves electrons from low energy regime to higher energy. However it is the other way around, in many cases a clear Fermi surface can still be observed in experiments. Such a system that takes into account interaction but behaves like non-interacting Fermi gas is referred to as Fermi liquid.

We focus on near zero temperature and investigate this property further. The occupation number is now written as

$$\langle n_{\mathbf{k}} \rangle_{T \rightarrow 0} = -\frac{1}{\pi} \int_{-\infty}^0 d\omega \operatorname{Im} \frac{1}{\omega + \mu - \varepsilon_{\mathbf{k}} - \Sigma_{\mathbf{k}}(\omega)}. \quad (4.4)$$

The discontinuity only occurs when the integrand has singularity, therefore the imaginary part of self-energy vanishes at some points.

$$\Sigma_{\mathbf{k}}(\omega) = \operatorname{Re}\Sigma_{\mathbf{k}}(\omega) + i\operatorname{Im}\Sigma_{\mathbf{k}}(\omega), \quad (4.5a)$$

$$\Sigma_{\mathbf{k}}(\omega) \approx \alpha_{\mathbf{k}} + \beta_{\mathbf{k}}\omega + i\gamma_{\mathbf{k}}\omega^2. \quad (4.5b)$$

Eq. (4.5b) is from a low energy expansion based upon perturbation theory, it agrees with the assumption of a vanishing imaginary part in Fermi liquid. Inserting Eq. (4.5a) into the general relation between $A_{\mathbf{k}}(\omega)$ and $\Sigma_{\mathbf{k}}(\omega)$:

$$A_{\mathbf{k}}(\omega) = -\frac{1}{\pi} \frac{\operatorname{Im}\Sigma_{\mathbf{k}}(\omega)}{\{\omega + \mu - \varepsilon_{\mathbf{k}} - \operatorname{Re}\Sigma_{\mathbf{k}}(\omega)\}^2 + \{\operatorname{Im}\Sigma_{\mathbf{k}}(\omega)\}^2}. \quad (4.6)$$

Since imaginary part is vanishing, precisely one resonance is required by Fermi liquid

$$\omega + \mu \equiv E_{\mathbf{k}} \stackrel{!}{=} \varepsilon_{\mathbf{k}} + \operatorname{Re}\Sigma_{\mathbf{k}}(E_{\mathbf{k}} - \mu), \quad (4.7)$$

hence the real part of self-energy can be interpreted as a kind of modification of non-interacting dispersion $\varepsilon_{\mathbf{k}}$. In analogy of Eq. (4.3), the Fermi surface in interacting system can be defined as

$$\text{Fermi surface} \equiv \{\mathbf{k} : E_{\mathbf{k}} \stackrel{!}{=} \mu\}. \quad (4.8)$$

As $E_{\mathbf{k}} - \mu$ is a small quantity if \mathbf{k} is not far away from \mathbf{k}_F , the real part of self-energy $\operatorname{Re}\Sigma_{\mathbf{k}}(E_{\mathbf{k}} - \mu)$ can be Taylor-expanded, details can be found in Ref. [28].

Making use of the quasiparticle equation Eq. (4.7) and self-energy expansion, we can define the quasi-particle weight

$$Z_{\mathbf{k}} \equiv \left(1 - \frac{\partial \text{Re}\Sigma_{\mathbf{k}}(\omega)}{\partial \omega} \Big|_{\omega=0} \right)^{-1}, \quad (4.9)$$

which measures how the quasiparticle energy deviates from the non-interacting case. $Z_{\mathbf{k}}$ ranges from 0 to 1, and can be regarded as a renormalization factor, smaller $Z_{\mathbf{k}}$ gives rise to a larger renormalized mass

$$\frac{m}{m^*} = Z_{\mathbf{k}}. \quad (4.10)$$

The quasiparticle lifetime can be defined as

$$\tau_{\mathbf{k}}^{-1} = -Z_{\mathbf{k}} \text{Im}\Sigma_{\mathbf{k}}(\omega), \quad (4.11)$$

which is determined by both real and imaginary part of self-energy. $-\text{Im}\Sigma_{\mathbf{k}}(\omega)$ is proportional to the width of the quasi-particle peak in spectral function $A_{\mathbf{k}}(\omega)$, see Eq. (4.6). When $\mathbf{k} \rightarrow \mathbf{k}_F$, the vanishing imaginary part leads to an infinite life-time. Now we can summarize the basic properties of Fermi liquid

- The existence of a well-defined Fermi surface.
- A unique one-to-one relation to the non-interacting Fermi gas, i.e. well-defined quasiparticles.
- Imaginary part of self-energy increases quadratically with increasing distance from Fermi level, i.e. $\text{Im}\Sigma_{\mathbf{k}}(\omega) \sim \omega^2$.

The validity of Fermi liquid theory holds only when

- ω is close to ε_F , i.e. small excitation.
- Low temperature $T \rightarrow 0$.

In this thesis, a good resolution of low energy spectrum at low temperature is guaranteed by the power of NRG, whose logarithmic nature of frequency grid allows one to investigate, in principle, infinitely low energy properties.

4.2 Pseudogap

In the Brinkman-Rice description [29], the doped metallic state is a Fermi liquid, in which quasiparticles are formed with a weight $Z \propto x$. Single-site DMFT can describe such a system well when spatial correlations are weak and orbital fluctuations are strong enough [5].

Additionally, regardless of the momentum direction or position on the Fermi surface, the onset of coherence (where quasiparticles behave as well-defined entities) happens at a single, uniform energy scale across the entire Fermi surface, as shown in the lower right corner of Fig. 11. In underdoped cuprates, however,

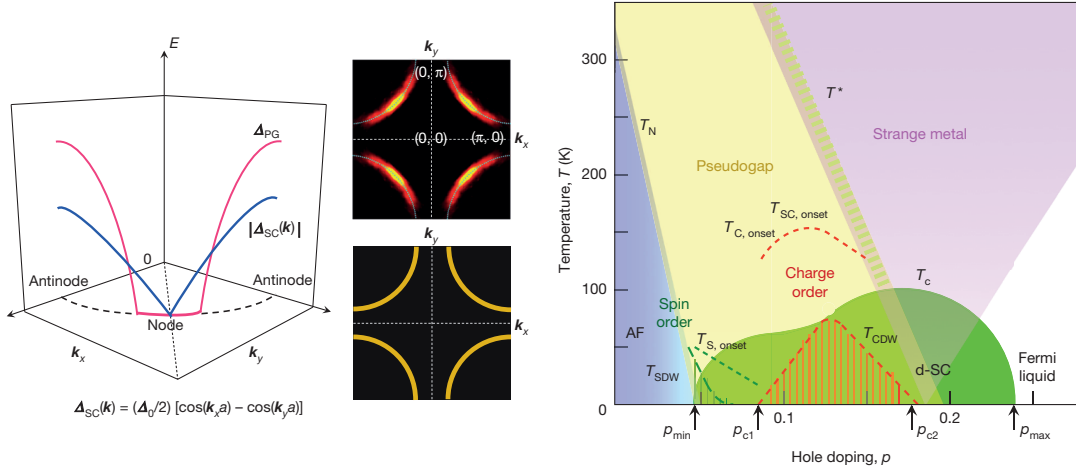


Figure 11: **Left panel:** Gap functions, Fermi arc and large Fermi surface. Once the pseudogap sets in, the antinodal regions, i.e. $(\pi, 0)$ and $(0, \pi)$ of the Fermi surface are gapped out. **Right panel:** Phase diagram, temperature versus hole doping level for the copper oxides. Different color regions indicate where various phases occur. Figures are adapted from Ref. [30]

experiments show that this coherence scale varies across different parts of the Fermi surface [2, 31]. For instance, coherence often forms with different energy cost near the nodal, i.e. $(\frac{\pi}{2}, \frac{\pi}{2})$ (gap-minimal) versus antinodal, i.e. $(0, \pi)$ or $(\pi, 0)$ (gap-maximal) regions, suggesting an anisotropic behavior along the Fermi surface. This anisotropy contrasts with predictions from simple mean-field or single-site DMFT approaches, which lack the momentum dependence needed to capture these experimental observations.

Experiments show that coherent quasiparticle excitations are strongly suppressed in antinodal region. Such suppression leads to a partial energy gap referred to as pseudogap at the Fermi level. However coherent quasi-particles are preserved in nodal region.

The formation of Fermi arc observed in angular resolved photoemission spectroscopy (ARPES) signifies the momentum selective property, it is defined as the arc-shaped region centered at nodal direction, where the spectral function has significant weight for low excitation energy near the Fermi level. In contrast, the antinodal region is gapped out, and has much reduced spectral function value, see the upper right corner of figure 11.

From a real-space perspective, only certain electrons experience this gap. The gap is associated with an insulating state, that only exists for electrons traveling parallel to the Cu – O bonds, whereas those traveling along $(\frac{\pi}{2}, \frac{\pi}{2})$ (at 45 degrees to the Cu – O bond) can move freely throughout the crystal.

Consequently, the nodal/antinodal dichotomy in momentum space is crucial for the description of phenomena observed in cuprates. In this sense, single-site DMFT is no longer adequate to describe the pseudogap state. A short-

range correlation is supposed to be taken into account, because at intermediate and strong coupling, correlation length is expected to be short. In this thesis, the minimal cluster, i.e. a dimer is rationalized by 2-site DCA to study such dichotomy behavior.

This thesis aims to investigate the phase transition between the pseudogap state and the Fermi liquid state at zero temperature by introducing hole doping into a Mott (or charge-transfer) insulator. The overall cuprate phase diagram is shown in the right panel of Fig. 11, a quantum critical point is expected to be found nearby p_{c2} (the critical point for superconductivity and charge order). Below such critical point the system exhibits pseudogap feature, otherwise can be described by Fermi liquid theory.

4.3 Realization of 2-site DCA

To investigate the nodal-antinodal dichotomy, a cluster extension of DMFT is essential. Following the methodology outlined in Ref. [5], we employ a minimal cluster approach and begin with the single-band $t - t'$ Hubbard model

$$H = \sum_{\mathbf{k}, \sigma=\uparrow, \downarrow} \varepsilon_{\mathbf{k}} c_{\mathbf{k}, \sigma}^{\dagger} c_{\mathbf{k}, \sigma} + U \sum_i n_{i\downarrow} n_{i\uparrow}, \quad (4.12a)$$

$$\varepsilon_{\mathbf{k}} = -2t[\cos(k_x) + \cos(k_y)] - 4t' \cos(k_x) \cos(k_y) - \mu. \quad (4.12b)$$

The Brillouin zone is divided into two patches denoted as P_+ for the central patch containing the nodal point $(\frac{\pi}{2}, \frac{\pi}{2})$, P_- for the border patch containing antinodal points $(\pi, 0)$ and $(0, \pi)$, see Fig. 12. Each patch is associated with a momentum independent self-energy $\Sigma_{\pm}(\omega)$.

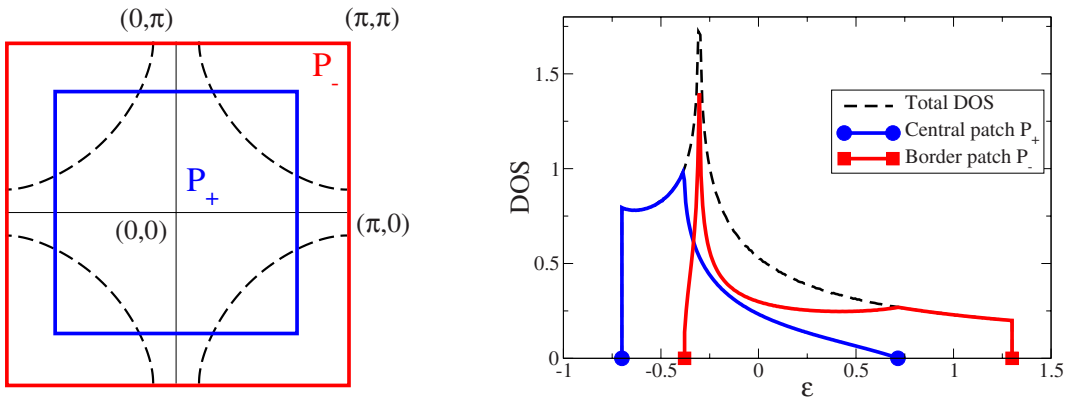


Figure 12: **Left panel:** Partition of the Brillouin zone adopted in both Ref. [5] and this thesis. The central (nodal) part is denoted by P_+ , the border (antinodal) part by P_- . **Right panel:** Partial density of states (DOS) with respect to P_+ and P_- . The lower edge of border patch DOS is denoted by ε_{\min} in the main text. Figures are taken from Ref. [5].

Such a division in momentum space corresponds to a Fourier transformation of the 2-site cluster in real space $c_{i=1,2}^{\dagger}$, hence in the $K = \pm$ representation, the

associated modes are reduced to the even- and odd-orbital combinations

$$c_{\pm\sigma}^\dagger = \frac{1}{\sqrt{2}}(c_{1\sigma}^\dagger \pm c_{2\sigma}^\dagger), \quad (4.13a)$$

$$G_{\pm}(\omega) = \frac{1}{\Omega_{\pm}} \int_{P_{\pm}} d^2\mathbf{k} \frac{1}{\omega + \mu - \varepsilon_{\mathbf{k}} - \Sigma_{\pm}(\omega)}. \quad (4.13b)$$

From the local Green's function, one can clearly see that now the momentum dependency is coarse-grind into the dichotomized Brillouin zone patches P_{\pm} , the representative momenta are $\mathbf{K}_+ = (0, 0)$ and $\mathbf{K}_- = (\pi, \pi)$.

The corresponding impurity model is the 2-impurity Anderson model (2IAM), the cluster Hamiltonian reads:

$$H_{\text{dimer}} = \sum_{i,j=1,2;\sigma=\uparrow,\downarrow} c_{i\sigma}^\dagger [\bar{t}(1 - \delta_{ij}) - \mu\delta_{ij}] c_{j\sigma} + U \sum_{i=1,2} n_{i\uparrow} n_{i\downarrow}, \quad (4.14a)$$

$$\bar{t} = \frac{1}{\Omega_+} \int_{P_+} d^2\mathbf{k} \varepsilon_{\mathbf{k}} = -\frac{1}{\Omega_-} \int_{P_-} d^2\mathbf{k} \varepsilon_{\mathbf{k}}. \quad (4.14b)$$

Since we work with the momentum space, the on-site and hopping terms become diagonal in K representation

$$H_{\text{dimer}} = \sum_{K=\pm,\sigma=\uparrow,\downarrow} c_{K\sigma}^\dagger (K\bar{t} - \mu) c_{K\sigma} + U \sum_{i=1,2} n_{i\uparrow} n_{i\downarrow}. \quad (4.15)$$

As explained in section 2.6, quantities such as the self-energy and Green's function are diagonal in DCA as well.

In our NRG implementation, the concrete form of interaction term in K space is not so important, as the impurity Hamiltonian can be defined in a mixed representation, i.e. $H_{\text{dimer}} = H_{\text{hop}} + H_{\text{int}}$, where H_{hop} is diagonal in K as in Eq. (4.15) and H_{int} remains in lattice representation as in Eq. (4.14). Because the NRG solver eventually executes the iterative diagonalization with a specified impurity operator, in our case $c_K^{(\dagger)}$, encoded via a three-leg tensor, it can return the self-energy $\Sigma_{\pm}(\omega)$ in correct representation.

4.4 Three-band Hubbard model (Emery model)

The simplest theoretical description of copper oxides is formulated by single-band Hubbard model, which contains one effective Cu $3d_{x^2-y^2}$ orbital and successfully describes the so-called Mott Hubbard metal-insulator transition. Despite of that, the single-band model encounters difficulty when it comes to the scenarios concerning the doping dependence of various properties. In the end of 1980's, an effective three-band Hubbard model is proposed by V.J. Emery. It is demonstrated that the properties of high- T_c oxide superconductors can be described by this model, in which the charge carriers are holes in the O $2p_{x/y}$ orbitals [9].

In the Emery model, the nearest neighbor hopping between the $3d$ -orbital of the Cu and $2p_{x/y}$ -orbital of the O, and the hopping between $2p_x$ and $2p_y$ are

included. The Hamiltonian in real space reads [32]:

$$\begin{aligned}
 H &= H_{d(\text{on-site})} + H_{p(\text{on-site})} + H_{dp_x} + H_{dp_y} + H_{p_x p_y} \\
 &= \sum_{\mathbf{r}} (\varepsilon_d - \mu) d_{\mathbf{r}}^{\dagger} d_{\mathbf{r}} + \sum_{\mathbf{r}} U_d n_{\mathbf{r}\uparrow}^d n_{\mathbf{r}\downarrow}^d \\
 &+ \sum_{\mathbf{r}} (\varepsilon_p - \mu) (p_{x\mathbf{r}}^{\dagger} p_{x\mathbf{r}} + p_{y\mathbf{r}}^{\dagger} p_{y\mathbf{r}}) \\
 &+ t_{dp} \sum_{\mathbf{r}} (d_{\mathbf{r}}^{\dagger} p_{x\mathbf{r}+\delta_x} - d_{\mathbf{r}}^{\dagger} p_{x\mathbf{r}-\delta_x}) + h.c. \\
 &+ t_{dp} \sum_{\mathbf{r}} (d_{\mathbf{r}}^{\dagger} p_{y\mathbf{r}+\delta_y} - d_{\mathbf{r}}^{\dagger} p_{y\mathbf{r}-\delta_y}) + h.c. \\
 &+ t_{pp} \sum_{\mathbf{r}} (p_{x\mathbf{r}+\delta_x}^{\dagger} p_{y\mathbf{r}+\delta_y} + h.c.) - t_{pp} \sum_{\mathbf{r}} (p_{x\mathbf{r}+\delta_x}^{\dagger} p_{y\mathbf{r}-\delta_y} + h.c.),
 \end{aligned} \tag{4.16}$$

where ε_d and ε_p are on-site energies of d and $p_{x/y}$ -orbitals, μ the chemical potential. $\delta_{x/y}$ are vectors pointing from d to $p_{x/y}$. The summation of \mathbf{r} runs over all the unit cells, and the summation over the spin σ is understood but not displayed explicitly, except in the Coulomb interaction term on the d -orbitals. In this formalism, all hopping amplitudes (i.e. t_{dp} and t_{pp}) are conventionally defined as positive numbers, with phase factors explicitly indicated by minus signs in the Hamiltonian. The full hopping configuration is illustrated in Fig. 13.

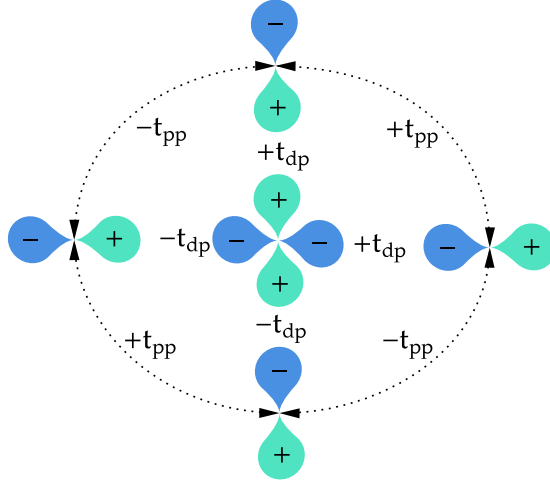


Figure 13: Configuration of the relevant three orbitals in Emery model. The wavefunction phases of $d_{x^2-y^2}$ and $p_{x/y}$ orbitals are indicated by \pm signs, along with the hopping amplitudes and their corresponding phase conventions. In this thesis, t_{dp} and t_{pp} are both positive numbers.

To transform into momentum space, we apply Fourier transformation to each orbital

$$\alpha_{\mathbf{r}}^{(\dagger)} = \frac{1}{\sqrt{N}} \sum_{\mathbf{k}} e^{\pm i\mathbf{k}\cdot\mathbf{r}} \alpha_{\mathbf{k}}^{(\dagger)}, \tag{4.17}$$

here $\alpha_{\mathbf{r}}^{(\dagger)}$ and $\alpha_{\mathbf{k}}^{(\dagger)}$ are annihilation (creation) operators for orbitals $\alpha = d, p_x, p_y$ in real and momentum space.

$$\begin{aligned}
 H_{dp_x} &= t_{dp} \sum_{\mathbf{r}} (d_{\mathbf{r}}^{\dagger} p_{x\mathbf{r}+\boldsymbol{\delta}_x} - d_{\mathbf{r}}^{\dagger} p_{x\mathbf{r}-\boldsymbol{\delta}_x}) + h.c. \\
 &= t_{dp} \sum_{\mathbf{r}} \left\{ \frac{1}{\sqrt{N}} \sum_{\mathbf{k}} e^{-i\mathbf{k}\cdot\mathbf{r}} d_{\mathbf{k}}^{\dagger} \frac{1}{\sqrt{N}} \sum_{\mathbf{k}'} e^{i\mathbf{k}'\cdot(\mathbf{r}+\boldsymbol{\delta}_x)} p_{x\mathbf{k}'} \right. \\
 &\quad \left. - \frac{1}{\sqrt{N}} \sum_{\mathbf{k}} e^{-i\mathbf{k}\cdot\mathbf{r}} d_{\mathbf{k}}^{\dagger} \frac{1}{\sqrt{N}} \sum_{\mathbf{k}'} e^{i\mathbf{k}'\cdot(\mathbf{r}-\boldsymbol{\delta}_x)} p_{x\mathbf{k}'} + h.c. \right\} \\
 &= t_{dp} \left\{ \frac{1}{N} \sum_{\mathbf{r}} e^{i(\mathbf{k}-\mathbf{k}')\cdot\mathbf{r}} \sum_{\mathbf{k}\mathbf{k}'} e^{i\mathbf{k}'\cdot\boldsymbol{\delta}_x} d_{\mathbf{k}}^{\dagger} p_{x\mathbf{k}'} - \frac{1}{N} \sum_{\mathbf{r}} e^{i(\mathbf{k}-\mathbf{k}')\cdot\mathbf{r}} \sum_{\mathbf{k}\mathbf{k}'} e^{-i\mathbf{k}'\cdot\boldsymbol{\delta}_x} d_{\mathbf{k}}^{\dagger} p_{x\mathbf{k}'} + h.c. \right\} \\
 &= t_{dp} \sum_{\mathbf{k}} (e^{i\mathbf{k}\cdot\boldsymbol{\delta}_x} - e^{-i\mathbf{k}\cdot\boldsymbol{\delta}_x}) d_{\mathbf{k}}^{\dagger} p_{x\mathbf{k}} + h.c. \\
 &= \sum_{\mathbf{k}} 2it_{dp} \sin(\mathbf{k}\cdot\boldsymbol{\delta}_x) d_{\mathbf{k}}^{\dagger} p_{x\mathbf{k}} - 2it_{dp} \sin(\mathbf{k}\cdot\boldsymbol{\delta}_x) p_{x\mathbf{k}}^{\dagger} d_{\mathbf{k}}.
 \end{aligned} \tag{4.18}$$

In the fourth line the equation $\frac{1}{N} \sum_{\mathbf{r}} e^{i(\mathbf{k}-\mathbf{k}')\cdot\mathbf{r}} = \delta_{\mathbf{k},\mathbf{k}'}$ is used. Note that $\pm 2it_{dp} \sin(\mathbf{k}\cdot\boldsymbol{\delta}_x)$ terms originate from the hopping between d and p_x , with an opposite phase convention. $d - p_y$ hopping follows the same derivation

$$H_{dp_y} = \sum_{\mathbf{k}} 2it_{dp} \sin(\mathbf{k}\cdot\boldsymbol{\delta}_y) d_{\mathbf{k}}^{\dagger} p_{y\mathbf{k}} - 2it_{dp} \sin(\mathbf{k}\cdot\boldsymbol{\delta}_y) p_{y\mathbf{k}}^{\dagger} d_{\mathbf{k}}. \tag{4.19}$$

$H_{p_x p_y}$ includes two directions of hopping, which are denoted by the corresponding sign of phase

$$\begin{aligned}
 H_{p_x p_y}^+ &= t_{pp} \sum_{\mathbf{k}} (e^{i\mathbf{k}(\boldsymbol{\delta}_y - \boldsymbol{\delta}_x)} + e^{-i\mathbf{k}(\boldsymbol{\delta}_y - \boldsymbol{\delta}_x)}) p_{x\mathbf{k}}^{\dagger} p_{y\mathbf{k}} + h.c. \\
 &= \sum_{\mathbf{k}} 2t_{pp} \cos[\mathbf{k}(\boldsymbol{\delta}_y - \boldsymbol{\delta}_x)] (p_{x\mathbf{k}}^{\dagger} p_{y\mathbf{k}} + h.c.), \\
 H_{p_x p_y}^- &= \sum_{\mathbf{k}} -2t_{pp} \cos[\mathbf{k}(\boldsymbol{\delta}_y + \boldsymbol{\delta}_x)] (p_{x\mathbf{k}}^{\dagger} p_{y\mathbf{k}} + h.c.), \\
 H_{p_x p_y} &= H_{p_x p_y}^+ + H_{p_x p_y}^- \\
 &= \sum_{\mathbf{k}} 2t_{pp} \{ \cos[\mathbf{k}(\boldsymbol{\delta}_y - \boldsymbol{\delta}_x)] - \cos[\mathbf{k}(\boldsymbol{\delta}_y + \boldsymbol{\delta}_x)] \} (p_{x\mathbf{k}}^{\dagger} p_{y\mathbf{k}} + h.c.) \\
 &= \sum_{\mathbf{k}} 4t_{pp} \sin(\mathbf{k}\cdot\boldsymbol{\delta}_x) \sin(\mathbf{k}\cdot\boldsymbol{\delta}_y) (p_{x\mathbf{k}}^{\dagger} p_{y\mathbf{k}} + h.c.),
 \end{aligned} \tag{4.20}$$

here sum to product formula is used in the last line. Combining Eq. (4.18), Eq. (4.19), Eq. (4.20) and the on-site energy terms, we arrive at the complete non-interacting Hamiltonian for Emery model

$$H_0 = \sum_{\mathbf{k}} \left(d_{\mathbf{k}}^{\dagger}, p_{x\mathbf{k}}^{\dagger}, p_{y\mathbf{k}}^{\dagger} \right) \mathbf{h}(\mathbf{k}) \begin{pmatrix} d_{\mathbf{k}} \\ p_{x\mathbf{k}} \\ p_{y\mathbf{k}} \end{pmatrix}, \tag{4.21}$$

where $\mathbf{h}(\mathbf{k})$ is a 3×3 matrix and the spin subscript σ is not displayed

$$\mathbf{h}(\mathbf{k}) = \begin{pmatrix} \varepsilon_d - \mu & 2it_{dp} \sin(\mathbf{k} \cdot \boldsymbol{\delta}_x) & 2it_{dp} \sin(\mathbf{k} \cdot \boldsymbol{\delta}_y) \\ -2it_{dp} \sin(\mathbf{k} \cdot \boldsymbol{\delta}_x) & \varepsilon_p - \mu & 4t_{pp} \sin(\mathbf{k} \cdot \boldsymbol{\delta}_x) \sin(\mathbf{k} \cdot \boldsymbol{\delta}_y) \\ -2it_{dp} \sin(\mathbf{k} \cdot \boldsymbol{\delta}_y) & 4t_{pp} \sin(\mathbf{k} \cdot \boldsymbol{\delta}_x) \sin(\mathbf{k} \cdot \boldsymbol{\delta}_y) & \varepsilon_p - \mu \end{pmatrix}. \quad (4.22)$$

A unitary transform can tridiagonalize the matrix $\mathbf{h}(\mathbf{k})$. The transform essentially mixes p_x and p_y orbitals into two new orbitals referred to as bonding and non-bonding orbitals [33], denoted as $p_{\mathbf{k}}$ and $\bar{p}_{\mathbf{k}}$

$$p_{\mathbf{k}} = \frac{i}{\gamma_{\mathbf{k}}} \sin(\mathbf{k} \cdot \boldsymbol{\delta}_x) p_{x\mathbf{k}} - \frac{i}{\gamma_{\mathbf{k}}} \sin(\mathbf{k} \cdot \boldsymbol{\delta}_y) p_{y\mathbf{k}}, \quad (4.23a)$$

$$\bar{p}_{\mathbf{k}} = \frac{i}{\gamma_{\mathbf{k}}} \sin(\mathbf{k} \cdot \boldsymbol{\delta}_x) p_{x\mathbf{k}} + \frac{i}{\gamma_{\mathbf{k}}} \sin(\mathbf{k} \cdot \boldsymbol{\delta}_y) p_{y\mathbf{k}}, \quad (4.23b)$$

where $\gamma_{\mathbf{k}}^2 = \sin^2(\mathbf{k} \cdot \boldsymbol{\delta}_x) + \sin^2(\mathbf{k} \cdot \boldsymbol{\delta}_y)$ is a normalization factor. Since the d orbital is unchanged under this transform, the complete transform matrix can be written as

$$\mathbf{U} = \begin{pmatrix} 1 & 0 & 0 \\ 0 & \frac{i}{\gamma_{\mathbf{k}}} \sin(\mathbf{k} \cdot \boldsymbol{\delta}_x) & -\frac{i}{\gamma_{\mathbf{k}}} \sin(\mathbf{k} \cdot \boldsymbol{\delta}_y) \\ 0 & \frac{i}{\gamma_{\mathbf{k}}} \sin(\mathbf{k} \cdot \boldsymbol{\delta}_x) & \frac{i}{\gamma_{\mathbf{k}}} \sin(\mathbf{k} \cdot \boldsymbol{\delta}_y) \end{pmatrix}. \quad (4.24)$$

Given the transform matrix \mathbf{U} , the non-interacting Hamiltonian is now transformed to

$$\begin{aligned} \bar{\mathbf{h}}(\mathbf{k}) &= \mathbf{U}^\dagger \mathbf{h}(\mathbf{k}) \mathbf{U} \\ &= \begin{pmatrix} \varepsilon_d - \mu & -2t_{dp}\gamma_{\mathbf{k}} & 0 \\ -2t_{dp}\gamma_{\mathbf{k}} & \varepsilon_{p\mathbf{k}} - \mu & t'_{\mathbf{k}} \\ 0 & t'_{\mathbf{k}} & \varepsilon_{\bar{p}\mathbf{k}} - \mu \end{pmatrix}. \end{aligned} \quad (4.25)$$

The matrix elements in Eq. (4.25) are

$$\varepsilon_{p\mathbf{k}} = \varepsilon_p + \frac{8t_{pp}}{\gamma_{\mathbf{k}}^2} \sin^2(\mathbf{k} \cdot \boldsymbol{\delta}_x) \sin^2(\mathbf{k} \cdot \boldsymbol{\delta}_y), \quad (4.26a)$$

$$\varepsilon_{\bar{p}\mathbf{k}} = \varepsilon_p - \frac{8t_{pp}}{\gamma_{\mathbf{k}}^2} \sin^2(\mathbf{k} \cdot \boldsymbol{\delta}_x) \sin^2(\mathbf{k} \cdot \boldsymbol{\delta}_y), \quad (4.26b)$$

$$t'_{\mathbf{k}} = -\frac{4t_{pp}}{\gamma_{\mathbf{k}}^2} \sin(\mathbf{k} \cdot \boldsymbol{\delta}_x) \sin(\mathbf{k} \cdot \boldsymbol{\delta}_y) (\sin^2(\mathbf{k} \cdot \boldsymbol{\delta}_x) - \sin^2(\mathbf{k} \cdot \boldsymbol{\delta}_y)). \quad (4.26c)$$

In some articles, e.g. Ref. [34, 35, 36], the next-nearest hopping between p electrons is also considered. As such hopping directions are along either $\boldsymbol{\delta}_x$ or $\boldsymbol{\delta}_y$, it contributes to $\mathbf{h}(\mathbf{k})$ via additional diagonal elements $2t'_{pp} \cos(2\mathbf{k} \cdot \boldsymbol{\delta}_{x/y})$. Furthermore, the unitary transformed matrix would be modified in the same way. In this thesis, we only consider nearest neighbor hopping.

Now it is time to inspect the transformed Hamiltonian \bar{H}_0

$$\begin{aligned}\bar{H}_0 &= \sum_{\mathbf{k}} \left(d_{\mathbf{k}}^\dagger, p_{\mathbf{k}}^\dagger, \bar{p}_{\mathbf{k}}^\dagger \right) \bar{\mathbf{h}}(\mathbf{k}) \begin{pmatrix} d_{\mathbf{k}} \\ p_{\mathbf{k}} \\ \bar{p}_{\mathbf{k}} \end{pmatrix} \\ &= \sum_{\mathbf{k}} (\varepsilon_d - \mu) d_{\mathbf{k}}^\dagger d_{\mathbf{k}} + (\varepsilon_{p\mathbf{k}} - \mu) p_{\mathbf{k}}^\dagger p_{\mathbf{k}} + (\varepsilon_{\bar{p}\mathbf{k}} - \mu) \bar{p}_{\mathbf{k}}^\dagger \bar{p}_{\mathbf{k}} \\ &\quad - 2t_{dp}\gamma_{\mathbf{k}}(d_{\mathbf{k}}^\dagger p_{\mathbf{k}} + p_{\mathbf{k}}^\dagger d_{\mathbf{k}}) + t'_{\mathbf{k}}(p_{\mathbf{k}}^\dagger \bar{p}_{\mathbf{k}} + \bar{p}_{\mathbf{k}}^\dagger p_{\mathbf{k}}).\end{aligned}\quad (4.27)$$

The structure can be clearly seen via the above equation: in this bonding/non-bonding representation, bonding p is coupled to d and \bar{p} respectively, while non-bonding \bar{p} is decoupled from d . When $t_{dp} = 0$, the coupling between d and p vanishes and gives rise to a dispersionless p band. This can be seen from left panel in Fig. 14.

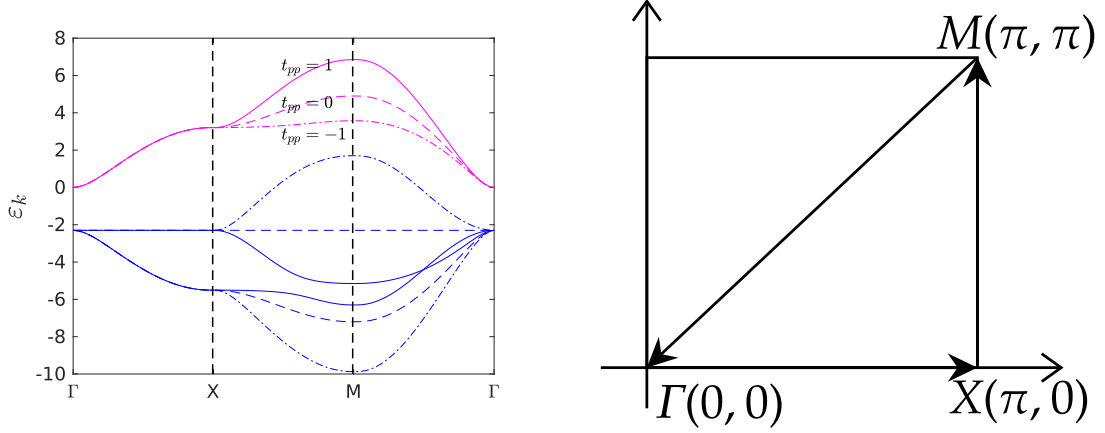


Figure 14: **Left panel:** Dispersion relations obtained from direct diagonalization of $\mathbf{h}(\mathbf{k})$. $\varepsilon_d = 0$, $\varepsilon_p = -2.3$, $t_{dp} = 2.1$, $t_{pp} = \pm 1, 0$. Rose red curves corresponds to the d -band, blue curves the p -bands. Solid lines with $t_{pp} = +1$, whereas the dashed lines with $t_{pp} = 0$ and $t_{pp} = -1$. **Right panel:** The path connecting the three high-symmetry points Γ , X , and M .

The tridiagonal $\bar{\mathbf{h}}(\mathbf{k})$ makes it possible to derive the Green's function analytically.

$$\mathbf{G}(\mathbf{k}, \omega) = \{(\omega + \mu)\mathbf{1} - \bar{\mathbf{h}}(\mathbf{k}) - \Sigma(\omega)\}^{-1} \quad (4.28)$$

Here, the full interacting Green's function is a 3×3 matrix as three orbitals are involved, $\mathbf{1}$ is unit matrix and $\Sigma(\omega)$ a matrix with only one non-vanishing element

$$\Sigma(\omega) = \begin{pmatrix} \Sigma_d(\omega) & 0 & 0 \\ 0 & 0 & 0 \\ 0 & 0 & 0 \end{pmatrix}. \quad (4.29)$$

In the Emery model, Coulomb interaction on $p_{x/y}$ orbitals is ignored, therefore the self-energy $\Sigma(\omega)$ has a simple form, which takes $\Sigma_d(\omega)$ the self-energy on d orbitals into account only. As $\mathbf{G}^{-1}(\mathbf{k}, \omega)$ retains the tridiagonal form, its inverse can be

evaluated via a continued fraction expansion [32] as seen in section 3.2. Combine Eq. (4.25) and Eq. (4.28), the (d, d) component of $\mathbf{G}(\mathbf{k}, \omega)$, e.g. $G^{dd}(\mathbf{k}, \omega)$ is

$$G^{dd}(\mathbf{k}, \omega) = [\omega + \mu - \varepsilon_d - \Sigma_d(\omega) - \bar{\varepsilon}_{\mathbf{k}}(\omega)]^{-1} = \left[\omega + \mu - \varepsilon_d - \Sigma_d(\omega) - \frac{4t_{dp}^2 \gamma_{\mathbf{k}}^2}{\omega - \varepsilon_{p\mathbf{k}} + \mu - \frac{t_{\mathbf{k}}^2}{\omega - \varepsilon_{\bar{p}\mathbf{k}} + \mu}} \right]^{-1}. \quad (4.30)$$

The above Green's function can be understood as follows: all the hopping effects are encoded in an effective dispersion $\bar{\varepsilon}_{\mathbf{k}}(\omega)$, that takes account dispersion from H_{dp} and H_{pp} in terms of $\gamma_{\mathbf{k}}$ and $\varepsilon_{p/\bar{p}\mathbf{k}}$. We only care about the (d, d) component of $\mathbf{G}(\mathbf{k}, \omega)$ as only the d orbital is interacting and its self-energy $\Sigma_d(\omega)$ comes into play. In this thesis $G^{dd}(\mathbf{k}, \omega)$ is the lattice Green's function that we consider

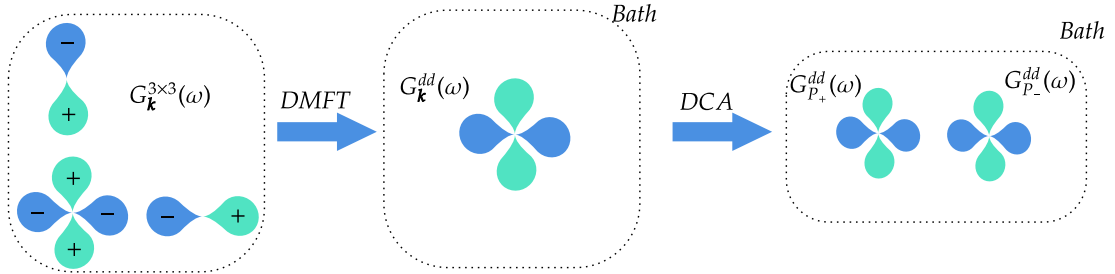


Figure 15: A schematic illustrating the mapping of a three-band lattice problem to an effective single-impurity problem using DMFT, and further to a two-site impurity problem via DCA.

for the DCA self-consistency loop, momentum dependency is averaged out to calculate the local Green's function,

$$G^{dd}(\omega) = \int_{BZ} \frac{d^d \mathbf{k}}{(2\pi)^d} G^{dd}(\mathbf{k}, \omega), \quad (4.31)$$

with which the hybridization function can be obtained via

$$\Gamma_{\text{out}}(\omega) = \text{Im}\{[G^{dd}(\omega)]^{-1} + \Sigma_d(\omega)\}. \quad (4.32)$$

The 2-site DCA generalization follows the same way described in section 4.3, the only difference is that the local Green's function is replaced by $G^{dd}(\omega)$, which contains the spatial correlation from p -orbitals.

5 Numerical Results I (Hubbard Model)

5.1 Spectral functions

Benchmark at finite temperature

The central variable throughout this work is the hole doping level x , we study various dynamical quantities as a function of x , and see how the system evolves and transitions with increasing doping. We begin with the spectral function, benchmarked against Ref. [5], the model Hamiltonian is described in section 4.3. We use $U/t = 10$, $t'/t = -0.3$ in units of $D = 4t = 1$.

Before presenting the results, we define the critical doping x_c as the doping level at which the pseudogap width Δ vanishes.

$$x_c = \min\{x \mid \Delta(x) = 0\}, \quad (5.1)$$

Δ is determined by the position of the first coherent excitation, which is determined by the pole of the antinodal Green's function

$$G_-(\omega) = \int_{P_-} \frac{d^2\mathbf{k}}{(2\pi)^2} \frac{1}{\omega + \mu - \varepsilon_{\mathbf{k}} - \Sigma_-(\omega)}. \quad (5.2)$$

Neglecting the effect of the imaginary part of $\Sigma_-(\omega)$ yields the gap equation

$$\Delta + \mu - \varepsilon_{\min} - \text{Re}\Sigma_-(\Delta) = 0. \quad (5.3)$$

Here ε_{\min} is the lower edge of the partial density of states with respect to the border patch, as shown in the left panel of Fig. 12.

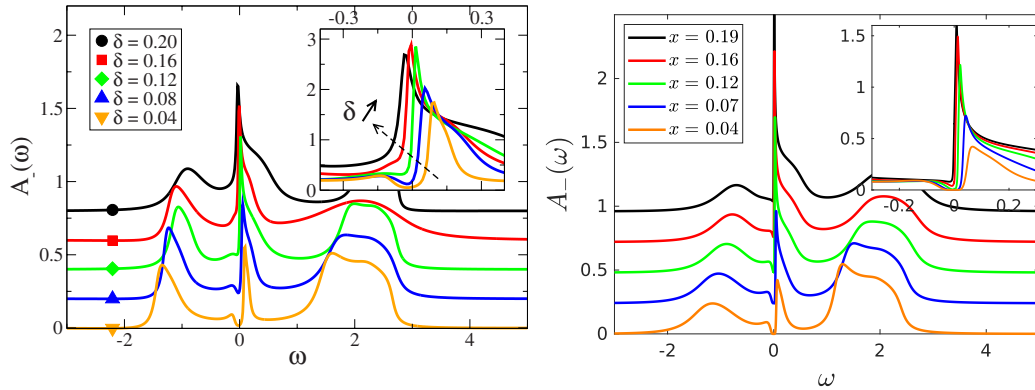


Figure 16: **Left panel:** Antinodal spectral function $A_-(\omega)$ at inverse temperature $\beta = 200$ for several doping values, presenting the forming of the pseudogap. It is taken from Ref. [5]. **Right panel:** Our corresponding 2-site DCA+NRG computation. The pseudogap at doping levels below x_c exhibits higher resolution and greater robustness against thermal fluctuations.

Fig. 16 demonstrates the border patch (antinodal) spectral function, denoted as $A_-(\omega)$. The left panel is adapted from Ref. [5], the right panel presents our

results obtained using DCA+NRG. The key parameters of the NRG solver are set as follows: number of kept states $N_{\text{keep}} = 13000$, and the logarithmic discretization parameter $\Lambda = 3$. These parameters are made to achieve a better resolution for low energy behavior, and suffice to accurately address the two-impurity model. Model parameters are set to be aligned with Ref. [5].

From both left and right panels in Fig. 16, one can see the well-established upper and lower Hubbard bands at high energies, along with a central peak near the Fermi level. At high doping, the peak is centered at $\omega = 0$, forming a quasiparticle peak as described in Fermi liquid theory. As the doping is reduced, the peak is shifted toward $\omega > 0$, and the spectral weight at $\omega = 0$ is strongly suppressed, forming a pseudogap in the spectral function $A_-(\omega)$. By solving the gap equation Eq. (5.1), the critical doping is determined as $x_c = 16\%$ for both cases. A detailed calculation of Δ by DCA+NRG scheme is shown in Ref. [37].

In the benchmark from Ref. [5] (left panel of Fig. 16), the spectral weight at the Fermi level becomes finite and gradually loses the dip-like suppression even for doping levels below the critical value ($x \lesssim x_c$). This behavior is attributed to thermal excitations and the limited resolution at $\omega \sim 0$ inherent to the Quantum Monte Carlo (QMC) impurity solver combined with analytical continuation.

In our results (right panel of Fig. 16), the pseudogap feature, i.e. the dip-like suppression at the Fermi level persists beyond the critical doping, e.g. $x = 20\%$, with a finite spectral weight, $A_-(\omega = 0) \gtrsim 0$. This reflects the high-resolution of our NRG solver in the low-energy region.

In summary, our results show excellent agreements with the result of Ref. [5]. Furthermore, a more pronounced pseudogap is reproduced for $x < x_c$. Notably, a suppression in spectral weight remains visible even near $x \sim x_c$, and appears to be more robust against thermal excitations compared to the findings in Ref. [5].

Our results at zero temperature

From this point onward, we focus on the case of zero-temperature ($\beta = 10^{10}$) to identify a potential quantum critical point (QCP) between the pseudogap and Fermi liquid phases. At zero temperature, thermal fluctuations are entirely suppressed, allowing the spectral function to accurately reflect the gap width Δ . Hence, in this case we define x_c as the doping above which the border patch spectral weight becomes non-vanishing at the Fermi level, i.e. the insulator-to-metal transition occurs.

$$x_c = \min\{x \mid A_-(\omega = 0) > 0\} \quad (5.4)$$

Fig. 17 shows calculations of $A_{\pm}(\omega)$ on a broader doping range from 5.7% to 43.7%. The insulator-to-metal transition that occurs at $x_c = 17.2\%$ is shown in the inset of right panel in Fig. 17. When $x < x_c$, the pseudogap has a finite width, hence the border patch is insulating. As x increases and exceeds x_c , the gap width decreases, leading to a finite spectral weight at the Fermi level, which then increases in a continuous manner, as illustrated in the right panel of Fig. 17.

The spectral function of the central patch (nodal region), $A_+(\omega)$, is shown in the left panel of Fig. 17. $A_+(\omega)$ exhibits much weaker dependence on doping and

gradually recovers the main feature of the non-interacting density of states, as seen in the left panel of Fig. 12. A small dip near the Fermi level corresponds to the prominent peak in $A_-(\omega)$. As doping increases, the dip is continuously filled, indicating a smooth transition.

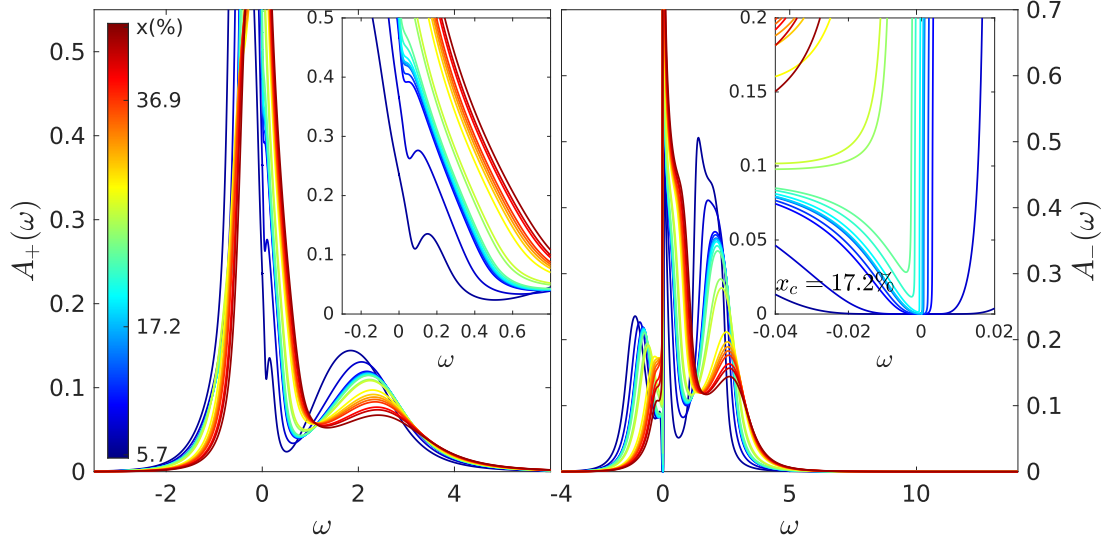


Figure 17: **Left panel:** Spectral function for the central DCA patch of momentum $(0, 0)$, at doping ranging from 5.7% to 43.7% and inverse temperature $\beta = 10^{10}$, which holds also for the right panel. **Right panel:** The border DCA patch of momentum (π, π) . The insets show $\omega \sim 0$ in more detail.

Fermi surface and electronic structure

The structure of the Fermi surface defined as

$$\varepsilon_{\mathbf{k}} + \text{Re}\Sigma(\mathbf{k}, \omega = 0) - \mu = 0, \quad (5.5)$$

can be observed from the spectral function at Fermi level $A(\mathbf{k}, \omega = 0)$ and is shown in Fig. 18 as function of doping x . The momentum dependence arises from both the dispersion $\varepsilon_{\mathbf{k}}$ and the self-energy $\Sigma(\mathbf{k}, \omega)$. In our case, the self-energy is defined on a dichotomized Brillouin zone, with only two coarse-grained momentum resolutions denoted as $\Sigma_{\pm}(\omega)$.

This is illustrated in the upper row of Fig. 18, where no interpolation is employed. Consequently, the Fermi surface presents discontinuities between central and border patches. The central patch displays an arc-like region with finite spectral weights at low doping $x < x_c$, whereas the border patch is completely gapped out. At doping above x_c , the border patch recovers coherence, exhibiting a Fermi surface contributions around $(\pi, 0)$ and $(0, \pi)$ in antinodal regions. This emphasizes the insulator-to-metal transition of the border patch, while the central patch is always metallic for finite doping $x \neq 0$.

In the lower row of Fig. 18, the cumulant interpolation described in section 2.6 is applied. At a low doping level $x = 11.4\%$, the Fermi arc, as observed in

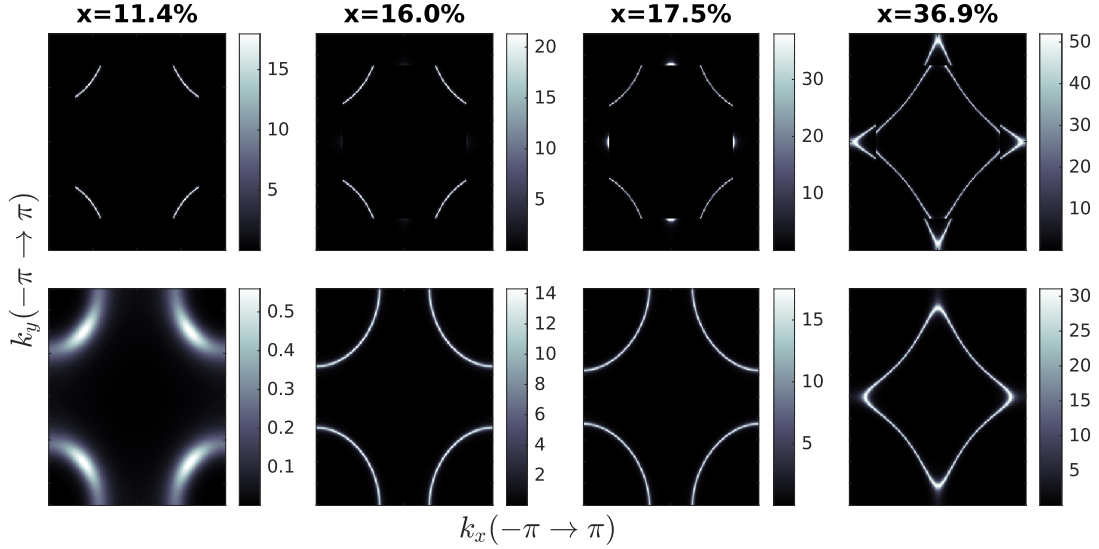


Figure 18: **Upper row:** Spectral function at the Fermi level $A(\mathbf{k}, \omega = 0)$ without interpolation between patches. **Lower row:** With cumulant interpolation. The columns read from left to right present doping across x_c , emphasizing the continuous transition.

ARPES experiments [2], can be clearly recognized. At an intermediate doping level $x = 16.0\% < x_c$, the Fermi surface emerges, even without the spectral contribution from the border patch, as shown in the corresponding upper panel. When doped above the critical point $x = 17.5\% > x_c$, the Fermi surface maintains its hole-like character without any evidence of a quantum critical behavior. At higher doping levels $x \gg x_c$, the hole-like Fermi surface expands and eventually intersects itself at a certain doping level, forming a closed Fermi surface around $(0, 0)$.

To summarize, while the insulator-to-metal transition is observed around the critical doping level x_c , no indication of genuine quantum criticality is captured, while at lower doping values a crossover-like behavior forms Fermi-arcs.

5.2 Self-energy and quasiparticle weight

As discussed in the last chapter, if a system can be described by Fermi liquid theory under a certain energy scale, the imaginary part of zero-temperature self-energy has to obey the quadratic form $-\text{Im}\Sigma(\omega) \sim \omega^2$. Fig. 19 shows the imaginary part of self-energy in both central and border patches.

For underdoped cases ($x < x_c$), the broadening of discrete δ -peaks from NRG results leads to oscillations in the low-energy region, rendering the quadratic fitting unreliable. Thus, we only use one of the curves ($x = 43.7\%$) and fit it with a quadratic function $f(\omega) = c \cdot \omega^2$. For well-established Fermi liquid behavior, this fitting holds over a relatively larger region, $[-\omega_{\text{FL}}, \omega_{\text{FL}}]$, where ω_{FL} refers to the Fermi liquid energy scale. With this quadratic reference, we analyze the asymptotic behavior of $-\text{Im}\Sigma_{\pm}(\omega)$ within a specific energy range

$\Delta\omega \equiv [10^{-3}, 10^{-2}]$.

In the underdoped regime ($x < x_c$), the curves exhibit a steeper slope than ω^2 , and cannot be adequately fitted by a quadratic function without significant deviation, indicating the absence of Fermi liquid behavior within the range $\Delta\omega$. However, as doping increases and approaches x_c , the slope gradually decreases, and the curves transition smoothly into the overdoped regime ($x > x_c$). Finally, the curves converge towards the quadratic reference ω^2 , signifying the onset of Fermi liquid behavior within $\Delta\omega$.

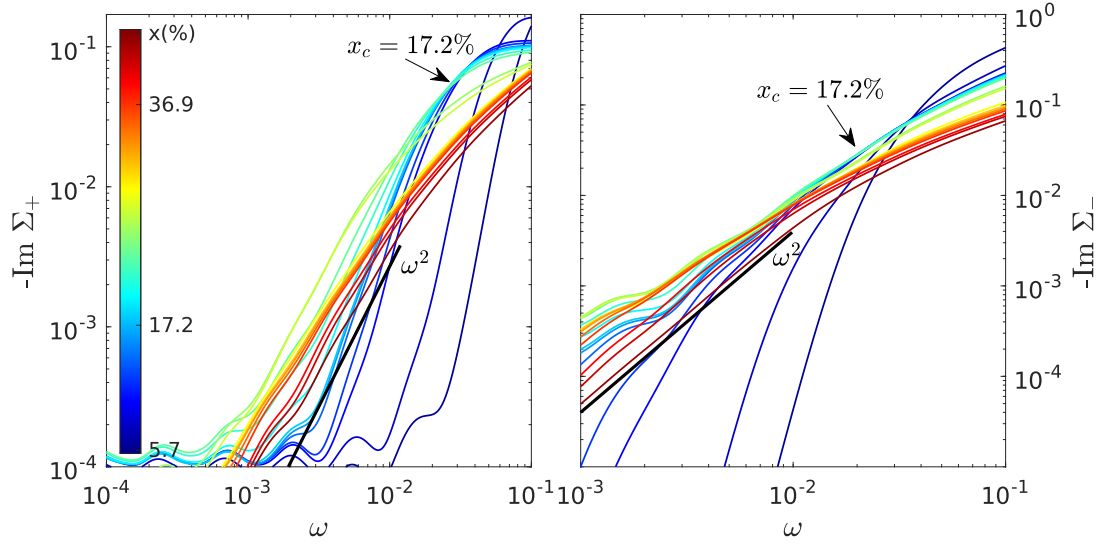


Figure 19: **Left panel:** The imaginary part of the self-energy for the central patch is shown. The curve at a doping level of $x = 43.7\%$ is fitted with a quadratic function, represented by the dark solid line. The curves first evolve toward x_c and then approach the quadratic reference with an increasing doping level. **Right panel:** The imaginary part of the self-energy for the border patch is presented, showing a similar trend to that observed in the central patch.

To address the oscillations in self-energies and examine Fermi liquid behavior in the lower energy region ($\omega < 10^{-2}$), a more detailed investigation of the Fermi liquid energy scale ω_{FL} , along with a systematic analysis based on susceptibilities, is presented in the next section.

Quasiparticle weight

Fig. 20 shows the quasiparticle weight, defined by Eq. (4.7), for the two momentum patches and their average as a function of doping, marked by solid black lines. The dashed lines represent the derivative of the quasiparticle weight with respect to the doping level, i.e. $\Delta Z/\Delta x$, highlighting the region of maximal change.

At low doping, Z_+ initially reduces with increasing doping, while Z_- in contrast increases. As doping level surpasses x_c , Z_- keeps the increasing trend throughout the entire process, while Z_+ stops decreasing and begins to increase.

Such an initial decrease can be observed in Ref. [5] as well, as shown in Fig. 21,

although it is not as pronounced as our result, because the model is calculated at a finite temperature $\beta = 200$.

In our zero temperature results, the initial decrease in the underdoped region of Z_+ is much more pronounced than in Ref. [5]. In the derivative $\Delta Z/\Delta x$, a sharp valley appears at the critical point x_c . For Z_- , it nearly displays a linear dependence on doping, and the variation at x_c is less marked.

The increase in quasiparticle weight in the border patch Z_- , resulting from the gradual reduction of the gap-like feature around x_c , is counteracted by the sharp decline in the quasiparticle weight in the central patch Z_+ , at low doping near x_c . This interplay leads to an overall decrease in the total quasiparticle weight, Z_{tot} . Consequently, the non-monotonic behavior of Z_{tot} as a function of x is observed. Nonetheless, the quasiparticle weights remain well-defined, neither diverging nor vanishing, thereby ruling out any indication of critical behavior.

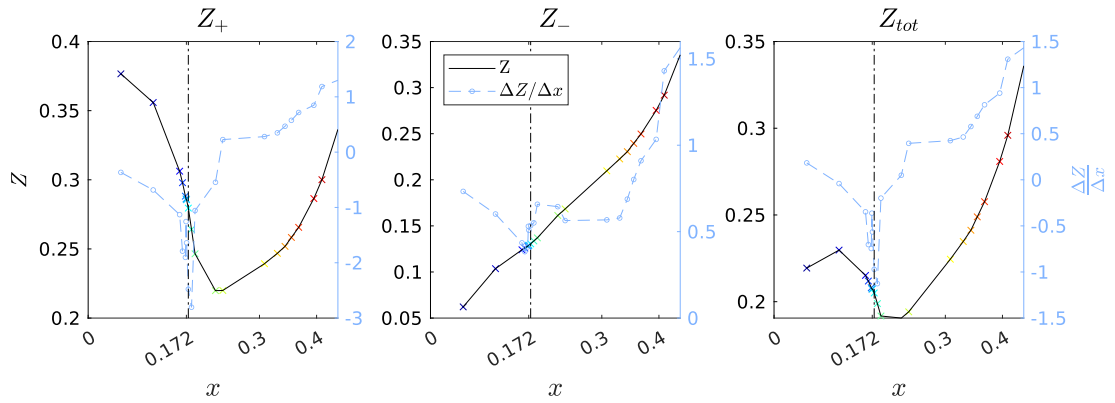


Figure 20: **Left panel:** The quasiparticle weight for the central patch. **Middle panel:** The quasiparticle weight for the border patch. **Right panel:** The averaged quasiparticle weight. The black solid line with colored markers represents Z , while the gray dashed lines indicate its derivative with respect to doping x . The vertical dash-dotted line marks x_c .

The difference between Z_+ and Z_- vanishes above a certain doping level, x_{cvg} (cvg refers to the convergence of $\mu - \text{Re}\Sigma_-(0)$, as shown in Fig. 22), which marks the point where differentiation between the two patches diminishes. This is illustrated in Fig. 22, where the patch differentiation is quantified by the real part of the self-energy at the Fermi level, $\text{Re}\Sigma_{\pm}(0)$. As the doping level surpasses $x_{\text{cvg}} = 31\%$, the dichotomy in momentum space disappears, indicating a transition to a fully metallic state. In this regime, the system can be effectively described by single-site DMFT, leading to no distinction between Z_+ and Z_- .

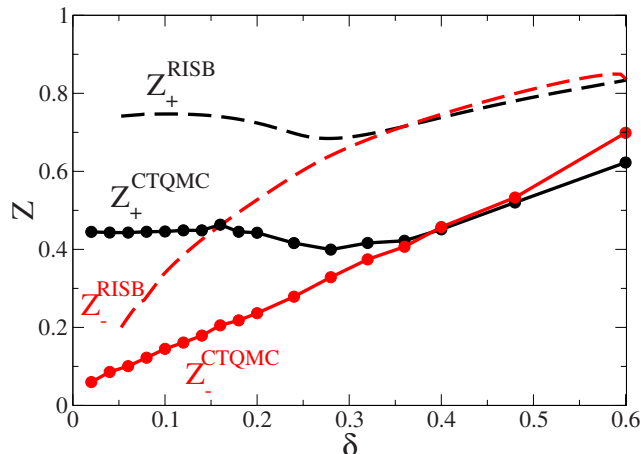


Figure 21: Quasiparticle weights evaluated using continuous time-quantum Monte Carlo (CTQMC) and rotationally invariant slave bosons (RISB) at finite temperature $\beta = 200$. The reduction in Z_+ is visible but less pronounced compared to our zero temperature results. This figure is adapted from Ref. [5].

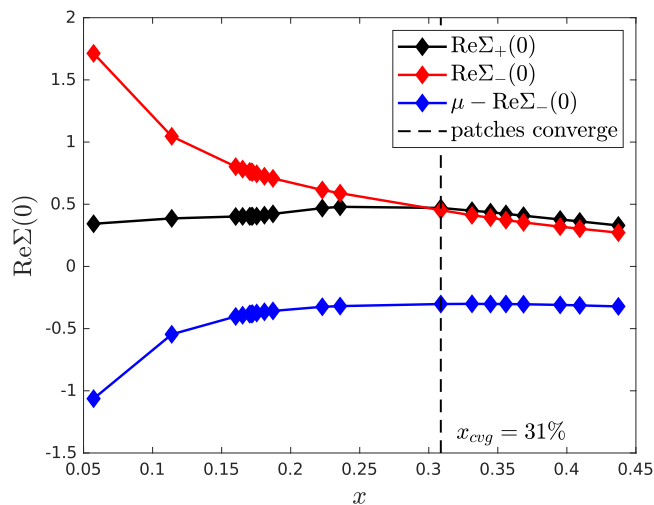


Figure 22: Real part of self-energies at Fermi level, as a function of doping x . $\text{Re}\Sigma_{\pm}(0)$ merge at $x_{cvg} = 31\%$, beyond which the difference in Z_{\pm} vanishes.

5.3 Susceptibility and phase diagram

In correlated systems, susceptibilities are of interest as they reflect how the system responds to perturbations and can provide valuable information about phase transitions.

In the framework of NRG, susceptibilities can be computed as retarded correlators of two bosonic operators, \mathcal{O}_1 and \mathcal{O}_2 , defined in the impurity Hilbert space

$$\chi(t) = \langle \mathcal{O}_1 | | \mathcal{O}_2 \rangle (t) = -i\Theta(t)\langle [\mathcal{O}_1(t), \mathcal{O}_2] \rangle, \quad (5.6)$$

where the spectral part χ'' of the susceptibility is defined by $\chi = \chi' - i\pi\chi''$ and

$$\chi''(\omega) = \frac{1}{2\pi} \int dt e^{i\omega t} \langle [\mathcal{O}_1(t), \mathcal{O}_2] \rangle. \quad (5.7)$$

In our implementation, such a correlator is evaluated using the fdmNRG approach, involving the local current and spin operators, respectively, and utilizing the Lehmann representation [25]. The two types of susceptibilities are defined as follows:

$$\chi_j'' = \langle j | |j \rangle_\omega, \text{ where } j = -it(c_1^\dagger c_2 - c_2^\dagger c_1), \quad (5.8a)$$

$$\chi_S'' = \langle S_{loc} | |S_{loc} \rangle_\omega, \text{ where } S_{loc} = \frac{1}{\sqrt{2}} \sum_{\alpha\alpha'} c_{1\alpha}^\dagger \sigma_{\alpha\alpha'}^z c_{2\alpha'}. \quad (5.8b)$$

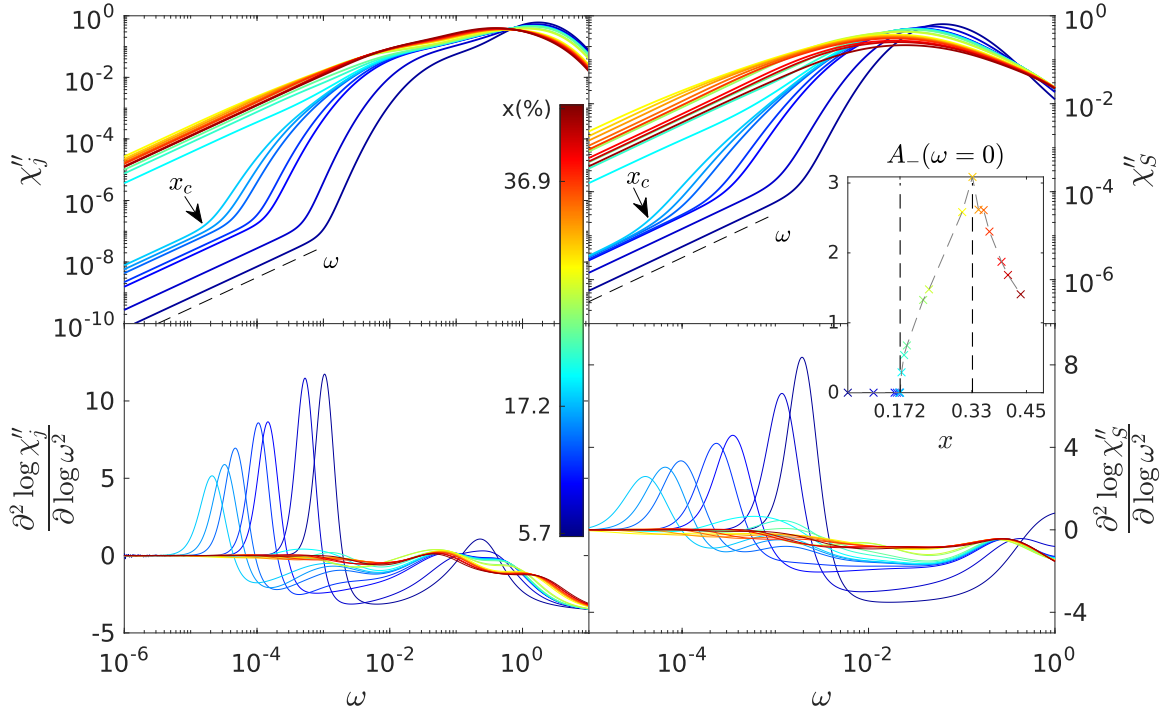


Figure 23: **Upper panels:** Current susceptibility χ_j'' and spin (magnetic) susceptibility χ_S'' . When the border patch is gapped ($x < x_c$), the curves exhibit an upward kink. As the doping level increases beyond x_c , the curves transition into a downward kink. Both χ_j'' and χ_S'' show similar behavior. **Lower panels:** second derivative of $\chi_{j/S}''$, where the extremum coordinates are used to determine ω_{FL} .

We begin by analyzing the near-static limit, $\chi_{j/S}''(\omega \rightarrow 0)$, which is closely related to the spectral function at the Fermi level, $A_-(\omega = 0)$, as illustrated in the inset of Fig. 23.

For $x < x_c$, the border patch is gapped out, resulting in lower electron density and thus suppressed susceptibilities. For $x > x_c$, the pseudogap is filled, and

$A_-(\omega = 0)$ increases, leading to higher electron density and causing the leap in $\chi''_{j/S}(\omega \rightarrow 0)$ at x_c . As the doping level further increases beyond $x = 33.0\%$, $A_-(\omega = 0)$ decreases, resulting in a suppression of $\chi''_{j/S}$.

In summary, the change observed in $\chi''_{j/S}(\omega \rightarrow 0)$ is driven by the insulator-to-metal transition in the border patch, consistent with the continuous transition described in the spectral function and self-energy.

Phase diagram

To investigate the potential pseudogap-to-Fermi liquid phase transition, the Fermi liquid energy scale ω_{FL} serves as a key indicator. It is defined as the crossover scale, below which the Fermi liquid emerges, characterized by a linear scaling of the susceptibility, $\chi''_{j/S} \sim \omega$, as predicted by Fermi liquid theory. Consequently, the extremum of the second derivative of $\chi''_{j/S}$ can be a feasible measure for locating the part, where $\chi''_{j/S}$ stops being linear. Therefore, we define ω_{FL} as the extremum of the second derivative $\frac{\partial^2 \log \chi''_{j/S}}{\partial (\log \omega)^2}$.

In Fig. 23, susceptibilities $\chi''_{j/S}$ and the second derivatives are shown in appropriate double log or linear-log scale. The upper panels demonstrate χ''_j and χ''_S . For $x < x_c$, one can see a series of upward kinks in the low frequency regime, i.e. peaks in terms of second derivative. The positions of these peaks label the corresponding energy scales, which decrease with the increasing x . For $x > x_c$, these upward kinks initially remain the peak-like feature, and consequently transition to a series of downward kinks progressively, corresponding to the minima in the second derivative. As a result, ω_{FL} increase with x , consistent with the well-established metallic nature of overdoped systems. The unexpected fluctuations of ω_{FL} in the overdoped regime are discussed in Appendix A.

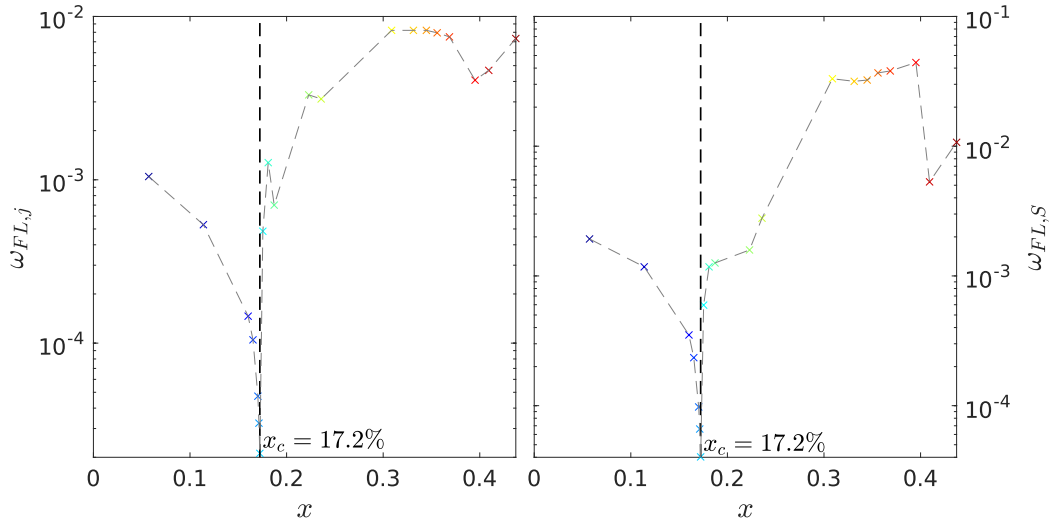


Figure 24: **Left panel:** The phase diagram of the extracted energy scale ω_{FL} , determined from χ''_j , as a function of doping x . **Right panel:** The phase diagram determined by χ''_S . The critical doping in both cases is $x_c = 17.2\%$, consistent with the x_c determined via $A_-(\omega)$.

The extracted crossover scale ω_{FL} as function of doping x is shown in Fig. 24 to visualize the reduction of ω_{FL} towards x_c . Both plots display a valley between underdoped and overdoped regime. The Fermi liquid scale ω_{FL} diminishes down to a value of $\omega_{\text{FL}} \sim 10^{-5}$ as doping approaches x_c , where we sampled x with a step size of $\Delta x \sim 0.2\%$.

However, the Fermi liquid scale never vanishes completely. This behavior highlights the significance of spatial correlations and suggests a possible breakdown of Fermi liquid theory, motivating further investigations involving multiple orbitals or larger cluster sizes.

Therefore, we reiterate that this is not a genuine quantum phase transition between the pseudogap and Fermi liquid phases.

5.4 Energy flow

As discussed in section 3.6, the fixed point in energy flow can reflect the existence of Fermi liquid and provides a measure of the characteristic energy scale. Fig. 25 illustrates the energy flow of the border patch for various doping values, with only even iterations shown. Each energy flow is labeled by the corresponding excitation number along with the degeneracy indicated in the parentheses.

The vertical dashed line marks the iteration at which the fixed point is reached. Due to Eq. (3.34), the NRG spectrum is rescaled by a factor $\Lambda^{-N/2}$, where N denotes the iteration number. Consequently, the Fermi liquid energy scale is determined as $\omega_{\text{FL}} = \Lambda^{-N_{\text{fix}}/2}$.

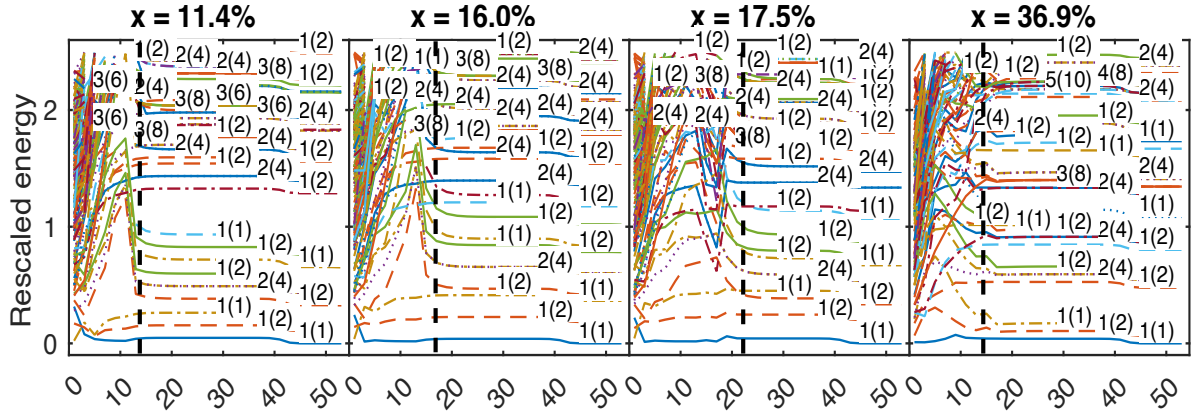


Figure 25: Energy flow obtained by solving the corresponding 2-impurity Anderson model. The black vertical dashed line indicates the fixed point N_{fix} .

The resulting Fermi liquid energy scales are listed in the Table 1. The same trend observed in Fig. 24 is evident here, where a phase boundary with a valley-like structure emerges. Additional values of ω_{FL} were calculated, confirming the absence of fluctuations in the overdoped regime.

Furthermore, one would expect a clear distinction between pseudogap states ($x < x_c$) and Fermi liquid states ($x > x_c$) if quantum criticality were present.

$x(\%)$	11.4	16.0	17.5	36.9
ω_{FL}	$10^{-3.3}$	$10^{-4.1}$	$10^{-5.0}$	$10^{-3.5}$

Table 1: Fermi liquid energy scales evaluated via the fixed point in energy flow. $\omega_{\text{FL}} = \Lambda^{-N_{\text{fix}}/2}$

However, across the entire doping range, including the underdoped regime, all energy flows consistently exhibit Fermi liquid characteristics, with no significant differences observed below or above x_c . This confirms our conclusion from the previous analysis: no quantum criticality is present.

To summarize, our calculations for the single-band Hubbard model do not reveal the anticipated quantum pseudogap-to-Fermi liquid phase transition at x_c . Instead, only a continuous insulator-to-metal transition is observed in the border momentum patch. This implies that 2-site clusters are too small to reveal the said quantum phase transition, further studies should focus on 4-site clusters. Moreover, it motivates further investigation using the three-band Hubbard model within the framework of the 2-site DCA. The inclusion of two additional p -orbitals is expected to enhance spatial correlations, even within the constraints of the 2-site scheme.

6 Numerical Results II (Emery Model)

6.1 Spectral functions

A detailed description of the Emery model is discussed in section 4.4. In our consideration, only interactions on d -orbitals are considered and denoted as U_d . This simplification is justified by DFT + U calculations, which argued that the Coulomb interaction on $p_{x/y}$ -orbitals and intersite interactions are much smaller than that on d -orbitals [38, 39]. As is well known in Mott physics, a large U_d can split the d -band into two subbands, i.e. the upper Hubbard band (UHB) and the lower Hubbard band (LHB). The resulting insulator is referred to as Mott insulator.

In this work we study another type of insulator that involves multiple orbitals. U_d opens a gap in the same way as in a Mott insulator, and pushes the UHB beyond the oxygen-dominant band, leading to an insulating gap. To excite electrons to the UHB, the required energy is estimated by the so-called charge transfer energy $\Delta \equiv \varepsilon_d - \varepsilon_p$, defined as the difference between on-site energies of d - and p -orbital, because charge transfer occurs between oxygen atoms and copper atoms. U_d is required to be much larger than Δ to form the charge-transfer gap (CTG), hence such an insulating system is referred to as a charge-transfer insulator (CTI), to be distinguished from a Mott insulator.

Upon doping the charge-transfer insulator, holes preferentially enter oxygen atoms first, as the p -orbital has higher on-site energy than LHO. Hybridization between p - and d -holes leads to the so-called Zhang-Rice singlet band, occupying the Fermi level [40].

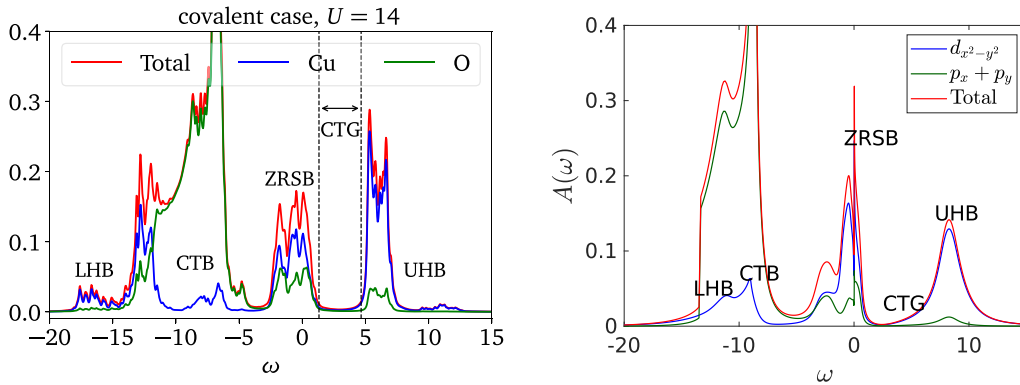


Figure 26: **Left panel:** Spectral function of both Cu- and O-atoms, labeled by their characteristic bands. The figure is taken from Ref. [35]. **Right panel:** Our results using the same parameters and doping level ($x_{\text{tot}} \sim 13\%$). The band positions show excellent agreement with the left panel, and the pseudogap is resolved more clearly.

For benchmark purposes, our results, computed for same parameters as Ref. [35], are presented in the left panel in Fig. 26. The band positions show reasonable

agreement, but our method provides significantly higher resolution in the low-energy regime near the Fermi level, allowing the pseudogap feature to be clearly observed. A clear LHB is absent for both of the results because the relatively small ε_p leads to stronger covalency and mixes LHU and CTB [35].

As shown in the right panel in Fig. 26, all the mentioned characteristic bands are well-recognized and labeled by their corresponding abbreviations. The spectral function is obtained at zero temperature ($\beta = 10^{10}$) with the following parameters [41]:

$$\varepsilon_d = 0, \varepsilon_p = -2.3, t_{pp} = 1, t_{pd} = 2.1, U_d = 14. \quad (6.1)$$

In this work, the electron picture is employed, therefore $\varepsilon_p < 0$, and the system is 13.3% hole-doped. In Emery model, as three orbitals d -, p_x - and p_y are included, doping levels in this work always refer to the total doping, counting contributions from the three bands. The half-filled reference is

$$n_d = 1, n_{p_x} = n_{p_y} = 2 \rightarrow n_{tot} = 1 + 2 \times 2 = 5, \quad (6.2)$$

as p -bands are expected to be fully filled in the charge transfer insulator, while the d -band, as the interacting band, is truly half-filled. Thus, the total doping is defined as

$$x_{tot} = 5 - (n_d + n_{p_x} + n_{p_y}) \quad (6.3)$$

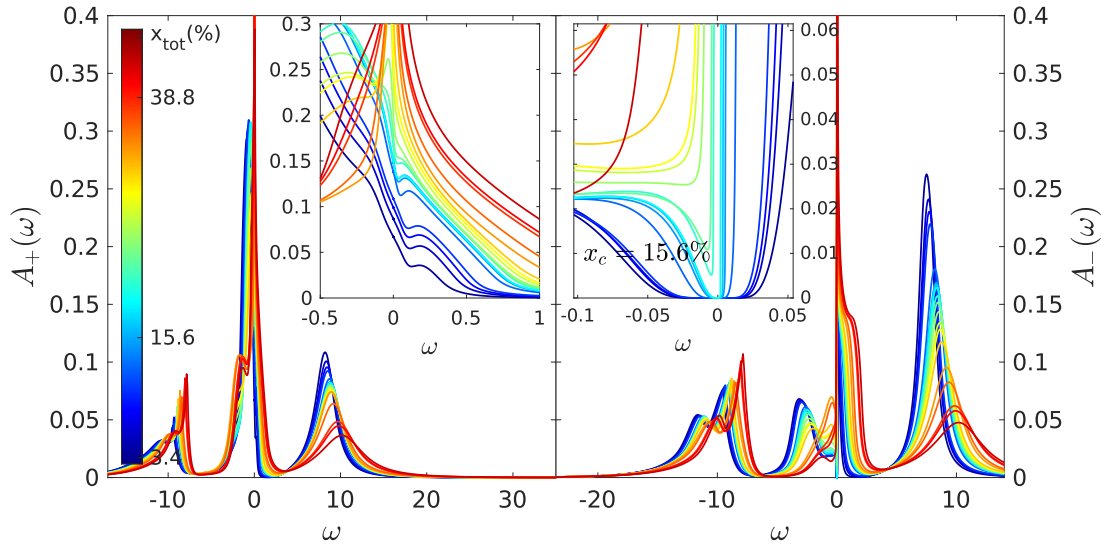


Figure 27: **Left panel:** d -orbital spectral function in the central patch. **Right panel:** d -orbital spectral functions in the border patch, as a function of total doping x_{tot} . The pseudogap in $A_-(\omega)$ gradually closes with increasing doping, the critical doping is defined at $x_c = 15.6\%$, above which spectral function weight becomes non-vanishing at the Fermi level.

Additional results at different doping levels are presented in Fig. 27. In the Emery model, where only the d -orbital is interacting, our focus is primarily on the

d -band, particularly in the border patch. The pseudogap observed in the spectral function $A_-(\omega)$ exhibits behavior strikingly similar to that in the Hubbard model: the gap width gradually narrows, and the spectral weight, initially suppressed, becomes finite above the critical doping level $x_c = 15.6\%$, which we define in the same way as for the Hubbard model.

Fermi surface and electronic structure

As a three-band model, we inspect the spectral function at the Fermi level

$$\begin{aligned} A(\mathbf{k}, \omega = 0) &= -\frac{1}{2\pi i} \text{Tr} \{ \mathbf{G}(\mathbf{k}, \omega = 0) - \mathbf{G}^\dagger(\mathbf{k}, \omega = 0) \} \\ &= -\frac{1}{\pi} \sum_i \text{Im} \{ (0 + \mu)\mathbf{1} - \mathbf{h}(\mathbf{k}) - \Sigma(\mathbf{k}, \omega = 0) \}_{ii}^{-1}. \end{aligned} \quad (6.4)$$

Here, $\mathbf{h}(\mathbf{k})$ is the non-interacting Hamiltonian and $\Sigma(\mathbf{k}, \omega)$ self-energy, defined in Chapter 4. As shown in the upper row of Fig. 28, where no interpolation is applied, the results exhibit the same trend as observed in the Hubbard model—the gapped border patch gradually recovers coherence as doping increases above x_c .

In the lower row, the cumulant interpolation is applied, utilizing the identical weight function Eq. (2.69) as in the Hubbard model. For sufficiently low doping $x_{\text{tot}} = 3.4\%$, the spectral weight is strongly suppressed and the arc structure observed in Hubbard model is almost unrecognizable. For doping levels just at and above x_c , i.e. $x_{\text{tot}} = 15.6\%$ and $x_{\text{tot}} = 16.0\%$, there is always a closed Fermi surface centered at $(0, 0)$, the d - p orbital hybridization shifts the closed Fermi surface to be less hole-like, with smaller curvature around $(\pi/2, \pi/2)$ compared to that in Fig. 18. In the case of $x_{\text{tot}} = 38.8\%$, an electron-like Fermi surface appears. Again, we observe a continuous transition across x_c and no quantum criticality in the Fermi surface, even with the inclusion of additional p -orbitals.

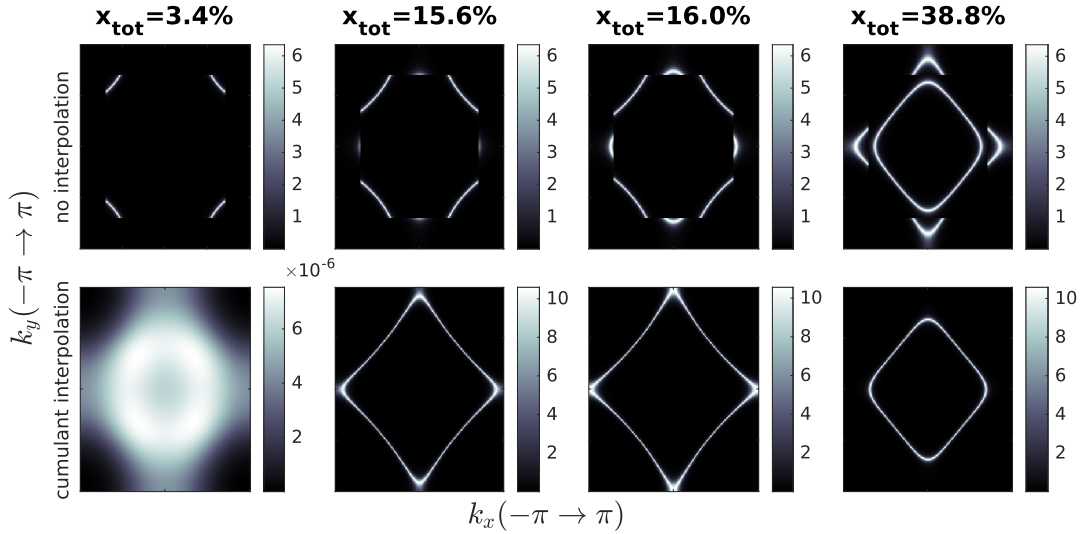


Figure 28: **Upper row:** Spectral function at Fermi level $A(k, \omega = 0)$ without interpolation for several doping values. Two above and two below x_c . **Lower row:** Same as the upper row with cumulant interpolation.

6.2 Self-energy and quasiparticle weight

The imaginary part of the d -orbital self-energy is shown in Fig. 29. One of the curves in the overdoped regime ($x_{\text{tot}} = 45.0\%$) is fitted with a quadratic function, and we investigate the asymptotic behavior within $\Delta\omega \equiv [10^{-3}, 10^{-1}]$

In the underdoped regime ($x < x_c$), the curves exhibit a steeper slope than the quadratic reference and cannot be adequately fitted by a quadratic function without significant deviation, indicating the absence of Fermi liquid behavior within the range $\Delta\omega$. As doping increases and exceeds x_c , the slope gradually decreases, and the curves continuously transition into the overdoped ones ($x > x_c$). Ultimately, the curves converge towards the quadratic reference ω^2 , indicating the emergence of Fermi liquid behavior within $\Delta\omega$.

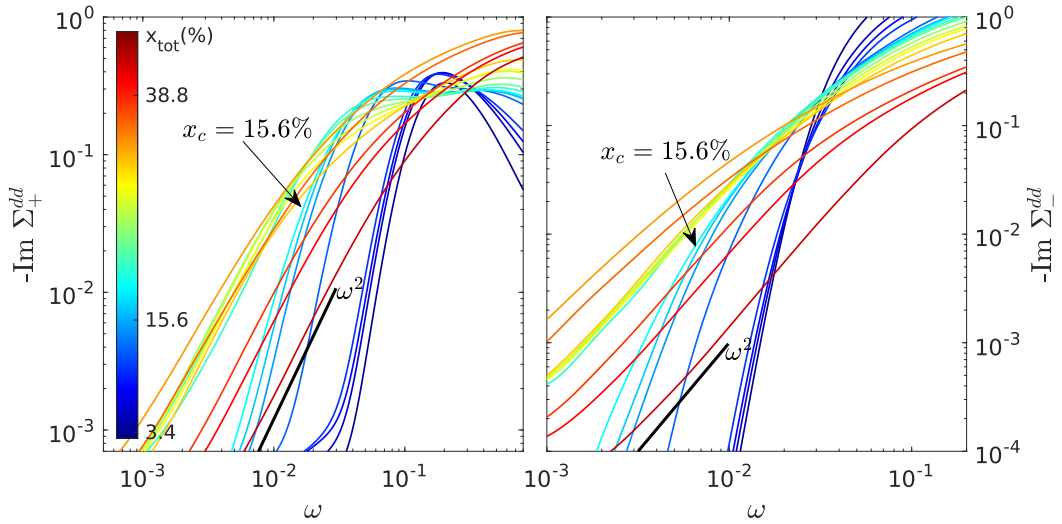


Figure 29: **Left panel:** The imaginary part of the self-energy for the central patch is shown. The curve at a doping level of $x = 45.0\%$ is fitted with a quadratic function, represented by the dark solid line. The curves first evolve toward x_c and then approach the quadratic reference with the increasing doping level. **Right panel:** The imaginary part of the self-energy for the border patch is presented.

The quasiparticle weight for each momentum patch is evaluated using the real part of the d -orbital self-energy. The results are shown in Fig. 29. The drastic decrease in Z_+ is highlighted by the derivative $\Delta Z/\Delta x_{\text{tot}}$, which exhibits a pronounced valley at x_c , even more distinct than that in Hubbard model. Furthermore, the nearly linear trend in Z_- observed in Hubbard model is suppressed here. As a result, the greater compensation in Z_+ combined with suppression in Z_- in underdoped regime yields the overall non-monotonic behavior in Z_{tot} .

As observed in both Fig. 29 and Fig. 30, the transition around x_c in the Emery model is more pronounced than in the Hubbard model. This suggests that incorporating multiple orbitals can, to some extent, enhance spatial correlations, thereby amplifying the sharpness of the transition, although it is still continuous.

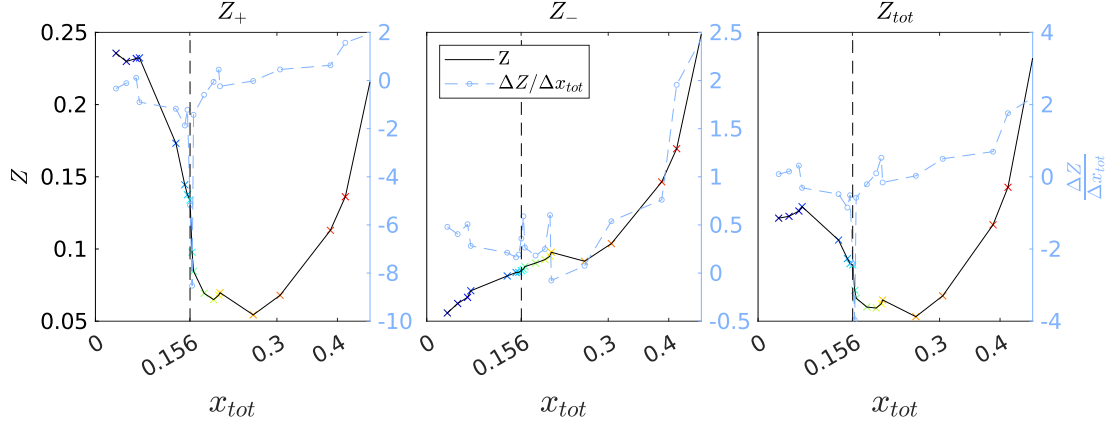


Figure 30: **Left panel:** The quasiparticle weight for the central patch. **Middle panel:** The quasiparticle weight for the border patch. **Right panel:** The averaged quasiparticle weight. The black solid line with colored markers represents Z , while the gray dashed lines indicate its derivative with respect to doping x . The vertical dashed line marks x_c .

6.3 Susceptibility and phase diagram

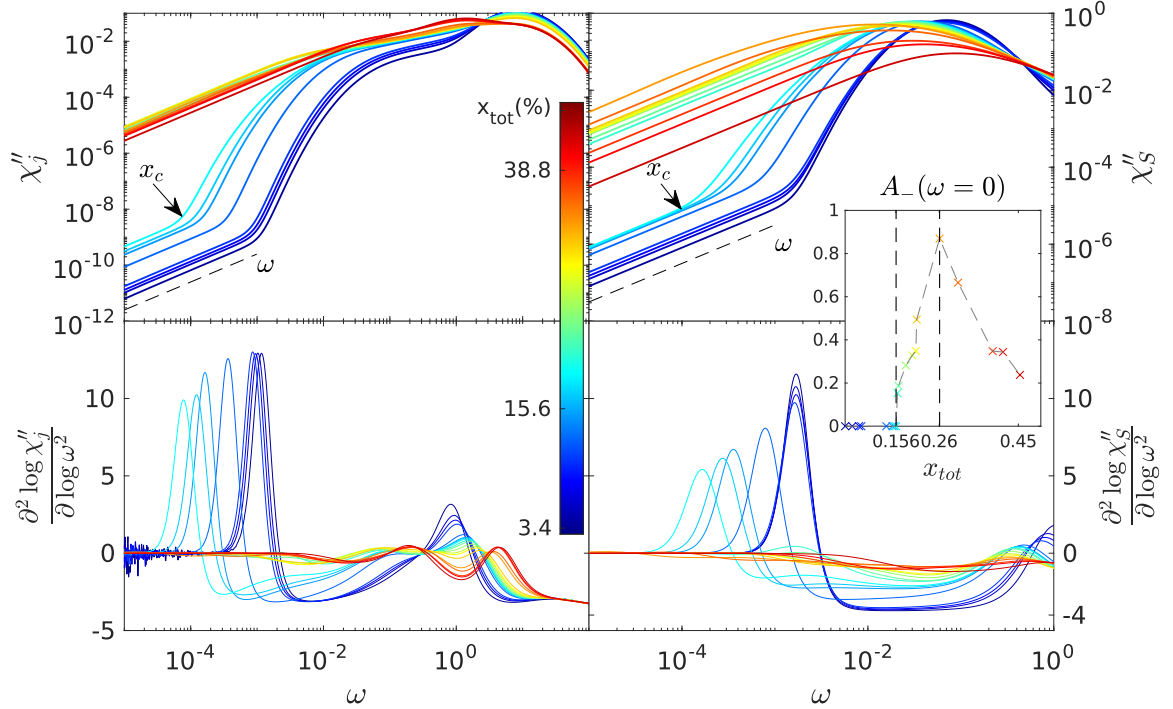


Figure 31: **Upper panels:** Current susceptibility χ_j'' and spin (magnetic) susceptibility χ_S'' . When the border patch is gapped ($x < x_c$), the curves exhibit an upward kink. As the doping level increases beyond x_c , the curves evolve into downward kinks. **Lower panels:** Second-order derivative of χ_j''/S , where the extremum coordinates are used to determine ω_{FL} .

Fig. 31 shows, the current and spin susceptibilities, along with their respective second-order derivatives. The upward kinks observed at $x < x_c$ in the susceptibilities transition into downward kinks as doping increases above the critical doping level x_c . In the near-static limit, $\chi''_{j/S}(\omega \rightarrow 0)$, a more pronounced leap at x_c is observed compared to the Hubbard model due to the inclusion of p -orbitals.

The Fermi liquid energy scale is extracted the same way as for the Hubbard model as shown in Appendix A. ω_{FL} as a function of x_{tot} is shown in Fig. 32, where the vertical dashed line marks the critical doping level x_c , which coincide with the valley formed by the extracted energy scales. Also the energy scales don't go down to zero and reach roughly the same values as the Hubbard model. The dip observed in the overdoped regime ($x_{tot} \sim 40\%$) in χ''_S arises from the same reason discussed in Appendix A, i.e. the determination of ω_{FL} using second-order derivative breaks down due to numerical inaccuracy caused by the crossover region.

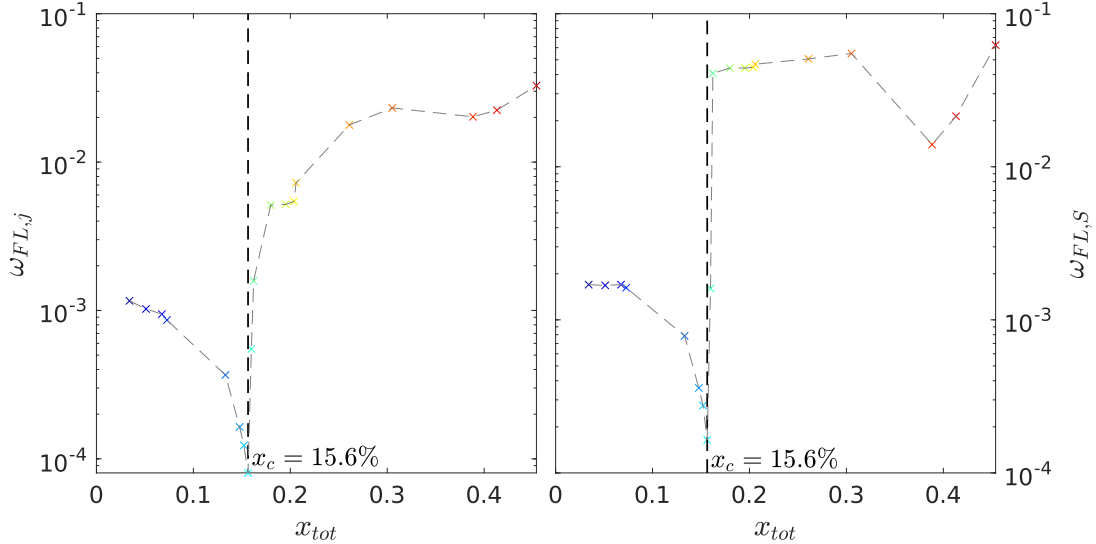


Figure 32: **Left panel:** The phase diagram determined by χ''_j . **Right panel:** The phase diagram determined by χ''_S . The critical doping in both cases is $x_c = 15.6\%$, consistent with that determined from $A_-(\omega)$.

6.4 Energy flow

Fig. 33 presents the energy flows from NRG calculations. Only even iterations of the border patch is shown. Each flow is labeled by the corresponding excitation number along with the degeneracy indicated in the parentheses.

Fermi liquid energy scales evaluated via $\omega_{FL} = \Lambda^{-N_{fix}/2}$ are listed in Table 2 follows the same pattern as shown in the phase diagram. Beside, the flow diagrams consistently exhibit Fermi liquid characteristics, confirming that there is no quantum phase transition around x_c .

$x_{\text{tot}}(\%)$	3.4	15.6	16.0	38.8
ω_{FL}	$10^{-2.8}$	$10^{-4.7}$	$10^{-4.7}$	$10^{-2.8}$

Table 2: Fermi liquid energy scales evaluated via the fixed point in energy flow.
 $\omega_{\text{FL}} = \Lambda^{-N_{\text{fix}}/2}$

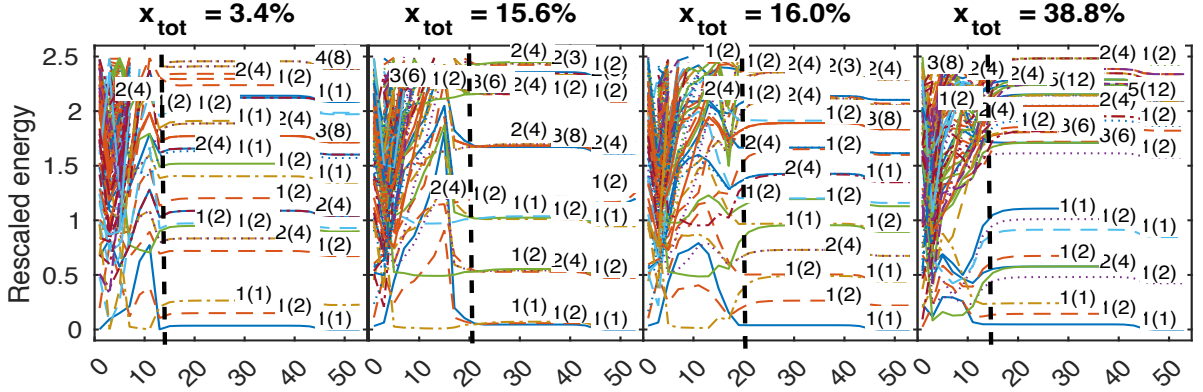


Figure 33: Energy flow of the border DCA patch for Emery model. The black vertical dashed line indicates the fix point N_{fix} , which is connected to the Fermi liquid energy scale via $\Lambda^{-N_{\text{fix}}/2}$.

Combining the various quantities examined—spectral function, self-energy, susceptibility, and energy flow—we conclude that even with the inclusion of additional p -orbitals in the three-band model, 2-site DCA framework is unable to capture the potential QCP.

7 Conclusion and Outlook

Conclusion

In this thesis, we utilized the combination of Numerical Renormalization Group (NRG) and Dynamical Cluster Approximation (DCA) to explore the potential pseudogap-to-Fermi liquid phase transition. This investigation was conducted using both the single-band Hubbard model and a more realistic three-band model—the Emery model—which incorporates additional $p_{x/y}$ -orbitals to describe the CuO_2 plane while neglecting Coulomb interaction on the oxygen atoms.

NRG, on one hand, enables the resolution of low-energy behavior near the Fermi level with, in principle, zero temperature and infinite frequency resolution. On the other hand, DCA, as a cluster extension of DMFT, provides access to momentum-dependent properties such as the nodal-antinodal dichotomy in hole-doped cuprates, which is fundamental to the emergence of the pseudogap. The synergy of NRG and DCA thus makes the investigation of pseudogap phenomena feasible and insightful.

By making use of these robust tools, we successfully reproduced the partially gapped spectral function $A_-(\omega)$ using a minimal cluster impurity model for both the single-band and three-band models. Furthermore, we reconstructed the characteristic Fermi arc for the single-band model using an effective interpolation scheme.

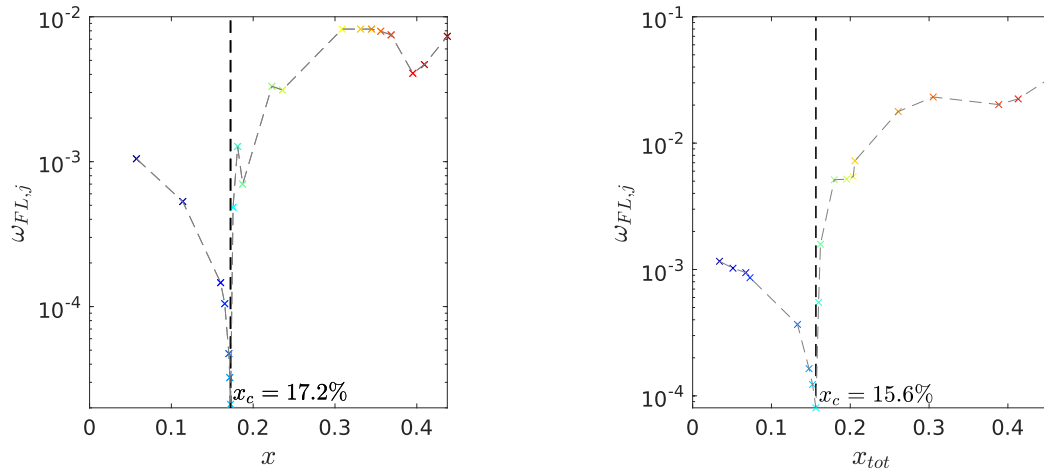


Figure 34: **Left panel:** The phase diagram of the Hubbard model using ω_{FL} extracted from χ''_j . **Right panel:** The corresponding phase diagram of the Emery model.

To examine the potential quantum criticality, we fixed the temperature at zero and systematically varied the hole doping across a wide range. A critical doping level, x_c , beyond which the pseudogap closes, was identified in both models. To explore the dynamical properties further, we computed two types of Green's

functions: current and spin susceptibilities. Using $\chi''_{j/S}$, we defined the so-called Fermi liquid energy scale, ω_{FL} , as the frequency below which Fermi liquid behavior emerges. The doping dependence of ω_{FL} allowed us to construct a phase diagram that corroborates the critical doping x_x identified from the spectral functions. Fig. 34 shows a similar structure in the phase diagrams of the Hubbard model and the Emery model, respectively.

However, a detailed examination of the spectral function, including the Fermi surface, and susceptibility confirms that the defined critical doping x_c is not a genuine quantum critical point (QCP); rather, it represents the insulator-to-metal transition in the border (antinodal) momentum patch.

This is corroborated by the energy flow from the NRG calculations, offering an alternative perspective on the energy scale ω_{FL} and phase characteristics. The energy flow across all doping levels, including the underdoped regime, consistently exhibits Fermi liquid characteristics. This observation further confirms that the anticipated quantum critical point is fundamentally absent in our 2-site results.

Nevertheless, our work systematically compared the single-band and three-band models in response to hole doping and found that they exhibit strikingly similar behavior. This suggests that the inclusion of p -bands, while enhancing spatial correlations, does not lead to a significant difference, at least within the 2-site DCA framework. This finding highlights the necessity of employing a 4-site cluster for deeper insights in this field.

Outlook

Our 2-site DCA framework can be readily extended to a 4-site cluster, enabling a more detailed investigation of the pseudogap phenomenon and potential quantum criticality. As demonstrated in the ongoing 4-site calculations [42], a larger cluster enhances momentum resolution, captures the other critical point x_c absent in the 2-site scheme, and exhibits an emerging plateau behavior in susceptibilities, thereby aiding in addressing challenges associated with determining the Fermi liquid energy scale ω_{FL} .

The three-band model, with its realistic inclusion of p -orbitals, provides an ideal basis for further study. Leveraging the excellent low-energy resolution of NRG, future work could explore the effects of d - p hybridization more comprehensively via tuning other model parameters t_{dp} and t_{pp} . This may reveal subtle differences not captured by the 2-site framework and offer new insights into the CuO_2 plane's spectral and dynamical properties.

Moreover, the 4-site cluster extension enables the evaluation of the superconducting order parameter, significantly broadening our scope in exploring the cuprate phase diagram.

A Fluctuations in the overdoped regime

In the overdoped regime $x > x_c$, ω_{FL} is expected to increase monotonically as Fermi liquid theory predicts. Nevertheless, the profile of $\omega_{FL}(x)$ above x_c exhibits some unexpected dips, as seen in Fig. 24. In this appendix, we detail the procedure used to extract ω_{FL} , emphasizing the determination process and addressing the unexpected fluctuations observed in the overdoped regime. While the discussion is focused on the Hubbard model, the same arguments apply to the Emery model.

The first dip (around $x \sim 18\%$) is caused by the merging of the maximum in $\frac{\partial^2 \log \chi_j''}{\partial (\log \omega)^2}$, as shown in Fig.35. When the doping level increases across x_c , the maximum in the second-order derivative progressively merges with the minimum. Consequently, the measure of ω_{FL} using second derivative breaks down, as multiple local minima coexist. Nevertheless, this dip in χ_j'' is unphysical and reflects the continuous nature of the transition.

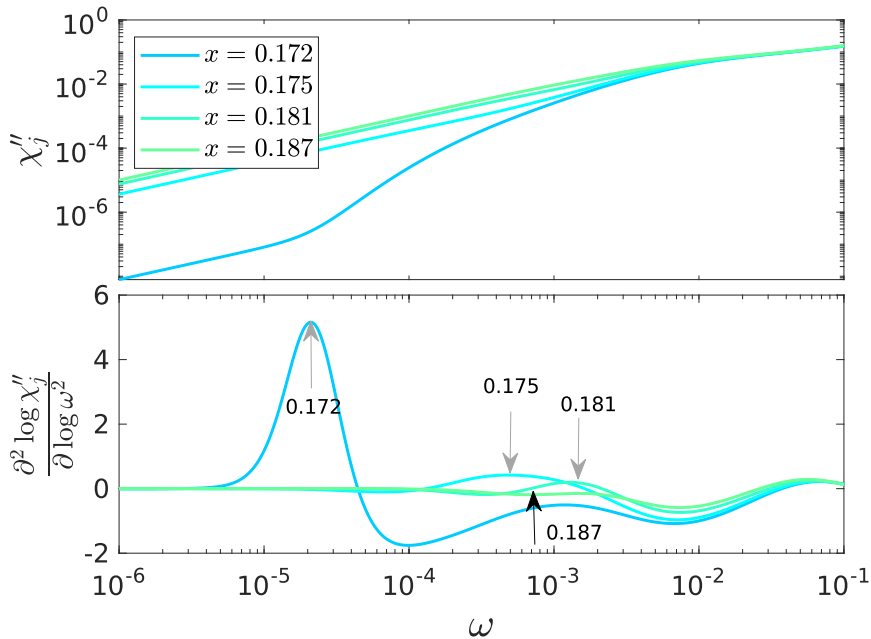


Figure 35: The current susceptibilities at doping levels $x = 17.2\% \sim 18.7\%$, along with their second-order derivatives, are presented to illustrate the merging of the curvature maximum, which results in an unexpected dip in the phase diagram.

The second dip (around $x \sim 40\%$) is attributed to similar reason. As the doping level surpasses $x \sim 33\%$, a broad crossover emerges in χ_j'' , reducing the accuracy of the determination of ω_{FL} via curvature, as illustrated in Fig.36.

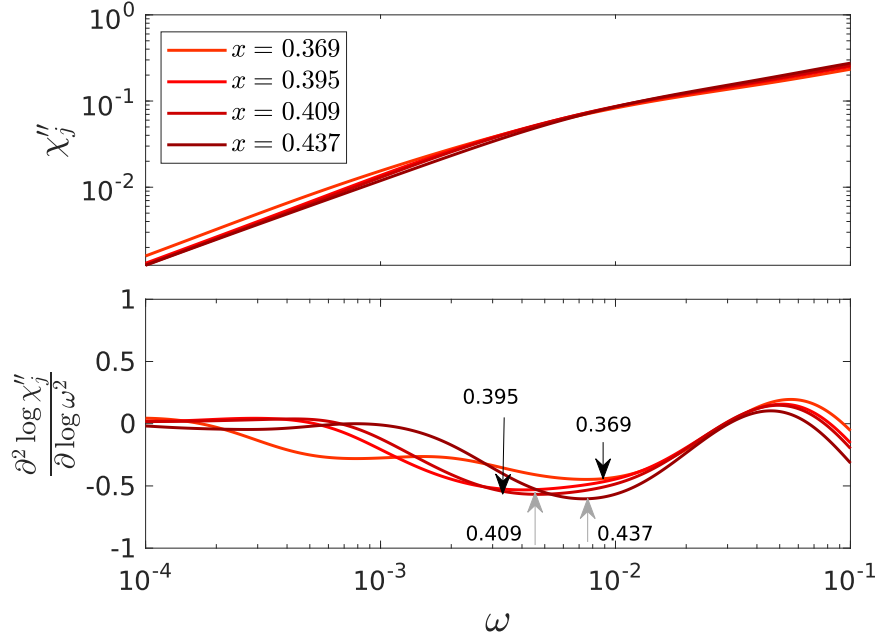


Figure 36: The current susceptibilities at doping levels $x = 36.9\% \sim 43.7\%$, along with their second-order derivatives, are presented to emphasize the broad crossover of the curvature minimum, which contributes to the unexpected dip observed in the overdoped regime of the phase diagram.

B Electronic structure

In this appendix, the electronic structures of both the Hubbard and Emery models are presented, providing verification of Zhang and Rice's proposal from this perspective, as discussed in [40].

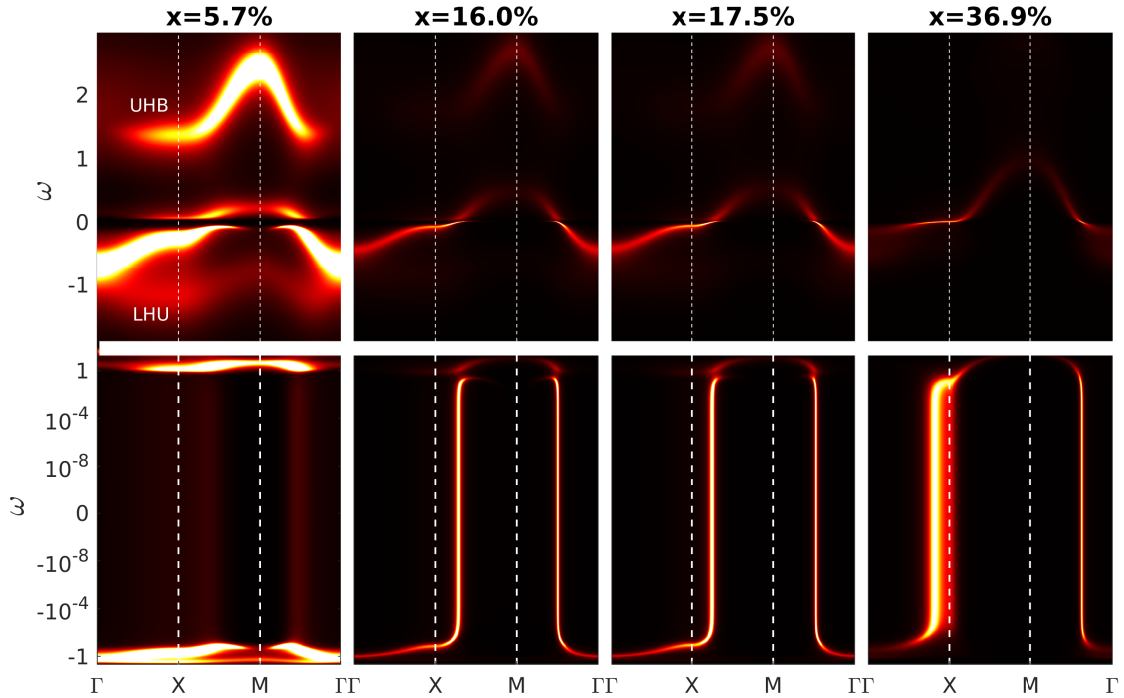


Figure 37: **Upper row:** The electronic structure is shown on a liner-scaled frequency axis. **Lower row:** A logarithmic-scaled frequency axis is applied. The (π, π) -centered Fermi arc (and surface) is characterized by the absence of spectral weight at $\omega = 0$ within $(\Gamma \rightarrow X)$, while the $(0, 0)$ -centered Fermi surface is distinguished by a pronounced spectral weight at $\omega = 0$ within $(\Gamma \rightarrow X)$.

In Fig. 37, the upper panels illustrate the overall electronic structure of the Hubbard model. Meanwhile, the lower panels, which employ a logarithmic scale for the frequency axis, depict the transition from the Fermi arc to the Fermi surface shifting from being centered at (π, π) to $(0, 0)$ as doping increases.

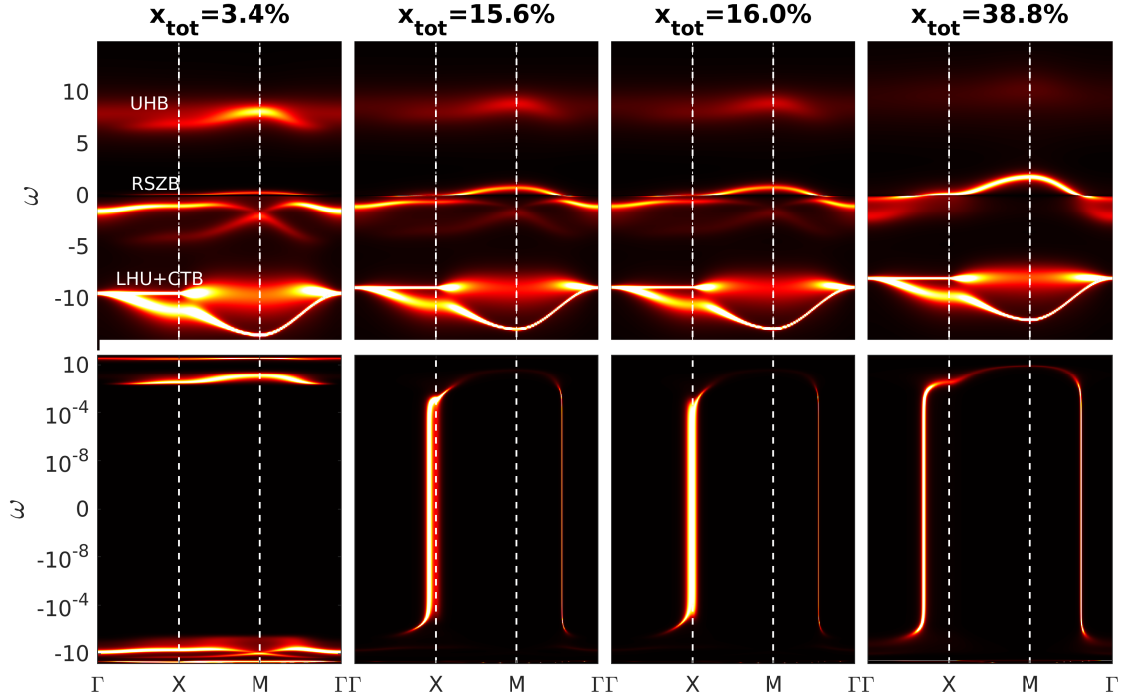


Figure 38: **Upper row:** The electronic structure is shown on a liner-scaled frequency axis. p -bands (CTB) are trivially shifted toward Fermi level as chemical potential decreases, contributing to the total doping level x_{tot} . **Lower row:** A logarithmic-scaled frequency axis is applied.

The electronic structure of Emery model is presented in Fig.38. The resemblance between the ZRSB + UHB in the Emery model and the LHB + UHB in the Hubbard model supports Zhang and Rice's proposal that the three-band model can be effectively reduced to a single-band model [40].

Moreover, as shown in the upper row of Fig.38, the p -bands (CTB) are trivially shifted toward the Fermi level due to the increasing total doping level x_{tot} , as defined in Eq. (6.3).

References

- [1] Andrea Damascelli, Zahid Hussain, and Zhi-Xun Shen. Angle-resolved photoemission studies of the cuprate superconductors. *Rev. Mod. Phys.*, 75:473–541, Apr 2003.
- [2] Kyle M. Shen, F. Ronning, D. H. Lu, F. Baumberger, N. J. C. Ingle, W. S. Lee, W. Meevasana, Y. Kohsaka, M. Azuma, M. Takano, H. Takagi, and Z.-X. Shen. Nodal quasiparticles and antinodal charge ordering in $\text{Ca}_{2-x}\text{Na}_x\text{CuO}_2\text{Cl}_2$. *Science*, 307(5711):901–904, 2005.
- [3] Antoine Georges and Gabriel Kotliar. Hubbard model in infinite dimensions. *Phys. Rev. B*, 45:6479–6483, Mar 1992.
- [4] Gabriel Kotliar, Sergej Y. Savrasov, Gunnar Pálsson, and Giulio Biroli. Cellular dynamical mean field approach to strongly correlated systems. *Phys. Rev. Lett.*, 87:186401, Oct 2001.
- [5] Michel Ferrero, Pablo S. Cornaglia, Lorenzo De Leo, Olivier Parcollet, Gabriel Kotliar, and Antoine Georges. Pseudogap opening and formation of fermi arcs as an orbital-selective mott transition in momentum space. *Phys. Rev. B*, 80:064501, Aug 2009.
- [6] M. H. Hettler, M. Mukherjee, M. Jarrell, and H. R. Krishnamurthy. Dynamical cluster approximation: Nonlocal dynamics of correlated electron systems. *Phys. Rev. B*, 61:12739–12756, May 2000.
- [7] Kenneth G. Wilson. The renormalization group: Critical phenomena and the kondo problem. *Rev. Mod. Phys.*, 47:773–840, Oct 1975.
- [8] R Bulla, A C Hewson, and Th Pruschke. Numerical renormalization group calculations for the self-energy of the impurity anderson model. *Journal of Physics: Condensed Matter*, 10(37):8365, sep 1998.
- [9] V. J. Emery. Theory of high- t_c superconductivity in oxides. *Phys. Rev. Lett.*, 58:2794–2797, Jun 1987.
- [10] DFG Research Unit 1346, editor. *The LDA+DMFT approach to strongly correlated materials*, volume 1 of *Schriften des Forschungszentrums Jülich, Reihe Modeling and Simulation*. Forschungszentrum Jülich, Forschungszentrum Jülich, October 2011. Held on 4 – 7 October 2011.
- [11] E. Müller-Hartmann. Correlated fermions on a lattice in high dimensions. *Zeitschrift für Physik B Condensed Matter*, 74(4):507–512, 1989.
- [12] P. W. Anderson. Localized magnetic states in metals. *Phys. Rev.*, 124:41–53, Oct 1961.

-
- [13] Emanuel Gull, Andrew J. Millis, Alexander I. Lichtenstein, Alexey N. Rubtsov, Matthias Troyer, and Philipp Werner. Continuous-time monte carlo methods for quantum impurity models. *Rev. Mod. Phys.*, 83:349–404, May 2011.
- [14] Andreas Weichselbaum. Tensor networks and the numerical renormalization group. *Phys. Rev. B*, 86:245124, Dec 2012.
- [15] Andreas Weichselbaum. Qspace - an open-source tensor library for abelian and non-abelian symmetries, 2024.
- [16] Andreas Weichselbaum. X-symbols for non-abelian symmetries in tensor networks. *Phys. Rev. Res.*, 2:023385, Jun 2020.
- [17] Thomas Maier, Mark Jarrell, Thomas Pruschke, and Matthias H. Hettler. Quantum cluster theories. *Rev. Mod. Phys.*, 77:1027–1080, Oct 2005.
- [18] Giulio Biroli and Gabriel Kotliar. Cluster methods for strongly correlated electron systems. *Phys. Rev. B*, 65:155112, Apr 2002.
- [19] Tudor D. Stanescu and Gabriel Kotliar. Fermi arcs and hidden zeros of the green function in the pseudogap state. *Phys. Rev. B*, 74:125110, Sep 2006.
- [20] Alex Hewson and Jun Kondo. Kondo effect. *Scholarpedia*, 4(3):7529, January 2009.
- [21] Wolfgang Mnder. *Matrix product state calculations for one-dimensional quantum chains and quantum impurity models*. PhD thesis, Ludwig–Maximilians–Universitt Mnchen, Mnchen, August 2011. Dissertation submitted on 30.08.2011.
- [22] E. Pavarini, E. Koch, F. Anders, and M. Jarrell. Correlated electrons: From models to materials. Lecture Notes, Modeling and Simulation Vol. 2, 2012.
- [23] Ralf Bulla, Theo A. Costi, and Thomas Pruschke. Numerical renormalization group method for quantum impurity systems. *Rev. Mod. Phys.*, 80:395–450, Apr 2008.
- [24] Ralf Bulla, Hyun-Jung Lee, Ning-Hua Tong, and Matthias Vojta. Numerical renormalization group for quantum impurities in a bosonic bath. *Phys. Rev. B*, 71:045122, Jan 2005.
- [25] Andreas Weichselbaum and Jan von Delft. Sum-rule conserving spectral functions from the numerical renormalization group. *Phys. Rev. Lett.*, 99:076402, Aug 2007.
- [26] Seung-Sup B. Lee and Andreas Weichselbaum. Adaptive broadening to improve spectral resolution in the numerical renormalization group. *Phys. Rev. B*, 94:235127, Dec 2016.

-
- [27] Ralf Bulla. The numerical renormalization group. 624th Wilhelm und Else Heraeus-Seminar: Simulating Quantum Processes and Devices, September 2016. Presentation slides.
- [28] Wolfgang Nolting. *Theoretical Physics 9: Fundamentals of Many-body Physics*. Springer, Cham, 2018. Published: 15 November 2018.
- [29] W. F. Brinkman and T. M. Rice. Application of gutzwiller’s variational method to the metal-insulator transition. *Phys. Rev. B*, 2:4302–4304, Nov 1970.
- [30] B. Keimer, S. A. Kivelson, M. R. Norman, S. Uchida, and J. Zaanen. From quantum matter to high-temperature superconductivity in copper oxides. *Nature*, 518(7538):179–186, 2015.
- [31] Makoto Hashimoto, Inna M. Vishik, Rui-Hua He, Thomas P. Devereaux, and Zhi-Xun Shen. Energy gaps in high-transition-temperature cuprate superconductors. *Nature Physics*, 10(7):483–495, 2014.
- [32] Zölf, M. B., Maier, Th., Pruschke, Th., and Keller, J. Electronic properties of cuo2-planes: A dmft study. *Eur. Phys. J. B*, 13(1):47–53, 2000.
- [33] Peizhi Mai, Giovanni Balduzzi, Steven Johnston, and Thomas A. Maier. Pairing correlations in the cuprates: A numerical study of the three-band hubbard model. *Phys. Rev. B*, 103:144514, Apr 2021.
- [34] L. Fratino, P. Sémon, G. Sordi, and A.-M. S. Tremblay. Pseudogap and superconductivity in two-dimensional doped charge-transfer insulators. *Phys. Rev. B*, 93:245147, Jun 2016.
- [35] Nicolas Kowalski, Sidhartha Shankar Dash, Patrick Sémon, David Sénéchal, and André-Marie Tremblay. Oxygen hole content, charge-transfer gap, covalency, and cuprate superconductivity. *Proceedings of the National Academy of Sciences*, 118(40):e2106476118, 2021.
- [36] Yi-Ting Tseng, Mário O. Malcolms, Henri Menke, Marcel Klett, Thomas Schäfer, and Philipp Hansmann. Single- and two-particle observables in the emery model: a dynamical mean-field perspective, 2024.
- [37] Andreas Gleis. Cluster dynamical mean-field + numerical renormalization group approach to strongly correlated systems. Master’s thesis, Ludwig-Maximilian University, Munich, 2019.
- [38] A. K. McMahan, Richard M. Martin, and S. Satpathy. Calculated effective hamiltonian for la₂cuo₄ and solution in the impurity anderson approximation. *Phys. Rev. B*, 38:6650–6666, Oct 1988.
- [39] Mark S. Hybertsen, Michael Schlüter, and Niels E. Christensen. Calculation of coulomb-interaction parameters for la₂cuo₄ using a constrained-density-functional approach. *Phys. Rev. B*, 39:9028–9041, May 1989.

- [40] F. C. Zhang and T. M. Rice. Effective hamiltonian for the superconducting cu oxides. *Phys. Rev. B*, 37:3759–3761, Mar 1988.
- [41] C. Weber, C. Yee, K. Haule, and G. Kotliar. Scaling of the transition temperature of hole-doped cuprate superconductors with the charge-transfer energy. *Europhysics Letters*, 100(3):37001, nov 2012.
- [42] M. Pelz, A. Gleis, and Jan von Delft. The pseudogap-Fermi liquid transition in the Hubbard model using DCA+NRG. This is an ongoing project carried out by the Chair of Theoretical Solid State Physics at Ludwig Maximilian University, 2024.